Measurements of the Strong Coupling Constant and the QCD Colour Factors using Four-Jet Observables from Hadronic Z Decays in ALEPH[1]

Sílvia Bravo i Gallart
Universitat Autònoma de Barcelona
Departament de Física
Edifici Cn E-08193 Bellaterra (Barcelona)

September 2001

[1]Ph.D. Dissertation

Al meu padrí, perquè era com era.
Al Gon, perquè és com és.

The work presented in the following pages has provoked to me many and different feelings. But now, that all has finished, I will concentrate in the good ones.

Three years ago, in an ALEPH week, I met Dr. Günther Dissertori. He told to us, Hugo and myself, about a nice QCD analysis. Since Hugo was an anti-QCD guy (there is a "school" here at IFAE) there was no need to fight for it. Since then I have worked with and LEARNT FROM Günther, who became the supervisor of this thesis. Now I know I was very lucky to have the possibility to work with a QCD- "lover" and expert.

Of course, the possibility of writting such an "interesting" work is also due to IFAE, and more precisely to Dr. Enrique Fernández, who gave me the chance to enter the IFAE-community and the high energy physics environment.

From the IFAE-community I will first talk about Dra. Mª Lluïsa Mir. She has been almost always close to me (since some months she is living in the States), and I could explode and tell her what was making my days hard at any moment. Also Dra. Martine Bosman was close. I worked with her for my master thesis, which was a pleasure, but she kept showing interest for my work (and smiling!).

Before the death of the ALEPH experiment (*RIP*) there was an intense activity here at IFAE around the ALEPH data. A lot of meetings were held, and we were following and trying to help one to each other. To all the ALEPH meeting group (Lluïsa, Manel, Frederic, Aurelio, Imma, Pilar, Gon, Eugeni, Hugo and Javier) thanks a lot. I should mention also the ALEPH-CERN meeting group... they asked a lot, but helped also. Thanks to Günther, Roger, Hasko, John, etc. And to finish, some words to the BCAL team: Mokhtar, Pilar, Gon, Eugeni, Gaelle, Hugo, Javier and David. It was a pleasure to share with you the use of the portable phone!

Finally, I will not stop my "professional thanks giving" without talking about all the people I worked with when I discovered the particle physics world. I am talking about Martine, Matteo, Manuel and Irene.

Deixo l'anglès i vaig a la meva llengua materna: lo pontsicà. Cares i somriures ben variats m'han fet costat durant els dies - llargs, llarguíssims - que ha durat tot plegat. Ara mentre rumiava com escriure aquests agraïments pensava que sóc una persona afortunada, perquè tinc molts a qui agrair.

Tinc una família molt "maja", cadascú amb el seu tarannà, però tots ben "majos". Una "família adoptiva" que són una Perla (Negra). Una família que s'extén a partir del Gon i que he descobert molt gran, en extensió i en estima.

Les meves arrels pontsicanes es mantenen i s'engreixen amb els anys (a veure si aconsegueixo mantenir l'engreix a les arrels!). Els de ponent som guais, això no ho dubta ningú... ja ho diu la cançó "Ser de Lleida és lo millor que hi ha". Entre tota la tribu de ponent, a Ponts i comarca jo he conegut a gent molt gran. Em podria posar a dir noms i ompliria línies i més línies. Ho deixo aquí, dient-los gràcies a tots per estar aquí, o allí, o on esteu ara mateix.

En aquests dies de globalitzacions, immigracions i misèries una pobra pontsicana s'ha vist obligada a veure món... he conegut comarques noves, i finalment he deixat els meus "trastos" (de moment) a Castellar del Vallès. He vist que la gent de comarques, com ara els del barcelonès, són bona gent. Hi ha de tot, com a tot arreu, però jo m'he topat amb "de lo mejorcito, lo mejor". Els músics i les amants, físics en matrimoni i canalla, cerdanyolencs que es casen, que renten, que toquen, que juguen... un ventall de cares i maneres de fer digne d'estudi.

Aquí a l'IFAE he fet bons amics. Alguns encara hi són, altres han deixat les nostres parets verdes i han començat nova vida més lluny o més a prop. Tots són molt treballadors, i ves per on, en general molt barruts. N'hi ha de rinxolats, n'hi ha d'irisats, n'hi ha que fan punt de creu, n'hi ha que no es pentinen,...

Acabo amb música. La del Último de la fila, la dels Burros, la del Manolo García... la que m'ha acompanyat durant hores i hores, i que encapçala algunes seccions d'aquest treball.

I res, que fins aquí he arribat i a des d'aquí hauré de continuar. Espero tenir-vos al costat, a tots, durant molt i molt de temps.

GRÀCIES

Contents

List of Figures

List of Tables

Chapter 1

Introduction

It is generally believed that Quantum Chromodynamics (QCD) is the correct theory for the description of the strong interaction of quarks and gluons. This theory has been successfully tested at high energies, but proofs that QCD predicts some basic properties observed in nature, such as confinement of quarks in hadrons, are still missing. The lack of these proofs is due both to the mathematical complexity of the theory and to the non-applicability of the perturbative theory at low energies. Thanks to the enormous statistics accumulated at the LEP e^+e^- storage ring and the considerable theoretical progress in the field of perturbative QCD, the measurements and tests of QCD have entered the high precision regime. The strong coupling constant is not too "strong" at these high energies, which increases the reliability of perturbative calculations, and at the same time non-perturbative corrections to many observables, related to the hadronization of quarks and gluons into observable hadrons, become small.

During the last years, a large number of measurements have been performed and the theoretical predictions have been proved to predict better and better the experimental distributions. This improvement is due to new calculations that allow for an exact fixed order prediction at higher orders, but also to new Monte Carlo (MC) Programs. The latest versions of the already existing MCs as well as the new codes include the exact matrix elements for up to five-parton final state configurations. The present knowledge on the contributions of missing higher order terms and on soft phenomena, like hadronization, which cannot be described by the perturbative theory is also included.

The present thesis describes new measurements using LEP data collected by the ALEPH detector: first a measurement of the strong coupling constant alone, and then a

simultaneous measurement of the strong coupling constant and the colour factors, which represents a stringent test of QCD, will be presented in the following chapters. Such measurements have already been performed within the ALEPH collaboration, but new calculations and new Monte Carlo Programs have been available for some years now that allow for an improvement in the analysis.

The following chapters give the details of the measurements, and summarize the understanding on the performance of the new Monte Carlo programs. It all starts with an introduction to the theory of strong interactions, QCD, which can be found in Chapter 2. This is not intended to be a complete description of the theory, but tries to focus on the main concepts as well as on the more specific points which are important for the understanding of the measurement.

In the next chapter, the theoretical predictions for four-jet observables are detailed since these are the kind of observables used in the analyses of this thesis. It also includes the definition of the observables used.

Then, in Chapter 4 a description of the ALEPH detector is given. Once more, instead of an exhaustive discussion, only a brief description is given, with particular stress on the subdetectors or performances which are more relevant for the measurements presented in this work.

The next chapter contains a description of the analysis method. Details on the event selection, on the theoretical predictions and on the corrections used and on the fit procedure can be found there.

Chapter 6 gives all the details and results of the measurements. Plots of the corrections applied and of the fit results can be found there. First, the measurement of the strong coupling constant from the four-jet rate is presented. Then results on the simultaneous measurement of the strong coupling constant and the colour factors follow. Finally, a measurement to test the possible existence of a light gluino is shown.

Finally, before the conclusions, the studies performed with the new Monte Carlo pro-

grams used in the present thesis, which are not the standard for other ALEPH measurements, are described. Our present understanding of them and the limits to their applicability are discussed.

At the end of the present work an appendix summarizes the current discussions on one of the methods used for the measurement of the strong coupling constant from the four-jet rate: the experimentally optimized scale method.

Chapter 2

Theoretical framework

Jamás he podido respetar esas extrañas leyes.
Jamás lo podré disimular, luna vuela y hazme a mi volar.

2.1 Introduction

The theoretical description of hadron production in e^+e^- annihilation consists of four parts as shown in Fig. 2.1. The first part is based on the Standard Model of electroweak interactions [1]. Feynman diagrams are used to calculate the electroweak process of e^+e^- annihilation. The description of a multihadronic event starts with a pair of primary partons, quark-antiquark, distributed according to an exact (up to some order in α^{QED}) Z decay matrix element. The evolution of these primary partons under the strong interaction is described by perturbative Quantum Chromodynamics (pQCD). In a parton (or dipole) cascade, the primary partons evolve from the hard scattering scale $Q \approx \mathrm{M_Z}$ into secondary partons at a cut-off scale $Q_0 \approx 1\mathrm{GeV}$. It is during these calculable stages (hard subprocess and shower) that the event's global features are determined: energy dependences, event topologies, multiplicity, etc. In a third stage, carried out at the low virtuality scale Q_0, a model is employed to convert the secondary partons into hadrons. This hadronization process can modify the global properties of the event, but these modifications are small at the LEP energies. Finally the decay of unstable hadrons, which can be described by kinematics using experimentally measured decay rates, needs to be included before the prediction can be confronted with data.

While the standard model of particle physics provides a well tested description of the reaction $e^+e^- \to Z/\gamma^* \to q\bar{q}$, the subsequent production of observable hadrons is less well understood. The following sections try to summarize our current understanding of both

the evolution of partons under the strong interaction and the hadronization process. First, a short introduction to the Standard Model of particle physics is given. Then, a review of the perturbative theory of strong interactions is presented. Third, the problems of the non-perturbative regime, namely Soft QCD, are introduced. Finally, some details about the implementation of the current understanding of QCD in the Monte Carlo programs are given.

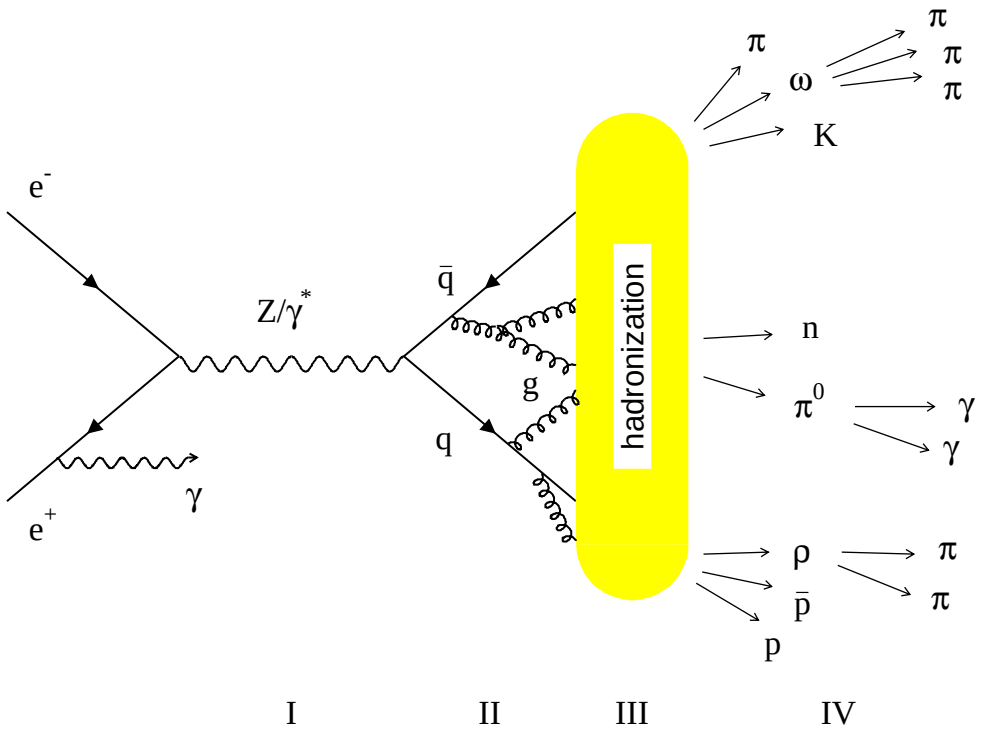

Figure 2.1: The reaction $e^+e^- \rightarrow$ *hadrons* viewed in four phases.

2.2 The Standard Model

A "standard model" is a theoretical framework, built from observations, which allows for predictions of physics phenomena. The Standard Model (SM) of particle physics [1, 2] provides a unified description of the electromagnetic, weak and strong forces in the language of quantum field theories. It has been experimentally verified with great accuracy over a wide range of energies and processes.

The SM is a quantum field gauge theory, based on the symmetry group $SU(3)_C \otimes SU(2)_L \otimes U(1)_Y$, partially characterized by the spectrum of elementary fields shown in Table 2.1. The matter fields are spin-$\frac{1}{2}$ fermions. There are three families of fermion fields, with similar properties except their masses, with the first family containing the constituents of stable matter: the up (u) and down (d) quarks (constituents of nucleons, as well as of pions and other mesons) and the electron (e) plus the electron-neutrino (ν_e). The quarks of the other two families are constituents of heavier short-lived particles. They and their companion charged leptons decay to the quarks and leptons of the first family via the weak force.

The interaction among fermions is mediated by spin-1 gauge bosons: one massless photon (γ) and eight massless gluons ($g_1, ..., g_8$) for the electromagnetic and strong interactions respectively, and three massive bosons ($W^{\pm}$ and Z) for the weak interaction.

Electrically charged particles interact due to the exchange of photons. The fact that the photon is massless accounts for the long range of the electromagnetic force.

Leptons

$$\begin{pmatrix} \nu_{e_L} \\ e_L \end{pmatrix}_{Y=-\frac{1}{2}} \quad \begin{pmatrix} \nu_{\mu_L} \\ \mu_L \end{pmatrix}_{Y=-\frac{1}{2}} \quad \begin{pmatrix} \nu_{\tau_L} \\ \tau_L \end{pmatrix}_{Y=-\frac{1}{2}}$$

$$\left(e_R\right)_{Y=-1} \quad \left(\mu_R\right)_{Y=-1} \quad \left(\tau_R\right)_{Y=-1}$$

Quarks

$$\begin{pmatrix} u_L \\ d'_L \end{pmatrix}_{Y=\frac{1}{6}} \quad \begin{pmatrix} c_L \\ s'_L \end{pmatrix}_{Y=\frac{1}{6}} \quad \begin{pmatrix} t_L \\ b'_L \end{pmatrix}_{Y=\frac{1}{6}}$$

$$\left(u_R\right)_{Y=\frac{2}{3}} \quad \left(c_R\right)_{Y=\frac{2}{3}} \quad \left(t_R\right)_{Y=\frac{2}{3}}$$

$$\left(d'_R\right)_{Y=-\frac{1}{3}} \quad \left(s'_R\right)_{Y=-\frac{1}{3}} \quad \left(b'_R\right)_{Y=-\frac{1}{3}}$$

Gauge Bosons

$$\gamma, Z, W^{\pm}, g_1, ..., g_8$$

Table 2.1: Standard Model fields. The $SU(2)_L \times U(1)_Y$ group representation of the fermion fields is explicitly shown.

Quarks carry a quantum number called *colour* which can take three different values. Coloured particles interact strongly through the exchange of gluons. Contrary to the elec-

trically neutral photon, gluons carry colour charge and hence couple to each other. This makes the strong force between two coloured particles increase with increasing distance.

Both quark and leptons carry *weak isospin* ($\vec{T}$) and *weak hyper-charge* (Y). These are quantum numbers that define the transformation under the $SU(2)_L \times U(1)_Y$ group. The $W^{\pm}$ and Z bosons couple to these "weak charges". As shown in Table 2.1, the left-(right-)handed fields transform as weak isospin doublets(singlets). As a consequence, Ws couple only to the left-handed fermions (with the spin oriented opposite to the direction of motion).

The $[d', s', b']$ weak isospin eigenstates are lineal combinations of the $[d, s, b]$ mass eigenstates. The unitary matrix relating both is the Cabbibo-Kobayashi-Maskawa matrix, which depends on four fundamental parameters of the SM: three angles and a phase. The latter provides the only mechanism within the SM that can account for the obserbed violation of CP symmetry.

The spin-1 field mediating the interactions results from the local gauge invariance of the SM Lagrangian. However, such a high degree of symmetry makes initially the theory unphysical since it predicts massless gauge bosons, while we know that for a realistic theory we need massive weak vector bosons. This problem is solved if we consider that the $SU(2)_L \times U(1)_Y$ symmetry is *spontaneously broken*.

The spontaneous symmetry breaking (SSB) mechanism is a general phenomenon which happens when the symmetric solutions of a theory are unstable and the ground state of the system is degenerated. Even if the theory is spontaneously broken, the symmetry is (in a sense) still present; it is only "hidden" by the choice of ground state. In spite of the SSB the theory can be shown to remain renormalizable [3]. This is an important property, as the renormalizability ensures that once a few parameters are determined experimentally, quantitative predictions can be calculated to arbitrary accuracy as a perturbative expansion in the coupling constant.

Therefore, in the SM the masses of the gauge fields (as well as of the fermions) are generated by SSB, ensuring that one of them (the photon) remains massless. The latter is attained by choosing a vacuum (the ground state in a quantum field theory) which only possesses $U(1)_{EM}$ symmetry. As a result of the SSB mechanism, the existence of a physical scalar particle is predicted in the minimal version of the SM, the so called Higgs boson [4].

The Higgs boson has not been observed experimentally yet, but some "hints" consistent with the production of the Higgs boson with a mass near 114 GeV/c^2 were found during the year 2000 [5]. The electroweak precision measurements made at LEP1, SLD and ν-Nucleon scattering experiments have some sensitivity to $\log(M_H)$ through loop corrections, and allow to constrain $\log(M_H)$ to be $1.78^{+0.27}_{-0.28}$ at 68% confidence level [6].

2.3 The Perturbative Theory of Strong Interactions

The most fundamental statement of QCD is that hadronic matter is made of quarks. This idea was born from the need to have a physical manifestation for the $SU(3)$ symmetry of flavour observed in the spectrum of the lowest-mass mesons (two-quark states) and baryons (three-quark states). The quarks in the baryons have to be half-integral spin states in order to account for the spins of low-mass baryons. In particular the quarks in a spin-3/2 baryon are in a symmetrical state of space, spin and $SU(3)_f$ degrees of freedom. Then the introduction of the colour degree of freedom was needed to avoid a violation of the Fermi-Dirac statistics.

A colour quantum number (QN) a is then carried by each quark. This QN can take three values (namely, red, green and blue) and in this QN the baryon wave functions are totally antisymmetric. In order not to create a proliferation of states with the introduction of this QN, the requirement is added that only colour singlet states can exist in nature. This lead to $SU(3)$ to be the group of colour transformations, with the quarks transforming according to the fundamental representation and antiquarks according to the complex conjugate one. The experiments thought to prove the existence of such point-like constituents went further than expected. The quarks were found to be not enough to explain the properties of hadrons. It was in this context that the QCD improved parton model [7] was constructed, with coloured quarks and gluons as the (up to now) final constituents of matter. The last fundamental statement came to explain why free quarks are not observed in nature. If they are not observed then a strong interaction should bind them together to form hadrons. *Asymptotic freedom* predicts that the coupling of quarks and gluons is large at large distances so as to confine quarks. At the same time the coupling is predicted to be small at short distances so that the quarks behave as free particles at asymptotically large energies.

2.3.1 The Lagrangian of Strong Interactions

The QCD Lagrangian density is given by

$$\mathcal{L}_{QCD} = \sum_{flavours} \bar{q}_a (i\gamma^\mu D_\mu - m_q)_{ab} q_b - \frac{1}{4} F^A_{\mu\nu} F^{A\mu\nu} + \mathcal{L}_{gauge-fixing} + \mathcal{L}_{ghost} \tag{2.1}$$

where the sum runs over the N_f different flavours of the quarks. The first two terms describe the interaction of spin-1/2 quarks of mass m and massless spin-1 gluons. $F^A_{\mu\nu}$ is the field strength tensor derived from the gluon field $\mathcal{A}^A_\alpha$ as

$$F^A_{\alpha\beta} = [\partial_\alpha \mathcal{A}^A_\beta - \partial_\beta \mathcal{A}^A_\alpha - g f^{ABC} \mathcal{A}^B_\alpha \mathcal{A}^C_\beta] \tag{2.2}$$

where the capital indices run over the eight colour degrees of freedom of the gluon field, g is the coupling constant which determines the strength of the interaction between coloured quanta, and f^{ABC} are the structure constants of the colour group, $SU(3)$. The third term in Eq. 2.2 shows the non-Abelian nature of QCD, which distinguishes this theory from QED. It gives rise to triplet and quartic gluon self-interactions and, ultimately, to asymptotic freedom. In non-Abelian theories, the covariant gauge-fixing term must be supplemented by a *ghost* term, which will not be discussed here as it is not relevant for what follows.

The quark fields q_a in Eq. 2.1 are in the triplet representation of the colour group and D is the covariant derivative, which acting on triplet fields takes the form:

$$(D_\alpha)_{ab} = \partial_\alpha \delta_{ab} + ig \left(t^C \mathcal{A}^C_\alpha\right)_{ab} \tag{2.3}$$

where the generators of $SU(3)$, t, are matrices in its fundamental representation and fulfill the relation

$$\left[t^A, t^B\right] = i f^{ABC} t^C \quad . \tag{2.4}$$

By convention the normalization of the $SU(N)$ matrices is chosen to be

$$T_r \left(t^A t^B\right) = T_R \delta^{AB}, \qquad T_R = \frac{1}{2} \quad . \tag{2.5}$$

With this choice, the colour matrices obey the following relations:

$$\sum_A t^A_{ab} t^A_{bc} = C_F \delta_{ac}, \qquad C_F = \frac{N^2 - 1}{2N} \tag{2.6}$$

$$\sum_{A,B} f^{ABC} f^{ABD} = C_A \delta^{CD}, \qquad C_A = N. \tag{2.7}$$

Thus for the specific case of $SU(3)$ we have

$$C_F = \frac{4}{3}, \qquad C_A = 3 \tag{2.8}$$

which are called the *colour factors*. They are related to the emission of a gluon by a quark and the splitting of a gluon into two other gluons, respectively. On the other hand, T_R in Eq. 2.5 is related to the rate of gluon splitting into quarks of one flavour.

2.3.2 Gauge Invariance

The QCD Lagrangian is invariant under local gauge transformations, i.e. the quark fields can be redefined independently, but not arbitrarily, at every point in space-time without changing the physical content. The behaviour of a quark field under such a local transformation is:

$$q_a(x) \rightarrow \exp\left(it \cdot \theta(x)\right) q_b(x) \tag{2.9}$$

and the covariant derivative is so called because it transforms in the same way as the field itself:

$$D_\alpha q(x) \rightarrow \exp\left(it \cdot \theta(x)\right) D_\alpha q(x) \quad . \tag{2.10}$$

From the previous equations the transformation of the gluon gauge field and the field strength can be obtained (see e.g. reference [8]) and it is observed that, in contrast to QED, the QCD field strength is not gauge invariant due to the self-interaction of gluons.

There is no gauge-invariant way of including a gluon mass, because the term $m^2 \mathcal{A}^\alpha \mathcal{A}_\alpha$ is not gauge invariant. This property is similar to QED where a massive photon is forbidden.

The gauge fixing explicitly breaks gauge invariance. However, in the end physical results will be independent of the gauge. The *ghost* term, that supplements the covariant gauge-fixing term, cancels the unphysical degrees of freedom of the gluon.

2.3.3 The Running Coupling

In a quantum field theory the calculation of a dimensionless observable R as a perturbation series in $\alpha_s = g/4\pi$, where R depends on a large energy scale Q, requires renormalization

to remove ultraviolet divergences. Such divergences come from loop corrections, such as those depicted in Fig. 2.2, which diverge for infinitely large momenta.

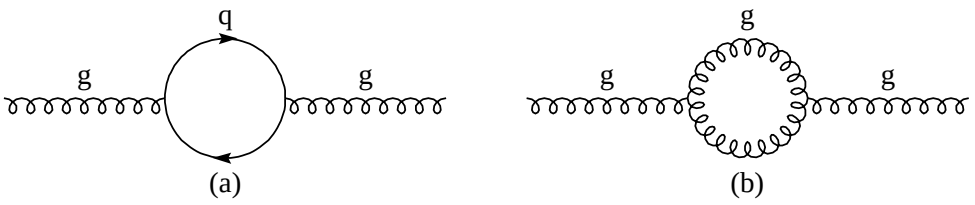

Figure 2.2: Loop corrections to the gluon propagator: (a) quark loop , (b) gluon loop.

Through renormalization the divergent terms are absorbed into the "bare" quantities of the theory, such as the coupling, the masses or the field normalizations, which are not observables, thus defining new renormalized quantities, which are measurable. This process introduces a second mass scale μ, at which the subtractions which remove the divergences are performed. R depends on the non-constant ratio Q/μ. The renormalized coupling also depends on μ.

Since μ is an arbitrary parameter, R cannot depend on μ when the coupling is fixed. Moreover, since R is dimensionless, it can only depend on Q^2/μ^2 and on the renormalized coupling α_s. Hence

$$\mu^2 \frac{d}{d\mu^2} R\left(\frac{Q^2}{\mu^2}, \alpha_s\right) \equiv \left[\mu^2 \frac{\partial}{\partial \mu^2} + \mu^2 \frac{\partial \alpha_s}{\partial \mu^2} \frac{\partial}{\partial \alpha_s}\right] R = 0 \tag{2.11}$$

which is called the renormalization group equation. Introducing $\tau = \ln\left(\frac{Q^2}{\mu^2}\right)$, and $\beta(\alpha_s) \equiv \mu^2 \frac{\partial \alpha_s}{\partial \mu^2}$, the renormalization group equation can be written as

$$\left[-\frac{\partial}{\partial \tau} + \beta(\alpha_s) \frac{\partial}{\partial \alpha_s}\right] R = 0 \tag{2.12}$$

which is solved by defining the running coupling $\alpha_s(Q)$,

$$\tau = \int_{\alpha_s}^{\alpha_s(Q)} \frac{dx}{\beta(x)} \tag{2.13}$$

where $\alpha_s(\mu) \equiv \alpha_s$. Thus all scale dependence in R comes from the running of $\alpha_s(Q)$. A change in the renormalization scale is compensated by a change of the coupling, and the physical observable R remains independent of the unphysical scale μ^2. However, this only holds if R is calculated at all orders of α_s, otherwise an explicit scale dependence appears at one order higher than the order at which the variable has been calculated.

The Beta Function

The running of the QCD coupling, α_s, is determined by the QCD β function, which has the expansion:

$$\beta(\alpha_s) = -b\alpha_s^2 \left(1 + b'\alpha_s + \mathcal{O}(\alpha_s^2)\right) \tag{2.14}$$

where

$$b = \frac{11C_A - 2N_f}{12\pi} \qquad b' = \frac{17C_A^2 - 5C_A N_f - 3C_F N_f}{2\pi(11C_A - 2N_f)} \tag{2.15}$$

with N_f the number of active flavours.

The β coefficients in general depend on the renomalization scheme used, hence also the running coupling. In this analysis the modified minimal subtraction renormalization scheme ($\overline{\text{MS}}$) is used. The first two terms of the expansion for β are, in fact, scheme independent. From the definition of the β function and neglecting b' and higher order coefficients in Eq. 2.14 the following solution can be extracted,

$$\alpha_s(Q^2) = \frac{\alpha_s(\mu^2)}{1 + \alpha_s(\mu^2) b \ln \frac{Q^2}{\mu^2}} \quad . \tag{2.16}$$

Quark loop diagrams contribute to the negative N_f term in b, while gluon loop diagrams give a positive C_A contribution which makes an overall negative β function. This is in contrast to QED, where the b coefficients have opposite signs. Then, as Q becomes large, $\alpha_s(Q)$ decreases to zero. This property of QCD, which depends on the sign of b, is called asymptotic freedom. It is this property that allows reliable predictions from perturbation theory for processes involving high momentum transfers. In QED where b is negative, the coupling increases at large Q.

2.3.4 The Lambda Parameter

Perturbative QCD tells us how $\alpha_s(Q)$ varies with Q, but its absolute value has to be obtained from experiment. Nowadays, the value of the coupling at $Q = \mathrm{M_Z}$ is used as the fundamental parameter , which is a convenient reference scale large enough to be in the perturbative regime.

However, it is also useful to express $\alpha_s(Q)$ in terms of a dimensionfull parameter (constant of integration) Λ,

$$\ln \frac{Q^2}{\Lambda^2} = -\int_{\alpha_s(Q)}^{\infty} \frac{dx}{\beta(x)} = \int_{\alpha_s(Q)}^{\infty} \frac{dx}{bx^2(1+b'x+...)} \quad . \tag{2.17}$$

Then, if the perturbative theory were the whole story, $\alpha_s(Q) \to \infty$ as $Q \to \Lambda$. Thus Λ sets the scale at which $\alpha_s(Q)$ becomes large.

In next-to-leading order (NLO) we have

$$\alpha_s(Q) = \frac{1}{b\ln(Q^2/\Lambda^2)}\left[1 - \frac{b'}{b}\frac{\ln\ln(Q^2/\Lambda^2)}{\ln(Q^2/\Lambda^2)}\right] \quad . \tag{2.18}$$

The Λ parameter depends on the number of active flavours, N_f, where active means $m_q \lesssim Q$. Thus for $5 \lesssim Q \lesssim 175$ GeV, $N_f = 5$. It also depends on the renormalization scheme. So, taking as current best fit value of α_s at the Z pole [9]

$$\alpha_s(\mathrm{M_Z}) = 0.1184 \pm 0.0031 \tag{2.19}$$

the corresponding preferred value of $\Lambda_{\overline{\mathrm{MS}}}$ for $N_f = 5$ falls in the range:

$$178 \text{ MeV} < \Lambda_{\overline{\mathrm{MS}}}(5) < 251 \text{ MeV}.$$

2.4 The Non-Perturbative Regime of Strong Interactions

The transition from the quark and gluon degrees of freedom appropriate in perturbation theory to the hadrons observed by real world experiments is poorly understood. In this strongly interacting transition regime we presently rely on models, which to varying degrees reflect possible scenarios for the QCD dynamics.

Corresponding to asymptotic freedom at high momentum scales (short distances), we have infrared slavery: $\alpha_s(Q)$ becomes large at low momenta (long distances). pQCD is not reliable anymore, and non-perturbative methods, such as lattice calculations, must be used. Lattice QCD is QCD formulated on a discrete Euclidean space-time grid. The discrete space-time lattice acts as a non-peturbative regularization scheme. At finite values of the lattice spacing a there are no infinities. Furthermore, renormalized physical quantities have a finite well behaved limit as $a \to 0$. This subfield of the particle theory attempts to solve QCD problems in the regime of the nuclear matter, i.e. at the scale of the hadronic world. Its aim is the calculation of correlation functions of hadronic operators and matrix elements of any operator between hadronic states in terms of the

fundamental quark and gluon degrees of freedom.

There are two important low momentum-scale phenomena:
Confinement: partons (quarks and gluons) are found only in colour-singlet bound states, called hadrons, of size ≈ 1 fm. If an attempt to isolate the partons within a hadron is done, it becomes energetically favourable to create extra partons, forming additional hadrons. This is a static (long-distance) property of QCD, which can be treated by lattice techniques.
Hadronization: partons produced in short distance interactions reorganize themselves (and multiply) to make the observed hadrons. This is a dynamical (long-timescale) phenomenon, where only phenomenological models are available at present.

2.4.1 Infrared Divergences

Even in the high-energy, short-distance regime, long-distance aspects of QCD cannot be ignored. Soft or collinear gluon emission gives infrared divergences in pQCD. Light quarks ($m_q \ll \Lambda$) also lead to divergences in the limit $m_q \to 0$.

pQCD can still be used to perform calculations, provided that the study is limited to two classes of observables:

Infrared- and collinear-save quantities, i.e. those insensitive to soft or collinear branching. Infrared divergences in pQCD either cancel between real and virtual contributions or are removed by restricting the phase space through an integration cut-off. Such quantities are determined primarily by hard, short-distance physics; long-distance effects give power corrections, suppressed by inverse powers of a large momentum scale.

Factorizable quantities, i.e. those in which infrared sensitivity can be absorbed into an overall non-perturbative factor, to be determined experimentally.

2.5 The implementation of QCD in Monte Carlo Models

The whole chain, from the e^+e^- annihilation to the hadronization and decay of unstable hadrons, has been implemented in Monte Carlo programs, which make it possible to generate multihadronic final states. An important aspect of the hadronic decay of the Z boson is that the final state hadrons generally form jets, i.e. they are not arbitrarily spread out in phase space, but stay rather close together (see Fig. 2.3). The direction and energies of these jets are in close correspondence with the directions and energies of the primary high energetic partons. More precisely, hadrons are formed out of the colour

field with limited transverse momentum, which is independent of the hard energy scale. Therefore, the higher the energy of the primary parton, the stronger is the collimation of hadrons around its direction. An event, where the primary quarks do not radiate any energetic gluons will typically appear as two back-to-back "bundles" of hadrons, whereas events with one or more high energy gluons, radiated off at sufficiently large angles, will give rise to additional hadronic jets.

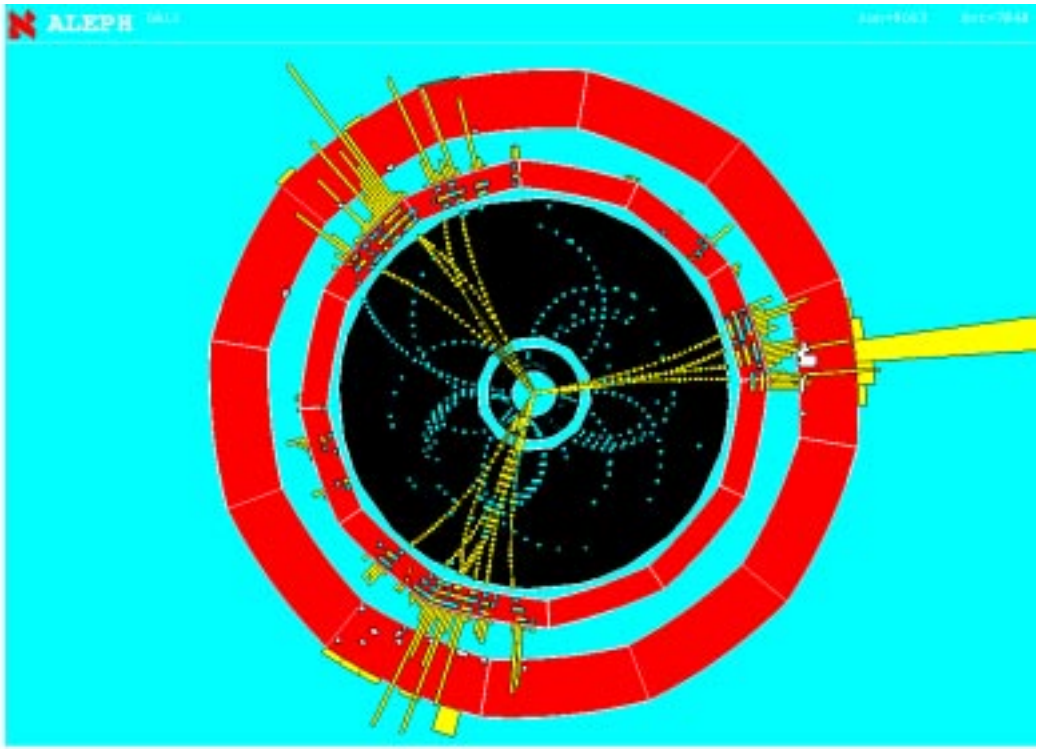

Figure 2.3: A three-jet hadronic event recorded with the ALEPH detector.

The most popular Monte Carlo programs that try to simulate all the properties of the electron-positron annihilation into hadrons are PYTHIA (JETSET) and HERWIG [10, 11]. PYTHIA combines a *Parton Shower* (PS) algorithm with the Lund string fragmentation. HERWIG is also based on a PS, but models the hadronization via cluster fragmentation. Some details about the PS implementation and about the string and cluster fragmentation models are given in the following sections.

2.5.1 Perturbative QCD: the approximation through a Parton Shower

Complete perturbative calculations in QCD have been performed only to next-to-leading order in most cases, or to one further order in α_s for a few observables. The effort for the calculation of a new term increases roughly factorially with the order, so not many more higher-order terms are expected to be calculated soon. Nevertheless there are regions of phase space in which higher-order terms are enhanced and cannot be neglected.

In the present section an approximate result in which such enhanced terms are taken into account to all orders will be shown. This will lead to a physically appealing parton shower picture which can readily be implemented in computer simulations. The parton shower represents an approximate perturbative treatment of QCD dynamics at scales of momentum transfer-squared t greater than some infrared cut-off value t_0, typically taken to be of the order of 1 GeV^2.

Parton Branching

Assume the branching of a parton a into $b + c$ as shown in Fig. 2.4. a is defined as an outgoing parton, i.e. the time-like branching is chosen. The opening angle is $\theta = \theta_b + \theta_c$ and the energy fraction is $z = E_b/E_a = 1 - E_c/E_a$. Thus, for small angles and massless partons, where the matrix element is enhanced, the following expression holds,

$$t = 2E_bE_c\,(1 - \cos\theta) = z(1 - z)E_a^2\theta^2 \tag{2.20}$$

hence, using transverse momentum conservation,

$$\theta = \frac{1}{E_a}\sqrt{\frac{t}{z(1 - z)}} = \frac{\theta_b}{1 - z} = \frac{\theta_c}{z} \quad . \tag{2.21}$$

Consider the different cases, i.e. a,b and c being gluons, a being a gluon and b and c a quark-antiquark pair, and a and b being quarks and c a gluon. Then the unregularized Dokshitzer-Gribov-Lipatov-Altarelli-Parisi (DGLAP) splitting kernels can be obtained (a detailed calculation can be found in [8]):

$$\hat{P}_{qq}(z) = C_F\frac{1 + z^2}{1 - z} \tag{2.22}$$

$$\hat{P}_{gg}(z) = C_A\frac{(1 - z(1 - z))^2}{z(1 - z)} \tag{2.23}$$

$$\hat{P}_{qg}(z) = T_F\left(z^2 + (1 - z)^2\right) \tag{2.24}$$

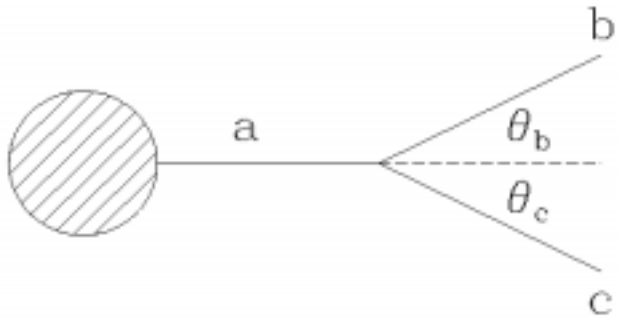

Figure 2.4: Kinematics of time-like parton branching.

The cross section for the various branching processes can be written as:

$$d\sigma_{n+1} = d\sigma_n \frac{dt}{t} dz \frac{\alpha_s}{2\pi} \hat{P}_{ba}(z) \quad . \tag{2.25}$$

A simple probabilistic picture can be adopted here. The cross section in n-th order is corrected by the probability for the additional branching of an outgoing parton, and this probability is given by $\alpha_s \hat{P}(z) dz\, dt/t$. The integration over a properly defined phase-space region will then lead to

$$\sigma_n \propto \alpha_s^n L^m, \quad m = 2n, 2n-1, ... \tag{2.26}$$

with L again some logarithm of a cut-off parameter in order to avoid singular regions. When approaching singular regions of the phase space, this logarithm will grow, and even for small α_s one will find large corrections. It becomes clear that the effective perturbative expansion parameter is not α_s any more, but rather $\alpha_s L$ or $\alpha_s L^2$, which can approach $\mathcal{O}(1)$ for a large logarithm. Hence the series in this new expansion parameter has to be resummed in all orders, if a meaningful prediction from perturbative theory ought to be obtained. This can be done through the solution of evolution equations, which are introduced in the next section.

The DGLAP Evolution Equations

The DGLAP evolution equations are typically derived within the framework of deep-inelastic scattering (see for example [8]). These are space-like processes, however, similar evolution equations can also be derived for time-like processes such as e^+e^- annihilation into $q\bar{q}$ with subsequent gluon radiation. For simplicity, we consider only a single type of

branching, the multiple gluon emission from a time-like quark, originating from a Z decay. A quark with initial virtuality $\approx Q^2$ evolves down in virtuality via successive small-angle gluon emissions. Eventually a lower scale t_0 is reached where non-perturbative (long-distance) effects become dominant.

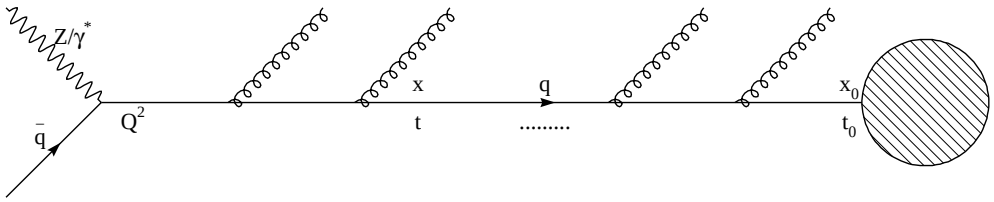

Figure 2.5: Final state branching in $e^+e^- \to q\bar{q}$.

The momentum fraction distribution, fraction with respect to the initial momentum, $D(x,t)$ of the evolving quark at some scale t gets infinitely large contributions from arbitrarily soft and collinear gluon radiation if the scale is small. However, the change of the distribution at some scale caused by additional radiation of a gluon is calculable. First we introduce a pictorial representation of the evolution, where every sequence of branchings is represented by a path in (t,x)-space, see Fig. 2.6. Each branching corresponds to a step downwards, from a higher to a lower value of the momentum fraction x, at a value of t equal to the virtual mass-squared after the branching. The change in the parton distribution $D(x,t)$ when t is increased to $t+\delta t$ is just the number of paths arriving in the element $(\delta t, \delta x)$ minus the number leaving that element, divided by δx. To find the total number arriving, we must integrate the branching probability times the parton density over all higher momentum fractions $x' = x/z$, to obtain

$$\begin{aligned} \delta D(x,t) &= \frac{\delta t}{t}\int_x^1 dx' dz \frac{\alpha_s}{2\pi}\hat{P}(z) D(x',t)\delta(x-zx') \\ &= \frac{\delta t}{t}\int_0^1 \frac{dz}{z}\frac{\alpha_s}{2\pi}\hat{P}(z) D(x/z,t) \end{aligned} \tag{2.27}$$

where $\hat{P}(z)$ is the relevant unregularized splitting function. For the number leaving the element, we integrate instead over all lower momentum fractions $x' = zx$:

$$\begin{aligned} \delta D_{out}(x,t) &= \frac{\delta t}{t} D(x,t)\int_0^x dx' dz \frac{\alpha_s}{2\pi}\hat{P}(z)\delta(x'-zx) \\ &= \frac{\delta t}{t} D(x,t)\int_0^1 dz \frac{\alpha_s}{2\pi}\hat{P}(z) \end{aligned} \tag{2.28}$$

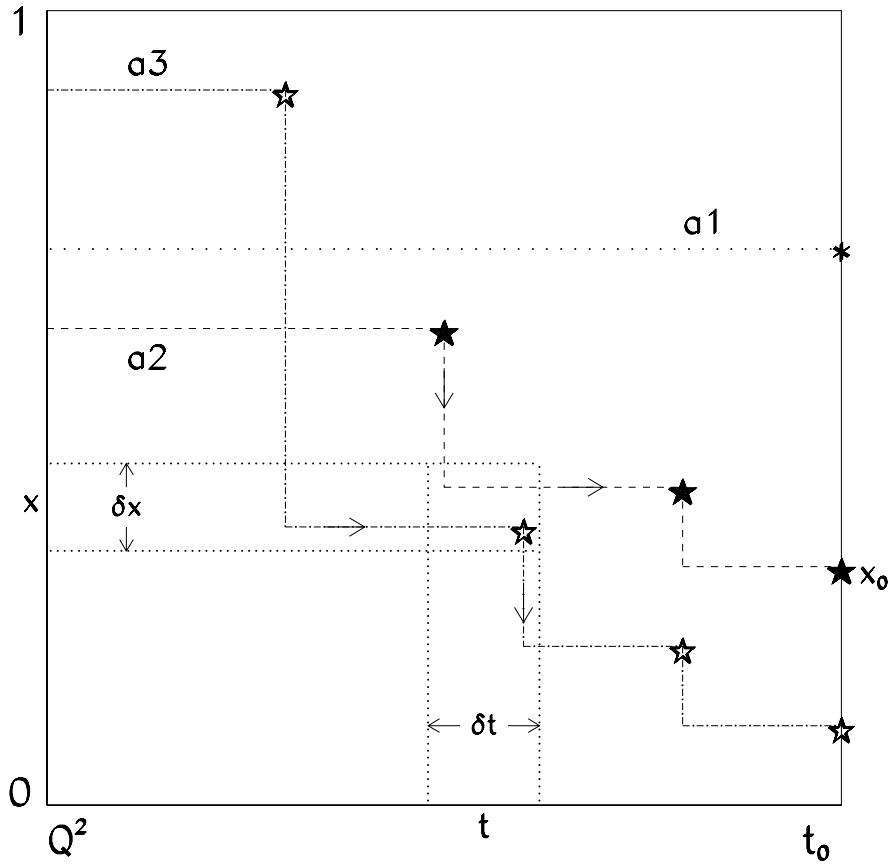

Figure 2.6: Representation of parton branching by paths in (t,x)-space. Three possible paths are indicated.

The net change in the population of the element is thus

$$\delta D(x,t) = \delta D_{in} - \delta D_{out} = \frac{\delta t}{t}\int_0^1 dz \frac{\alpha_s}{2\pi}\hat{P}(z)\left[\frac{1}{z}D(x/z,t) - D(x,t)\right]. \tag{2.29}$$

The singularity at $z = 1$ in $\hat{P}(z)$ is damped by the difference $[\frac{1}{z}D(\frac{x}{z},t) - D(x,t)]$, thus the whole expression is well defined. A compact notation is obtained by the introduction of the *plus-prescription*

$$\int_0^1 dx f(x) g(x)_+ = \int_0^1 dx \left[f(x) - f(1)\right] g(x). \tag{2.30}$$

Using this plus-prescription, the regularized splitting functions are defined

$$P(z) = \hat{P}(z)_+ \tag{2.31}$$

in terms of which the evolution equation for the parton density may be written as

$$t\frac{\partial}{\partial t}D(x,t) = \int_x^1 \frac{dz}{z}\frac{\alpha_s}{2\pi}P(z)D(x/z,t). \tag{2.32}$$

When there are several different types of partons in the branching process, the evolution equation has to be generalized to take into account the different processes by which a parton of type i can enter or leave the element $(\delta t, \delta x)$. This leads to a coupled set of evolutions equations of the form

$$t\frac{\partial}{\partial t}D_i(x,t) = \sum_j \int_x^1 \frac{dz}{z}\frac{\alpha_s}{2\pi}P_{ij}D_j(x/z,t)\,. \tag{2.33}$$

The above formulation of the DGLAP equations is convenient for obtaining analytical solutions for the evolution of parton distributions. Introducing the *Sudakov form factor*

$$\Delta(t) \equiv \exp\left[-\int_{t_0}^t \frac{dt'}{t'}\int dz \frac{\alpha_s}{2\pi}\hat{P}(z)\right]\,, \tag{2.34}$$

we can write Eq. 2.32 as

$$t\frac{\partial}{\partial t}D(x,t) = \int \frac{dz}{z}\frac{\alpha_s}{2\pi}\hat{P}(z)D(x/z,t) + \frac{D(x,t)}{\Delta(t)}t\frac{\partial}{\partial t}\Delta(t) \tag{2.35}$$

and hence

$$t\frac{\partial}{\partial t}\left(\frac{D(x,t)}{\Delta(t)}\right) = \frac{1}{\Delta(t)}\int \frac{dz}{z}\frac{\alpha_s}{2\pi}\hat{P}(z)D(x/z,t)\,. \tag{2.36}$$

This equation can be integrated to give an integral equation for $D(x,t)$ in terms of the initial parton distribution $D(x,t_0)$:

$$D(x,t) = \Delta(t)D(x,t_0) + \int_{t_0}^t \frac{dt'}{t'}\frac{\Delta(t)}{\Delta(t')}\int \frac{dz}{z}\frac{\alpha_s}{2\pi}\hat{P}(z)D(x/z,t')\,. \tag{2.37}$$

The first term on the right-hand side is the contribution from paths that do not branch between scales t and t_0. Thus the Sudakov form factor $\Delta(t)$ is simply the probability of evolving from t to t_0 without branching. The second term is the contribution from all paths which have their last branching at scale t'. The factor $\Delta(t)/\Delta(t')$ represents the probability of evolving from t to t' without branching.

In the present discussion for the Sudakov form factor, the infrared singularity of the unregularized splitting functions at $z = 1$ has been ignored. However, this singularity is removed, in order for the form factors to be defined, through an infrared cut-off, $z < 1 - \epsilon(t)$. Branchings with z above this range are classified as *unresolvable*: they involve emission of an undetectable soft parton. The Sudakov form factor with this cut-off

then gives the probability of evolving from t to t_0 without any resolvable branching.

Although no virtual corrections have been mentioned explicitly, the Sudakov form factor in fact sums enhanced virtual (parton loop) as well as real (parton emission) contributions to all orders. The virtual corrections affect the no-branching probability, and are included via unitarity, which is just the fact that the sum of the branching and no-branching probabilities must be unity. The resolvable branching probability tells us via unitarity the sum of the virtual and unresolvable real contributions: the latter two are both divergent but their sum is finite, and included consistently in Eq. 2.36.

A natural cut-off for the branching would be that the virtual mass-squared $t > t_0$, which can be translated into

$$z(1-z) > t_0/t \quad . \tag{2.38}$$

This follows from the condition of positive transverse momentum, as shown in [8],

$$p_\perp^2 = z(1-z)p_a^2 - (1-z)p_b^2 - zp_c^2 > 0 \tag{2.39}$$

and $p_a^2 = t, p_b^2, p_c^2 > t_0$. The cut-off condition can be approximated to

$$\frac{t_0}{t} < z < 1 - \frac{t_0}{t}\,. \tag{2.40}$$

A further refinement consists in the usage of the running coupling with a properly chosen scale. As a first guess, the scale for the running could be set to the virtuality of the branching parton. However, a more careful treatment suggests [12] that $z(1-z)t$ should be used as its argument, which is essentially the transverse momentum squared. By doing this , terms of the form $\ln(1-z)/(1-z)$ are resummed, which are found in next-to-leading calculations of the splitting functions.

Finally the Sudakov form factor for a single branching type becomes

$$\Delta(t) = \exp\left[-\int_{2t_0}^{t}\frac{dt'}{t'}\int_{t_0/t'}^{1-t_o/t'} dz\frac{\alpha_s[z(1-z)t']}{2\pi}\hat{P}(z)\right]\,. \tag{2.41}$$

Monte Carlo Method

The formulation of parton branching in terms of the Sudakov form factor is well suited to computer implementation, and is the basis of the parton shower Monte Carlo programs for simulating QCD jets. The basic Monte Carlo branching algorithm in its simplest form

is described in the following lines, neglecting the complications for the different possible branchings and QCD coherence effects.

The basic problem that the Monte Carlo branching algorithm has to solve is as follows: given the virtual mass scale and momentum fraction (t_1, x_1) after some step of the evolution, or as initial conditions, generate the values (t_2, x_2) after the next step. The first quantity to be generated by the algorithm is the value of t_2. It was shown that for a time-like branching the probability of evolving from t_1 to t_2 without (resolvable) branching is $\Delta(t_1)/\Delta(t_2)$ where $\Delta(t)$ is the Sudakov form factor. Thus t_2 can be generated with the correct probability distribution by solving the equation

$$\frac{\Delta(t_1)}{\Delta(t_2)} = \mathcal{R} \tag{2.42}$$

where $\mathcal{R}$ is a random number distributed uniformly in the interval $[0, 1]$. If the value of t_2 is lower than t_0, this means that no further branching occurs. Otherwise, we have to generate the value of the momentum fraction $x = x_2/x_1$ for the next branching, with a probability distribution proportional to $(\alpha_s/2\pi)P(z)$, where $P(z)$ is the appropriate splitting function. This can be done by solving the equation

$$\int_{\epsilon}^{x_2/x_1} dz \frac{\alpha_s}{2\pi} P(z) = \mathcal{R}' \int_{\epsilon}^{1-\epsilon} dz \frac{\alpha_s}{2\pi} P(z) \tag{2.43}$$

where $\mathcal{R}'$ represents another random number in the interval $[0, 1]$ and ϵ is the infrared cut-off for resolvable branching.

The values of (t_i, x_i) generated by successive applications of the algorithm define the virtual masses and momentum fractions of the exchanged parton, from which the momenta of the emitted gluons can be computed. The azimuthal angles of their emission need to be specified by a further Monte Carlo algorithm. Each emitted gluon and in general each parton with time-like momentum in a parton shower, can itself undergo further branching, which can be dealt with by a similar algorithm. As a consequence of successive time-like branchings, a parton cascade develops. Each outgoing line becomes the source of a new cascade, until the Monte Carlo algorithm generates a no-branching step in the evolution of its virtual mass. Those that do branch produce partons of lower virtual masses, which become more likely to generate no branching. Eventually all outgoing lines have stopped branching and the cascade ceases. At this stage, which depends on the cut-off scale t_0, the outgoing partons have to be converted into hadrons via the hadronization model if the Monte Carlo program is to be used for the simulation of real events. Different available models are described in Section 2.5.2.

2.5.2 Soft QCD

The bulk properties of hadronic events in Z decay are established early in the fragmentation when virtualities are large and pQCD is valid. However, the issue of to what extent pQCD dominates and what are the contributions coming from non-perturbative effects is still under investigation.

It was already stated that the final state hadrons form jets with directions and energies quite close to the ones of the primary high energetic partons. The fact that soft QCD does not heavily modify the properties of these jets might be a result of several effects. First multiple gluon radiation is restricted in phase space such that subsequent soft gluons can not be radiated at arbitrarily large angles (this is called *angular ordering*). Second, the hadronization phase involves only small momentum transfers, thus the main topological properties of the event remain almost untouched.

Therefore, the interface between perturbative an soft QCD is implemented at two levels in Monte Carlo programs as HERWIG and PYTHIA, which are the ones used in the analyses described in Chapter 6. Soft Gluon Emission is introduced in the parton shower, which also includes our knowledge on pQCD. Then, at the end of the shower the partons undergo hadronization. Different models are used in the MCs, namely string and cluster models. In some cases the parton shower is not used, and the partons coming from the matrix element expressions are directly hadronized (this option is only implemented in PYTHIA).

i) Soft Gluon Emission

The parton branching formalism discussed so far takes account of collinear enhancements to all orders in perturbative theory. However, there are also soft enhancements due to gluon emission. The singularities of the small-angle parton splitting functions for soft gluon emission have already appeared in the previous section. However, the enhancement due to soft gluon emission has more general contributions. Whenever an external line of a QCD Feynman graph with momentum p and mass m (not necessarily small) emits a gluon with momentum q and energy ω, a divergence as $\omega \to 0$ appears for any velocity and emission angle. Notice that there is no soft enhancement of radiation from an off-mass-shell internal line of a Feynman graph, since the associated denominator factor does not diverge when $\omega \to 0$.

The enhancement factor in the amplitude for each external line implies that the cross section enhancement has a factor which is the sum over all pairs of external lines $\{i, j\}$ [8]:

$$d\sigma_{n+1} = d\sigma_n \frac{d\omega}{\omega} \frac{d\Omega}{2\pi} \frac{\alpha_s}{2\pi} \sum_{i,j} C_{ij} W_{ij} \tag{2.44}$$

where $d\Omega$ is the element of solid angle for the emitted gluon, C_{ij} is a colour factor, and the radiation function W_{ij} is given by

$$W_{ij} = \frac{\omega^2 p_i \dot{p}_j}{p_i \dot{q} p_j \dot{q}} = \frac{1 - v_i v_j \cos\theta_{ij}}{(1 - v_i \cos\theta_{iq})(1 - v_j \cos\theta_{jq})} \tag{2.45}$$

with v_i the velocity of the i-th particle. The radiation function can be separated into two parts, containing the collinear singularities along lines i and j. For simplicity we consider massless particles ($v_{\mathrm{i,j}} = 0$). Then, $W_{ij} = W_{ij}^i + W_{ij}^j$ where

$$W_{ij}^i = \frac{1}{2}\left(W_{ij} + \frac{1}{1 - \cos\theta_{iq}} - \frac{1}{1 - \cos\theta_{jq}}\right) \quad . \tag{2.46}$$

This function has the property of angular ordering. After the azimuthal averaging, the contribution of W_{ij}^i is confined to a cone, centered on the direction of i, extending in angle as far as the direction of line j.

Angular ordering is the coherence effect common to all gauge theories. In QED it causes the Chudakov effect, i.e. the suppression of soft bremsstrahlung from e^+e^- pairs. In QCD the angular ordering provides the basis for the coherent parton branching formalism, which includes soft gluon enhancements to all orders. For two external lines forming a colour singlet, as in $e^+e^- \to q\bar{q}$, the angular ordering operates as in QED suppressing the radiation outside the cones extending from i to j and vice-versa. A more interesting case is that of three partons (i, j, k) forming a colour singlet, such as $e^+e^- \to q\bar{q}g$. There, each of the partons i, j and k radiates in proportion to its colour charge squared. When i and j are close in angle, their incoherent contributions are limited (after azimuthal averaging) to cones of half-angle θ_{ij}. At larger angles, out to the direction of k, they give coherent contributions in proportion to their combined colour charge squared. This contribution can be computed as if it came from an internal line of momentum $p_l = p_i + p_j$, but in reality it comes coherently from the two external lines.

The above treatment can be extended to higher orders leading to a coherent parton branching formalism that can be used to compute soft gluon enhancement to all orders. The rules for coherent branching involve a simple modification of those for the collinear branching process seen in Section 2.5.1. Such modifications are detailed in [8] and they

lead to the Sudakov form factor for the coherent branching process,

$$\tilde{\Delta}(t) = \exp\left[-\int_{4t_0}^{t}\frac{dt'}{t'}\int_{\sqrt{t_0/t'}}^{1-\sqrt{t_0/t'}}\frac{dz}{2\pi}\alpha_s\left(z^2(1-z)^2t'\right)\hat{P}(z)\right]. \tag{2.47}$$

ii) **Hadronization**

One general approach to hadronization, based on the observation that perturbation theory seems to work well down to rather low scales, is the hypothesis of local parton-hadron duality. Here one only supposes that the flow of momentum and quantum numbers at the hadron level tends to the flow established at the parton level. Thus, for example, the flavour of the quark initiating a jet should be found in a hadron near the jet axis. The extent to which the hadron flow deviates from the parton flow reflects the irreducible smearing of order Λ due to hadron formation. However more explicit hadronization models are needed in order to compute detailed predictions. The two classes of models used in the analysis of this thesis are briefly described in the following paragraphs.

String Model

In an e^+e^- annihilation, neglecting the possibility of gluon bremsstrahlung, the produced quark and antiquark move out in opposite direction, losing energy to the colour field, which is supposed to collapse into a string-like configuration between them. Mesons and baryons are created by tunneling effects or equivalently by the breakup of the colour tube. This *Lund Model* [13] is inspired by the idea that because of the self-coupling of the gluons, an effective anti-screening of the bare colour charge occurs and the field between colour charges is restricted to a flux tube. Hence describing the gluon field as a flux tube with constant energy per unit length, leading to a linearly rising potential, at increasing distance between colour charges the attractive force stays constant instead of decreasing, as is the case for the electro-magnetic force. Eventually the energy in the colour field becomes so large that $q\bar{q}$ pairs are created from the vacuum, which afterwards combine to form colour-neutral states. An schematic view of the string model is shown in Fig. 2.7.

Cluster Model

An important property of the parton branching process is the preconfinement of colour [14]. Preconfinement implies that the pairs of colour-connected neighbouring partons discussed above have an asymptotic mass distribution that falls rapidly at high masses and is asymptotically Q^2-independent and universal. This suggests a class of cluster hadronization models, in which gluons at the end of the perturbative phase are split into quark and antiquark pairs. Then, colour-singlet clusters of partons form which afterwards decay

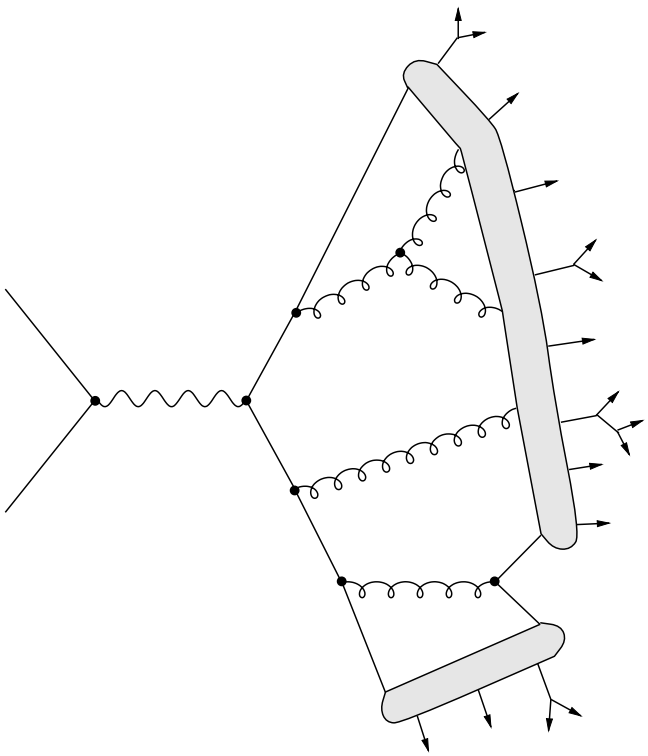

Figure 2.7: String fragmentation scheme.

isotropically into hadrons. Only these hadrons and/or the decay products of short-lived or weakly decaying ones are measurable in the detector. An schematic view of the cluster model is shown in Fig. 2.8.

2.5.3 Monte Carlo Programs: a brief description

Complete matrix elements (ME) calculations are expected to give a good description of multi-jet events when large separations among jets are involved and in particular when angular variables are considered. On the other hand, pure ME differential cross sections lack parton shower and hadronization and cannot reproduce collinear and soft radiation at arbitrarily high order. It is therefore important to have the possibility to start with pure ME calculations and complement them with these additional features. The results obtained in this way (ME + PS + hadronization) can be compared with pure parton level ones as well as those from dedicated QCD MCs, like standard $q\bar{q}$ PYTHIA and HERWIG.

If one takes for example topologies with four or more jets, one expects that a reasonable description for not too small values of the jet resolution y_{cut} may be obtained starting

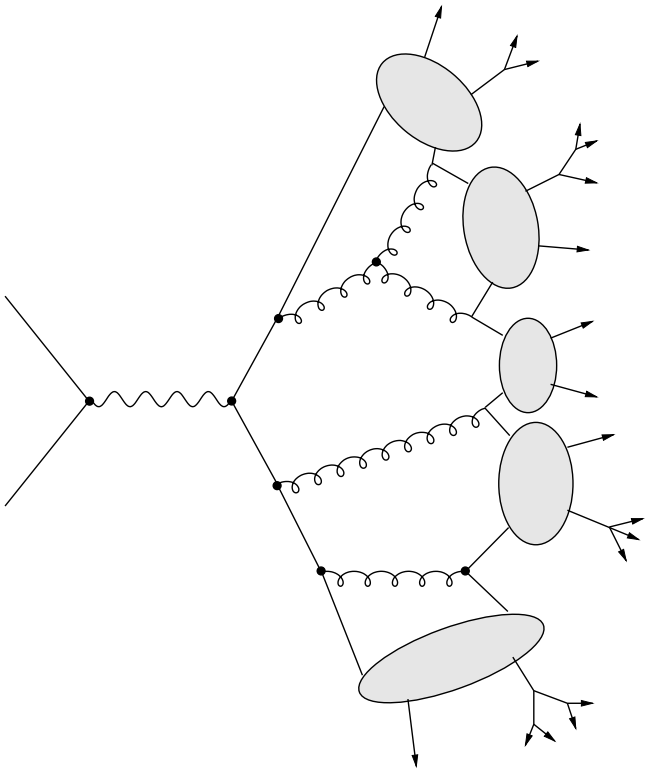

Figure 2.8: Cluster fragmentation scheme.

with a four-parton ME at a much lower y_{cut} and adding to it PS and hadronization. This jet resolution parameter, y_{cut}, introduced here is just a parameter of the different algorithms used to define jets at parton level in the theoretical calculations, and for grouping the selected neutral and charged tracks into jets at the experimental level. Even if events such as the one in Fig. 2.3 have been seen in a detector such as ALEPH, there is no unique way of grouping particles into jets and so different algorithms have been proposed. Basically, the method used is the successive binary clustering, i.e. for all pairs of final-state particles (i, j), a test variable y_{ij} is defined. The minimum of all y_{ij} is compared to the so-called jet resolution parameter. If it is smaller, the two particles are recombined into a new pseudo-particle with four-momentum $p_k = p_i + p_j$ (other recombination schemes have also been proposed).

One must however be aware of the fact that when starting with four-parton ME, all events described by two- or three-parton ME + PS + hadronization are not taken into account. In this respect QCD MCs surely give a more complete description as they start a PS from a two-parton ME and match three-parton production with the respective ME

results. The above mentioned approach of starting from four-parton ME can however be considered as a complementary approach for some studies and a way to check MC results when for instance angular variables or mass effects are involved.

In the following sections two options to start with four-parton configurations, using the PYTHIA showering and hadronization, are described. However, there are other options as the ones described in the HERWIG and APACIC subsections.

PYTHIA

A shower interface to four-partons massless matrix elements
Since version 6.1, the PYTHIA MC program contains an algorithm to start a shower from a given four-jet configuration, $q\bar{q}gg$ or $q\bar{q}q'\bar{q}'$. This allows comparisons of four-jet topologies between matrix-element calculations and data, with showering and hadronization effects better implemented, which are not covered by the matrix-element calculations alone.

The standard PYTHIA parton shower does not include any matching procedure to four-jet matrix elements. Therefore, it is not a good option for the description of four-jet topologies. For example, it does not correctly model angular azimuthal distributions in branchings. In fact, the standard shower routine is set up only to handle systems of two showering partons, not three or more.

The basic idea of matching to a four-parton configuration is to cast the output of matrix element generators in the form of a parton shower history, which then can be used as input for a complete parton shower. Here two of the subsequent branchings already have their kinematics defined, while the rest are chosen freely as in a normal shower. Benefits of having a prehistory include *(i)* the availability of the standard machinery to take into account recoils when masses are assigned to massless partons in the matrix elements, *(ii)* a knowledge of angular-ordering constraints on subsequent emissions and azimuthal anisotropies in them, and *(iii)* information on the colour flow as required for the subsequent string description. The choice among possible shower histories is based on a weight obtained from the mass poles and splitting kernels.

For example, let's concentrate on a process like $q\bar{q}gg$. Here the matrix-element expression contains contributions from five graphs (Fig. 2.9) and from interferences between them. The five graphs can also be read as five possible parton shower histories, but here

without the possibility of including interferences. The relative probability for each of these possible histories can be obtained from the rules of shower branchings.

The relative probability $\mathcal{P}$ for each of the five possible parton-shower histories can be used to select one of the possibilities at random. Then, when the conventional parton shower algorithm is executed, the properties such as masses, momentum transfers and angles between mother and daughter partons are forced to stay at the same value as for the ME configurations. However, this forcing cannot be exact since the final partons given by the ME are on the mass shell, while the corresponding partons in the parton shower might be virtual and branch further. All other branchings of the parton shower are selected at random according to the standard evolution scheme. Singular regions are typically avoided with a cut $y >$y$_{\rm int}$(default 0.01), where y is the square of the minimal scaled invariant mass between any pair of partons. All this is done by calling the PY4JET routine that will shower and fragment the four-parton configuration given as input. The partons have to be stored in the order $q\bar{q}gg$ or $q\bar{q}q'\bar{q}'$, where $q'\bar{q}'$ is assumed to be the secondary quark pair.

This strategy used in PYTHIA has the advantage that it can be applied to arbitrarily complicated partonic states, but the disadvantage that it does not tell how to mix different event topologies consistently. Therefore, it can be used for events where the main partons are well separated, and the task is to provide a realistic representation of the internal structure of the resulting jets, which is the case of a four-parton configuration at LEP1.

Interfacing four-parton massive matrix elements: FOURJPHACT
FOURJPHACT is a Fortran code that computes exact LO *massive* MEs for all $e^+e^- \to q\bar{q}q'\bar{q}'$ and $e^+e^- \to q\bar{q}gg$ final states and it interfaces them with the PYTHIA routine PY4JET.

The program starts by computing some cross section, where one can choose between fixed or running α_s. Unweighted events may be generated during this step, or in a second run in order to obtain a predetermined number of events. These may be passed to PYTHIA which provides PS and hadronization.

An inventory of cuts at parton level are already defined in FOURJPHACT: to implement them one only has to specify the numerical values for minima and maxima of

energies, transverse momenta, angles among partons and invariant masses. In a similar way, cuts using the resolution parameter of the most used clustering algorithms can be requested (e.g. a DURHAM y_{cut}, which is the clustering algorithm used for this thesis, as explained in Section 5.1).

FOURJPHACT can compute or generate events for one final state at a time or for all 20 final states with quarks (no top) and gluons at the same time. In this last case, the corresponding probability of each channel is determined or read from a file, and the generated events will have the correct fraction of all final states. This "one shot" option is often used when hadronization is required afterwards.

HERWIG

Four-jet matrix element + parton shower options (massless ME)
A new option available in HERWIG version 6.1 is to generate events starting from the four-parton processes $e^+e^- \to q\bar{q}gg$ and $e^+e^- \to q\bar{q}q'\bar{q}'$. The relevant process code is $IPROC = 600 + IQ$ for primary quark flavour IQ or 600 for a sum over all flavours. The matrix elements used are those of Ellis, Ross and Terrano [15] and Catani and Seymour [16], which include the relative orientation of initial and final states, but not quark masses. The kinematic effects of quark masses are taken into account in the subsequent parton showers and in matching the showers to the momentum configurations generated according to the matrix elements. The variable $EMSCA = \min \sqrt{s_{ij}}$, where $s_{ij} = 2p_i \cdot p_j$, sets a limit on the transverse momenta in the showers and is also used as the scale for α_s. The latter feature has the effect of enhancing the regions of small s_{ij} relative to matrix element calculations with α_s fixed.

To avoid soft and collinear divergences in the matrix elements, an internal parton resolution parameter $Y4JT$ must be set. The interparton distance is calculated using either the DURHAM or JADE metric. This choice is governed by the logical parameter $DURHAM$. For reliability of the results, one should use the same metric for parton and final-state jet resolution, with a value of $Y4JT$ smaller than the y_{cut} value to be used for jet resolution.

APACIC

The philosophy of the new approach of the APACIC MC [17] is to use ME and PS in the corresponding regimes of their reliability: matrix elements are employed to describe

the production of jets, and parton showers to model their evolution. A general algorithm to match them has been proposed and implemented in APACIC++, the PS part of the package. The algorithm is based on the paradigm above, namely to restrict the validity of the ME's for the description of particle emission to the regions of jet-production, i.e. to regions of comparably large angles and energies - or to large y_{cut} of the corresponding jet-clustering scheme. In contrast, the PS is restricted to the disjunct region of jet-evolution, i.e. small angles and low energies - or low y_{cut}, respectively. The hadronization of the partons is left to well-established schemes. At the moment, an interface to the hadronization in the Lund-string picture as implemented in PYTHIA is supplied.

The program package is designed for the modelling of multi-jet events. It is capable to produce and evaluate matrix elements for the production of up to five massive partons in QCD and at least all electroweak processes of the type $e^+e^- \to$ four fermions allowed in the Standard Model. The MEs are matched to the parton shower via an algorithm capable to deal with -in principle- any number of jets produced via the strong, weak or electromagnetic interaction on equal footing.

APACIC ++ parameters:

- *i)* $y_{cut}{}^{ini}$ Emissions of colour charged partons are restricted to resolution parameters $y_{cut} > y_{cut}{}^{ini}$.
- *ii)* $\kappa_s^{3,4,5}$ Due to the truncation of the perturbative expansion, matrix element calculations show a significant dependence on the QCD renormalization scale. APACIC++ accounts for these dependences by a scale parameter $\kappa_s^{3,4,5}$ for each n-jet configuration: $\alpha_s = \alpha_s(\kappa_s^{3,4,5} \cdot s)$, where s is the square of the center-of-mass energy of the e^+e^- system.
- *iii)* $\alpha_s(M_Z)$ The strong coupling constant is responsible for the parton shower evolution
- *iv)* cut-off PS The parton shower ends at a given energy scale, where fragmentation starts.

2.6 Extensions beyond QCD: The light gluino hypothesis

Si es que existen, he de encontrar
lenguajes de un mundo que está dormido entre las hojas de los libros.

Although experimental measurements at the highest available energy are consistent with the standard model of the strong interactions, the observed relationship of the strong coupling constant at the Z and the weak angle as well as the value of the b/τ mass ratio in relation to the top quark mass remain strong indications of a supersymmetric (SUSY) grand unification above 10^{16}GeV and a SUSY threshold for squarks and sleptons in the 0.1 to 1 TeV region. Supersymmetric phenomenology deals normally with sparticles of masses $\mathcal{O}(100)$GeV. The only exception is the light gluino with mass ≤ 1.5GeV and $3-5$GeV [19]. In this unification picture the value of the SUSY threshold is very sensitive to the highest known (two-loop) contribution to the Minimal Supersymmetric Standard Model(MSSM) β function. At the one-loop order a SUSY threshold far below 100GeV would be needed in order to fit the coupling constant measurements and such a low threshold is directly ruled out by the non-observation of squarks and sleptons in Z decay. This suggests that the three-loop results could also be important especially as the precision of the measurements at the Z and beyond improves.

As a first step in the calculation of the full three-loop β function of the MSSM, the gluino contribution to the renormalization of the strong coupling constant is taken into account. This gives the complete result in the region between the gluino mass and the squark mass which, in the light gluino scenario, extends from the low energy regime up to the Z and beyond up to the squark threshold. Then, as was seen in Section 2.3.3, the running of the strong coupling constant as a function of the scale μ is determined by the QCD β function, redefined here more conveniently as

$$\frac{d\alpha_s}{d(\ln \mu)} = -\alpha_s \beta \left(\frac{\alpha_s}{4\pi}\right) \tag{2.48}$$

where β has the perturbative expansion

$$\beta(x) = \beta_1 x + \beta_2 x^2 + \beta_3 x^3 + ... \tag{2.49}$$

Simple relations between the coefficients, e.g. $\beta_1 = b\,8\pi$, allow to go from the definition in Eq. 2.14 to the one in Eq. 2.49. Ignoring squark contributions, the one- and two-loop results in the minimally extended SUSY QCD are [20]

$$\beta_1 = \frac{22}{3} C_A - \frac{8}{3}\left(N_f T_R + \frac{N_g}{2} C_A\right) \tag{2.50}$$

$$\beta_2 = \frac{68}{3}C_A^2 - \frac{40}{3}\left(N_f T_R C_A + \frac{N_g}{2}C_A^2\right) - 8\left(N_f T_R C_F + \frac{N_g}{2}C_A^2\right) \tag{2.51}$$

where N_g is the number of gluino multiplets.

The gluino contributions to the β function coefficients as well as the additional four-jet final states can be exploited to set limits on the light gluino mass. In fact this was used in a previous ALEPH analysis [21] to exclude the existence of a gluino with mass below 6.3 GeV/c^2. In this analysis four-jet observables were used, for which only tree-level cross sections were known at that time. Similar hints were found in the analysis by Csikor and Fodor [22], based on the running of the strong coupling constant.

However, a consistent analysis looking for a hint of the existence of the light gluino, must contain the virtual gluino effects not only in the running (technically in the β function), but in all loop diagrams. As will be seen in Chapter 5, since recently calculations up to next-to-leading order exist, which will allow for a consistent analysis. The calculations are for massless quarks and a massless gluino though, preventing to set a limit on the light gluino mass.

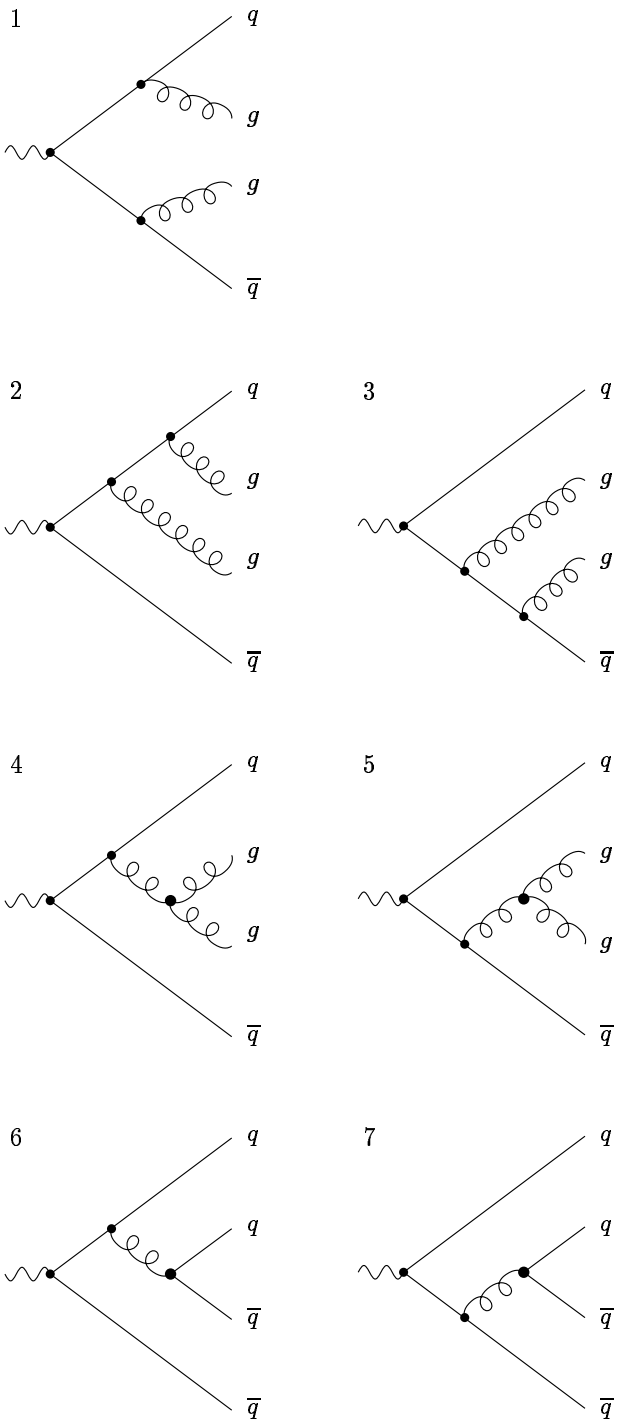

Figure 2.9: Four parton configurations.

Chapter 3

QCD predictions for Four-Jet Observables

Prometo cambiar, volverme humilde como un cristiano,
dejar de beber y aprender tu alfabeto.

3.1 Introduction

Multi-jet events at LEP have sufficiently large invariant masses to ensure that jets truly reflect the distribution of quark and gluon quanta in the femto-universe, revealing the basic couplings in the QCD Lagrangian. Four-jet events are particularly interesting for the study of QCD (see Fig. 3.1), since this theory shows its full gauge structure only in order α_s^2. They are extremely important to experimentally verify the effects of the gluon self-coupling, since the $e^+e^- \to q\bar{q}gg$ cross section dominates over the $e^+e^- \to q\bar{q}q\bar{q}$. As already seen in Chapter 2, the direct coupling between gluons is a consequence of the non-abelian nature of QCD.

The three-jet cross section is consistent with a spin-one gluon. However, one could imagine an alternative "Abelian QCD" theory, in which $SU(3)$ is replaced by $[U(1)]_3$ and the coupling is adjusted to be $\tilde{\alpha}_s = C_F\alpha_s$, so that the correct three-jet rate is obtained. It is then the four-jet rate that allows to distinguish this theory from QCD, since only a subset of the QCD Feynman diagrams contribute in the Abelian case.

The QCD cross section for four-parton production is given by

$$d\sigma^{(4)} = \left(\frac{\alpha_s}{2\pi}\right)^2 [C_F^2\mathcal{A} + C_F C_A\mathcal{B} + C_F T_R n_f\mathcal{C}] + \mathcal{O}(\alpha_s^3)\,, \tag{3.1}$$

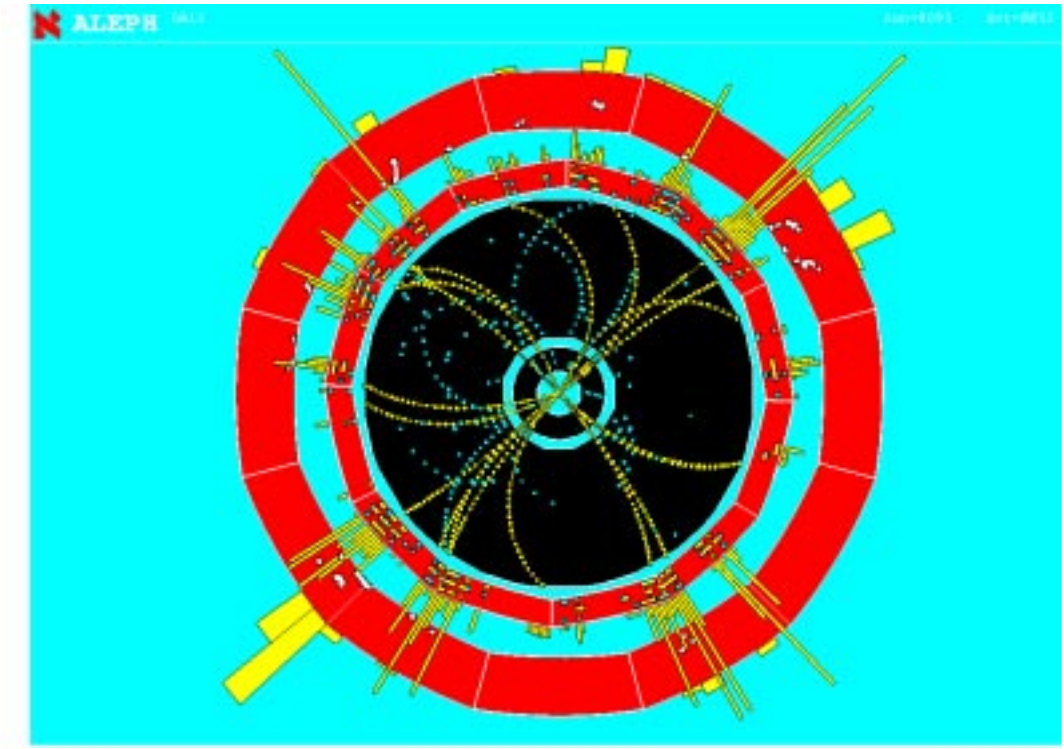

Figure 3.1: A four-jet hadronic event recorded with the ALEPH detector.

where $\mathcal{A}$, $\mathcal{B}$ and $\mathcal{C}$ are functions of the parton-parton invariant masses squared, $s_{ij} = (p_i + p_j)^2$. The last term on the right-hand side corresponds to the $q\bar{q}q\bar{q}$ final state, and is common to both the Abelian and non-Abelian theories. The first two terms correspond to the $q\bar{q}gg$ final state: the second term receives contributions from the triple-gluon vertex diagram and is absent in the Abelian theory.

With the overall couplings already fixed by the three-jet rate, the four-jet rates are therefore different in the two theories, and one could in principle discriminate between them on the basis of the overall event rate alone. In particular, the rate is much smaller for the Abelian theory, where the $q\bar{q}q\bar{q}$ final state rate is relatively more important than in QCD. The problem with this is that the magnitude of the cross section is quite sensitive to the choice of scale in the strong coupling, and this freedom would allow the overall rates to be adjusted to fit the measured rate in each case. In principle, the fraction of four-quark events would also provide a discrimination. However, it is very difficult to distinguish light-quark and gluon jets with the necessary efficiency. The only realistic possibility appears to be to tag at least three b quarks in the final state (using vertex de-

tectors or semi-leptonic decays) to estimate the fraction of $q\bar{q}q\bar{q}$ events, but the efficiency is again very low.

A much more powerful and illuminating method makes use of the different correlations among the final-state particles induced by the various contributions to the cross section. These correlations have their origin in the different angular momentum properties of the final state.

In this study both the overall four-jet rate and the so called four-jet angular correlations have been used. The four-jet rate is very sensitive to the strong coupling constant and, as the resummation of large logarithms exist, we expect its scale dependence to be heavily reduced. For the angular correlations, the sensitivity to the QCD colour factors will be exploited. In the following pages the description of these observables can be found.

3.2 Four-Jet Observables

The NLO differential cross section for a four-jet observable, O_4, can be written as,

$$\frac{1}{\sigma_0}\frac{d\sigma}{dO_4}(O_4) = \eta(\mu)^2 B_{O_4}(O_4) + \eta(\mu)^3 \left[B_{O_4}(O_4)\beta_0 \ln {x_\mu}^2 + C_{O_4}(O_4)\right] \tag{3.2}$$

with

$$\eta(\mu) = \left(\frac{\alpha_s(\mu) C_F}{2\pi}\right) \tag{3.3}$$

and where σ_0 is the Born cross section for e^+e^- annihilation into hadrons, μ is the renormalization scale, x_μ the ratio of μ with respect to the Z boson mass, and B_{O_4} and C_{O_4} are scale-independent functions. They are obtained from the integration of the fully differential massless matrix elements for e^+e^- annihilation into four-parton final states. The NLO expression is presented here, as terms at $\mathcal{O}(\alpha_s^4)$ have not yet been calculated.

For the running coupling the two-loop expression

$$\eta(\mu) = \frac{\eta(\mathrm{M_Z})}{w(\mu)}\left(1 - \frac{\beta_1'}{\beta_0'}\eta(\mathrm{M_Z})\frac{\ln w(\mu)}{w(\mu)}\right) \tag{3.4}$$

is used, with

$$w(\mu) = 1 - \beta_0' \eta(\mathrm{M_Z}) \ln\left(\frac{\mathrm{M_Z}}{\mu}\right) \quad , \tag{3.5}$$

$$\beta_0' = \frac{11}{3}x - \frac{4}{3}yN_f \quad , \quad \beta_1' = \frac{17}{3}x^2 - 2\,y\,N_f - \frac{10}{3}x\,y\,N_f \quad . \tag{3.6}$$

$x = \frac{C_A}{C_F}$ and $y = \frac{T_R}{C_F}$ are the QCD colour factor ratios. Using the expected values from $SU(3)$ for the colour factors, $C_A = 3$ and $C_F = 4/3$, together with the normalization $T_R = 1/2$, the theoretical prediction for the ratios is x=2.25 and y=0.375. β_0' and β_1' are the coefficients of the QCD β function as defined in Section 2.6 but including some factors, $\beta_0' = \beta_0/2C_F$ and $\beta_1' = \beta_1/4C_F^2$, to have as perturbative parameter $\eta(\mu)$ instead of $\alpha_s(\mu)$, and setting N_g to zero, as the light gluino hypothesis is not taken into account for the time being.

The B and C functions depend linearly and quadratically on the colour factors, as can be seen in the following expressions,

$$B_4 = B_0 + B_x\,x + B_y\,y \tag{3.7}$$

and

$$C_4 = C_0 + C_x\,x + C_y\,y + C_z\,z + C_{xx}\,x^2 + C_{xy}\,x\,y + C_{yy}\,y^2\,. \tag{3.8}$$

Such a dependence will be used, in the analyses presented in Chapter 6, for the simultaneous measurement of the strong coupling constant and the colour factors. At NLO the ratio z appears that is related to the square of a cubic Casimir operator,

$$C_3 = \sum_{a,b,c=1}^{N_A} \mathrm{Tr}\left(T^a T^b T^{\dagger c}\right) \mathrm{Tr}\left(T^{\dagger c} T^b T^a\right) \quad , \tag{3.9}$$

via $z = \frac{C_3}{N_c\,C_F^3}$.

3.2.1 Electron-Positron Annihilation Cross Section

In the previous chapter it was seen that the formation of hadrons is non-perturbative. However, a pQCD calculation of the total hadronic cross section can be obtained. The reason for this can be found when looking at the event in space-time. The electron and positron collide to form a γ or a Z of virtuality Q equal to the collision energy $\sqrt{s}$, which fluctuates into $q\bar{q}$, $q\bar{q}g$, ... By the uncertainty principle, this fluctuation occurs on a distance scale of the order $1/Q$, and if Q is large the production rate should be predicted by perturbation theory. Subsequently, the quarks and gluons form themselves into hadrons. This process, called hadronization, occurs at a much later time scale characterized by $1/\Lambda$, where Λ is the scale in α_s, i.e. the scale at which the coupling becomes strong. The interactions which change quarks and gluons into hadrons certainly modify the outgoing state, but they occur too late to modify the original probability for the event to happen,

which can therefore be calculated in perturbation theory.

The total cross section for $q\bar{q}$ production at Born level (no initial state radiation, no gluon radiation) is given by

$$\sigma_0 = \frac{12\pi\Gamma_{ee}\Gamma_{q\bar{q}}}{\mathrm{M_Z^2}\Gamma_\mathrm{Z}^2} \tag{3.10}$$

where $\mathrm{M_Z}$ is the mass of the Z boson, and Γ_{ee}, $\Gamma_{q\bar{q}}$ and Γ_Z are the partial widths for Z decay into e^+e^-, $q\bar{q}$ and the total width, respectively. Leading-order corrections, see Fig. 3.2, from pQCD to this Born cross section give

$$\sigma_\mathrm{tot} = \sigma_0 \left(1 + \frac{\alpha_s}{\pi}\right) = \sigma_0 \left(1 + \frac{3}{2}\eta\right) \tag{3.11}$$

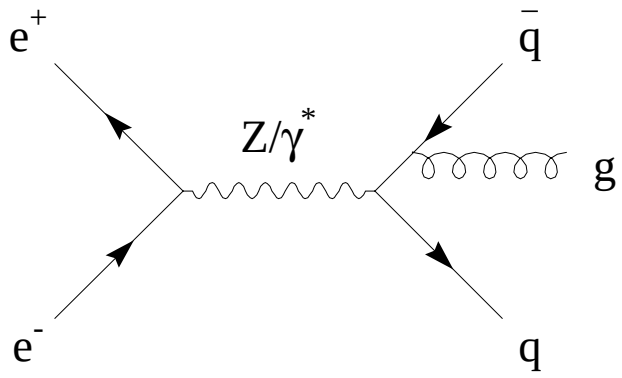

Figure 3.2: Feynman graph for the $\mathcal{O}(\alpha_s)$ correction to the Born cross section for $e^+e^- \to q\bar{q}$.

3.3 The Four-Jet Rate

The four-jet rate is used in this thesis as it is very sensitive to η (i.e. to the strong coupling constant). Following the expression in Eq. 3.2, the NLO prediction for the four-jet rate -defined as the ratio of the four-jet cross section to the total hadronic cross section- is given by:

$$\begin{aligned} R_4(\mathrm{y_{cut}}) = \frac{\sigma_{4-\mathrm{jet}}}{\sigma_\mathrm{tot}}(\mathrm{y_{cut}}) &= \eta(\mu)^2 B_4(\mathrm{y_{cut}}) \\ &+ \eta(\mu)^3 \left[\beta_0 \ln(x_\mu^2) + C_4(\mathrm{y_{cut}}) - \frac{3}{2}B_4(\mathrm{y_{cut}})\right], \end{aligned} \tag{3.12}$$

where y_{cut} is the clustering resolution parameter and the relation in Eq. 3.11 is used to obtain the proper normalization.

Four-jet fractions decrease very rapidly when increasing the resolution parameter, so most of the data is found at small y_{cut}. However, the fixed order perturbative prediction is not reliable for small values of y_{cut}, due to the terms $\alpha_s{}^n \ln^m y_{cut}$ that enhance the higher order corrections. The all-order resummation of the leading and next-to-leading logarithmic (NLL) contributions has to be performed. This resummation is possible with the Durham clustering algorithm [23] used in this thesis and described in Section 5.1, using the coherent branching formalism. The expression for the four-jet rate in the next-to-leading logarithmic approximation is given in [24],

$$R_4^{\mathrm{NLL}} = 2[\Delta_q(Q)]^2 \left[\left(\int_{Q_0}^{Q} dq \Gamma_q(Q,q) \Delta_g(q,Q_0) \right)^2 + \int_{Q_0}^{Q} dq \Gamma_q(Q,q) \Delta_g(q,Q_0) \times \int_{Q_0}^{q} dq' + \left(\Gamma_g(q,q') \Delta_g(q',Q_0) + \Gamma_f(q') \Delta_f(q',Q_0) \right) \right] . \tag{3.13}$$

The functions $\Delta_a(Q,Q_0)$ are the Sudakov form factors which express the probability of parton branching evolution from a scale $Q = Q_0\sqrt{y_{cut}}$ to a scale Q_0 without resolvable branching. These functions are obtained as the integrals of the emission probabilities $\Gamma_a(Q,q)$, which are:

$$\begin{aligned} \Gamma_q(Q,q) &= \frac{2C_F}{\pi} \frac{\alpha_s(q)}{q} \left[\left(1 + \frac{\alpha_s(q)}{2\pi} K \right) \ln \frac{Q}{q} - \frac{3}{4} \right] \quad , \\ \Gamma_g(Q,q) &= \frac{2C_A}{\pi} \frac{\alpha_s(q)}{q} \left[\left(1 + \frac{\alpha_s(q)}{2\pi} K \right) \ln \frac{Q}{q} - \frac{11}{12} \right] \quad , \\ \Gamma_f(Q,q) &= \frac{N_f}{3\pi} \frac{\alpha_s(q)}{q} \quad . \end{aligned} \tag{3.14}$$

The K coefficient is renormalization scheme dependent. In the $\overline{\mathrm{MS}}$ scheme it is given by [25]

$$K = C_A \left(\frac{67}{18} - \frac{\pi^2}{6} \right) - \frac{10}{9} T_R N_f \quad . \tag{3.15}$$

It was shown in reference [26] that one can obtain an improved theoretical prediction for the differential two-jet rate if the vertex probabilities are taken at next-to-leading

order, which we also consider in our analysis. Then the vertex probabilities can be written as,

$$\begin{aligned} P_{qq}(\alpha_s, z) &= C_F \left(\frac{1+z^2}{1-z} + \frac{\alpha_s}{2\pi} K \frac{2}{1-z} \right), \\ P_{gg}(\alpha_s, z) &= 2C_A \left(\frac{z}{1-z} + \frac{1-z}{z} + z(1-z) + \frac{\alpha_s}{2\pi} K \frac{2}{1-z} \right), \\ P_{gq}(\alpha_s, z) &= T_R N_f \left(z^2 + (1-z)^2 \right). \end{aligned} \tag{3.16}$$

As the Durham four-jet rate can be resummed but it does not satisfy a simple exponentiation, the only viable matching schemes are the R matching or the modified R matching [27, 28]. The one used in this study is the R matching following again reference [24]. The R-matched expression for the four-jet rate is

$$R_4^{\mathrm{R-match}} = R_4^{\mathrm{NLL}} + \left[\eta^2 \left(B_4 - B_4^{\mathrm{NLL}} \right) + \eta^3 \left(C_4 - C_4^{\mathrm{NLL}} - \frac{3}{2} \left(B_4 - B_4^{\mathrm{NLL}} \right) \right) \right] \quad . \tag{3.17}$$

In Fig. 3.3 a comparison of the predictions at different orders for the four-jet rate is shown. There we can notice that the NLO contribution is large, going from 30% to about 70% of the LO one. When the resummation is included the main difference is in the shape of the distribution. The same effect is found when the K coefficient is taken into account. As will be shown in Chapter 6, the inclusion of the K factor is needed in order to obtain a good fit of the data.

3.4 The Four-Jet Angular Correlations

Apart from the four-jet rate, four other observables have been used which are expected to be very sensitive to the colour factor ratios. These are the four-jet angular correlations:

- the Bengtsson-Zerwas angle [29]:

$$| \cos(\chi_{\mathrm{BZ}}) | = | \cos(\angle [(\vec{p}_1 \times \vec{p}_2), (\vec{p}_3 \times \vec{p}_4)]) | \tag{3.18}$$

- the Körner-Schierholtz-Willrodt angle [30]:

$$\cos(\Phi_{\mathrm{KSW}}) = \cos\left(\frac{1}{2} \left(\angle [(\vec{p}_1 \times \vec{p}_4), (\vec{p}_2 \times \vec{p}_3)] + \angle [(\vec{p}_1 \times \vec{p}_3), (\vec{p}_2 \times \vec{p}_4)] \right) \right) \tag{3.19}$$

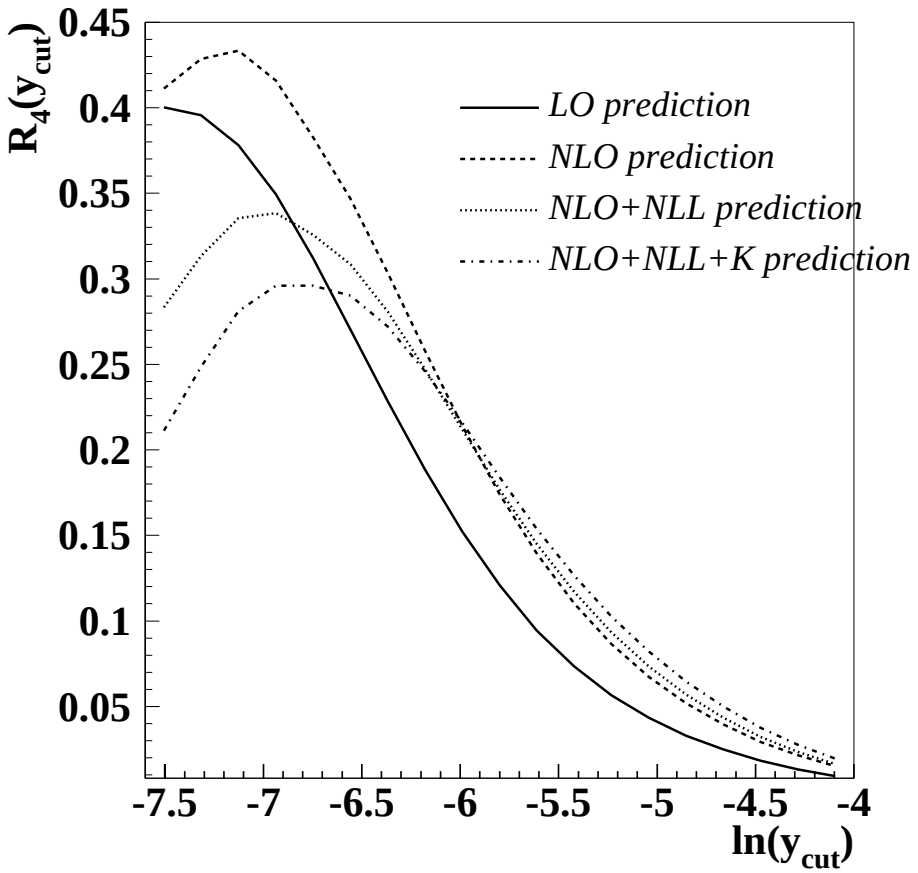

Figure 3.3: Predictions at different orders for the four-jet rate.

- the modified Nachtmann-Reiter angle [31]:

$$| \cos(\Theta_{\rm NR}) | = | \cos(\angle[(\vec{p}_1 - \vec{p}_2), (\vec{p}_3 - \vec{p}_4)]) | \tag{3.20}$$

- the angle between the two lowest energy jets [32]:

$$\cos(\alpha_{34}) = \cos(\angle[\vec{p}_3, \vec{p}_4]) \tag{3.21}$$

where p_i are the energy-ordered four-momenta ($E_1 > E_2 > E_3 > E_4$). The theoretical NLO expression for each of the angular observables will be of the form

$$\frac{1}{\sigma_0}\frac{d\sigma}{d\cos X}(\cos X) = \eta(\mu)^2 B_{\cos X}(\cos X) + \eta(\mu)^3 \left[B_{\cos X}(\cos X)\,\beta_0\,\ln({x_\mu}^2) + C_{\cos X}(\cos X)\right] \tag{3.22}$$

The idea of the four-jet angular observables is to exploit the characteristic features of gluon dynamics in QCD, as opposed to abelian theories, to isolate the triple gluon vertex

in four-jet events of e^+e^- annihilation. For this, the angular correlation observables were defined to be sensitive to different types of Feynman graphs as detailed in the following paragraphs.

- Gluons radiated from q and $\bar{q}$ in $e^+e^- \to q\bar{q}g$ are linearly polarized to a high degree in the $q\bar{q}g$ final state. If χ is the angle between the final state plane and the polarization vector then we have the probability for $g \to gg \approx \left[1 + \frac{1}{9}\cos 2\chi\right]$ and for $g \to qq \approx [1 - \cos 2\chi]$. Therefore we expect the angle between the plane formed by the two lowest energetic jets (preferentially virtual gluon decays) and the plane formed by the high energy jets (mostly the primordial $q\bar{q}$) to be distributed nearly isotropically in QCD while these planes should be preferentially perpendicular in abelian theories. Even if it is very difficult to distinguish between jets induced by the primary and the secondary partons, we expect the secondary partons to be less energetic. All this takes us to the definition of the Bengtsson-Zerwas angle. See Fig. 3.4 for the difference between QCD, which has $SU(3)$ as underlying gauge group, and an abelian theory.

- In order to obtain evidence for the triple-gluon vertex the following variable was presented. $\phi_{\mathrm{KSW}} = \angle[(\mathbf{p}_1 \times \mathbf{p}_4), (\mathbf{p}_2 \times \mathbf{p}_3)]$. In theories without the triple-gluon vertex the planes orthogonal to the vectors $\mathbf{p}_1 \times \mathbf{p}_4$ and $\mathbf{p}_2 \times \mathbf{p}_3$ are uncorrelated, and because of phase space restrictions the angle Φ_{KSW} between these two planes is found around 90°, preferentially. However, if there is a triple-gluon vertex, then the pole structure of the propagator for the intermediate gluon leads to a preference for small angles between the two secondary gluons, and a correlation between the planes is induced. Because of the energy ordering, the planes turn out to be anti-parallel most of the time. The final definition found in Eq. 3.19 comes from a generalization in order to be invariant under exchange of the first and second jet, as well as of the third and fourth jet. A simplified version of the Körner-Schierholz-Willrodt angle is obtained by looking at the angle between the two lowest energetic jets. This is the definition of the fourth angular observable defined above. The angle α_{34} distinguishes between the relative contributions from double gluon radiation and gluon splitting into gluon pairs. Gluon radiation from the two primary quarks occurs more or less independently, and because of the collinear character of bremsstrahlung and the energy ordering of the four jets, large angles between the secondary partons are expected. Gluon splitting into secondary partons on the other hand will lead to rather small opening angles. In Fig. 3.5 the distributions for the same cases as in the above figure are shown for comparison.

- To find a signal for the triple gluon vertex the following kind of events are considered:

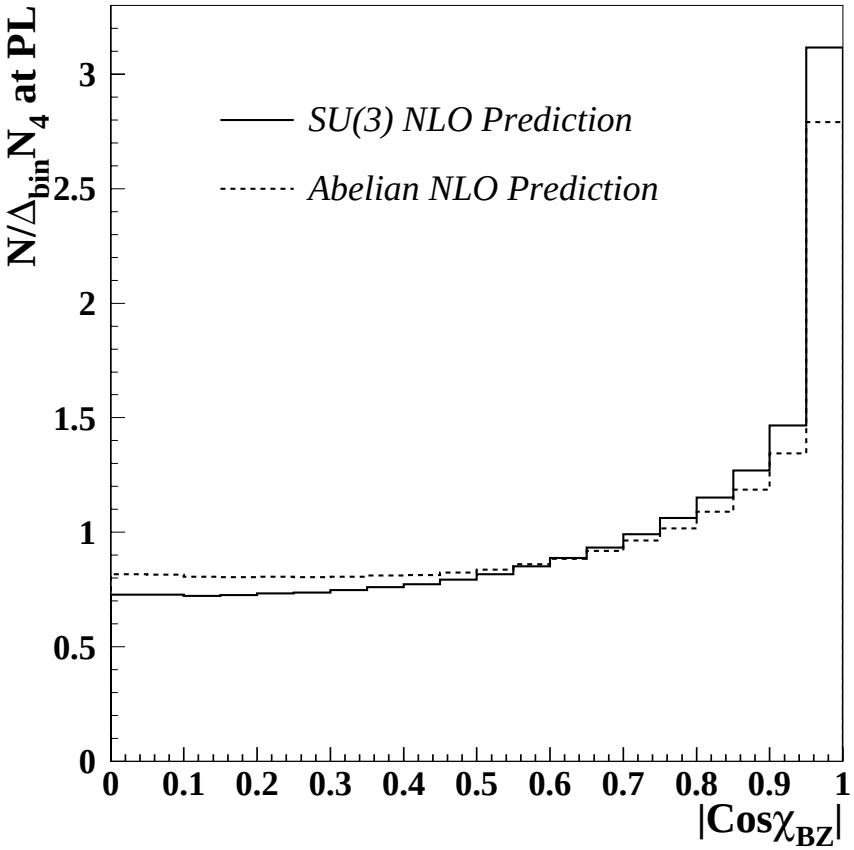

Figure 3.4: Comparison of QCD NLO predictions and abelian NLO predictions for the Bengtsson-Zerwas angle. (Durham algorithm, E-scheme, y_{cut}=0.008. See Section 5.1)

Two back-to-back jets of high energy and two back-to-back jets of much lower energy, i.e.

$$\begin{array}{ccc} \mathbf{p}_1 + \mathbf{p}_2 = 0 & & \mathbf{p}_3 + \mathbf{p}_4 = 0 \\ E_1 = E_2 & \gg & E_3 = E_4 \end{array}$$

Then $\cos\theta_{13} = (\mathbf{p}_1 \cdot \mathbf{p}_3)/|\mathbf{p}_1||\mathbf{p}_3|$, which is the angle between the axis of the high energy jets and the low energy jets is very sensitive to the presence of the triple-gluon coupling. If we concentrate on events where a virtual gluon decays either into two spin-1/2 or into two massless vector particles, the virtual gluon will have always helicity 0 with respect to the direction of the high energy jets. Therefore the helicities of the high energy quark-antiquark pair must be opposite and the pair $q\bar{q}$

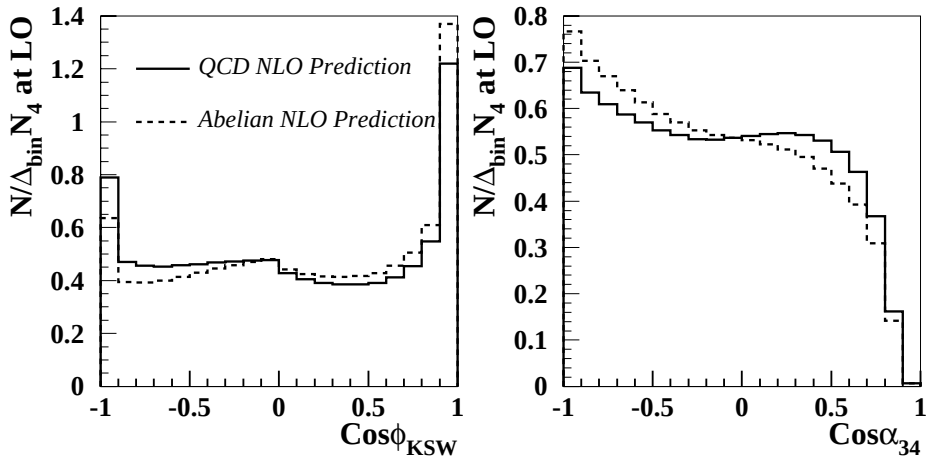

Figure 3.5: Comparison of QCD NLO predictions and abelian NLO predictions for $\cos\Phi_{\mathrm{KSW}}$ and $\cos\alpha_{34}$ (Durham algorithm, E-scheme, y_{cut}=0.008. See Section 5.1)

carries ± 1 unit of angular momentum with respect to its direction of flight. Note that a vector particle like a gluon with helicity zero in one direction has only helicity components ± 1 in any orthogonal direction. Now, if the virtual gluon decays to a massless $q\bar{q}$ pair, then the direction of these secondary partons has to be orthogonal to the primary ones. However, for a decay into two real gluons, which must have helicity ± 1, the situation is just the inverse. In summary, the following distributions are expected for different kinds of graphs:

$$\frac{d\sigma}{d\cos\theta_{13}} \propto 1 - \cos^2\theta_{13} \quad \text{for the final state } q\bar{q}q\bar{q} \tag{3.23}$$

$$\frac{d\sigma}{d\cos\theta_{13}} \propto \cos^2\theta_{13} \quad \text{for the final state } q\bar{q}gg \tag{3.24}$$

Since in QCD there are more gluon decays into two gluons than into a quark-antiquark pair, a dominance of the $\cos^2\theta_{13}$ term is expected. Of course, in reality also double bremsstrahlung diagrams occur, and $\cos\theta_{13}$ has to be restricted to values well below 1 where the perturbation theory breaks down due to collinear divergences. To solve this problem, a generalized Nachtmann-Reiter angle was proposed, Eq. 3.20, which is the one used in this thesis. Fig. 3.6 shows the comparison between a four-quark channel and a two-quark-two-gluon one.

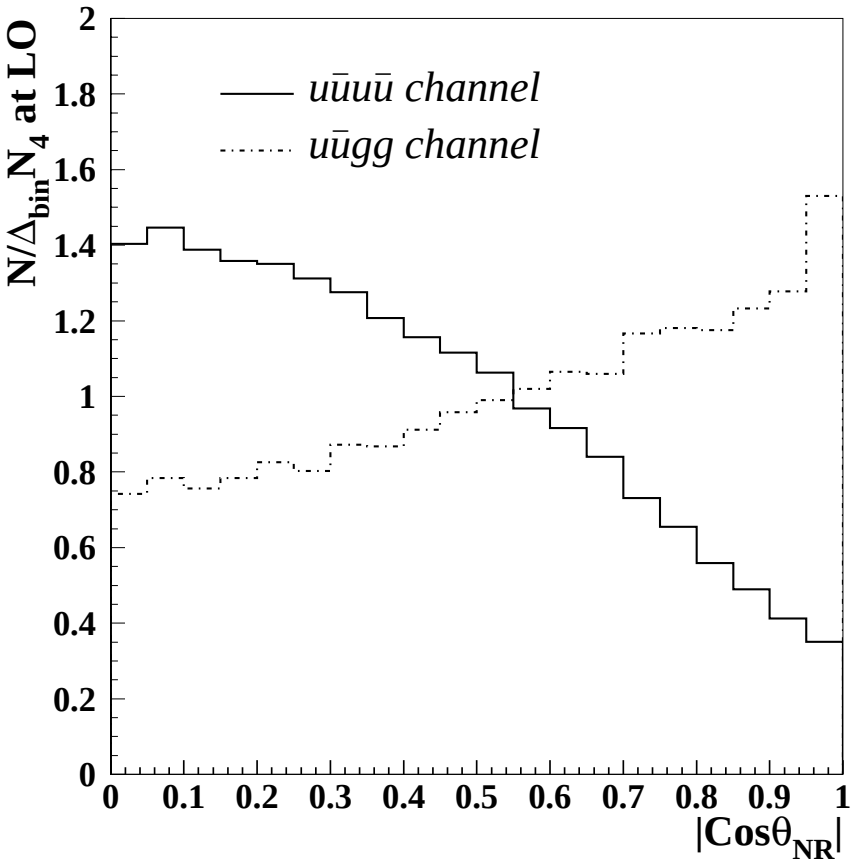

Figure 3.6: Comparison of the $|\cos\theta_{\mathrm{NR}}|$ distributions at LO between a four-quark channel and a two-quark-two-gluon channel.

3.5 Four-Jet Events and Monte Carlo implementation

The analyses of this thesis will be based on the observables described above. Thus, it is very important that four-jet events from QCD are correctly implemented in the MC programs that are widely used in phenomenological studies of hadron production at e^+e^- colliders. However, certain aspects of the four-jet production are known not to be well described by the standard "$\mathcal{O}(\alpha_s)$ ME + parton shower" MC programs. In addition, some of the observables that have shown a significant disagreement between data and MCs are the four-jet angular correlations, which will be used for the simultaneous measurement of the strong coupling constant and the colour factors.

Such discrepancies have been related to the fact that standard MCs do not provide a correct description of the spin correlations among the various partons, particularly at large jet separations. These correlations are naturally included in a full matrix element calculation, but are not necessarily included in a PS emulation for the four-jet final state. A consequence of this is that "$\mathcal{O}(\alpha_s^2)$ ME" programs, such as the option of four-parton + string fragmentation (no parton shower) implemented in PYTHIA, yielded a much better angular description of four-jet final states. However, even an "$\mathcal{O}(\alpha_s^2)$ ME + fragmentation" model, without the PS evolution, is inadequate to describe QCD four-jet production in e^+e^- collisions. The problem is that such ME models contain "ad-hoc" hadronization which is adjusted to produce a good agreement with some data, but they cannot be extrapolated to other energies. Furthermore, their description of the sub-jet structure is very poor.

Such deficiencies in the description of four-jet final states could be cured by an "$\mathcal{O}(\alpha_s^2)$ ME + PS" (plus hadronization) approach, that is now available in the commonly used MC programs, PYTHIA and HERWIG (see Section 2.5.3 for more details). There, a combination of the full angular information content of matrix elements with the detailed sub-jet structure of parton showers is tried, which should give a realistic overall description of event properties.

Chapter 4

Description of the experiment

The measurements presented in this thesis were obtained using data taken by ALEPH at the Z peak during the years 1994-95. ALEPH was one of the four detectors[1] at the LEP accelerator (Large Electron Positron collider). In this chapter both LEP and the ALEPH detector are briefly described. For the latter, the performances relevant for the analyses are emphasized.

4.1 The LEP collider

The LEP collider [33, 34] was an e^+e^- storage ring with a 27 km circumference situated at the European Laboratory for Particle Physics (CERN) in Geneva, Switzerland. It was located in an underground tunnel (depth 80-137 m) spanning the French and Swiss territories, see Fig. 4.1. It was built to make precision studies of the Standard Model and to look for hints of new physics, and it was in operation from August 1989 till November 2000.

The beams were formed by bunches of electrons and positrons accelerated in opposite directions. They were steered to collide only in the 4 points where the detectors were placed.

The LEP injection chain started with a linear accelerator (LINAC) which accelerated electrons and positrons in two stages. In the first stage, the electrons were accelerated up to an energy of 200 MeV. Then, part of these electrons were used to produce positrons by collision with a tungsten target. In the second stage, both electrons and positrons were accelerated up to an energy of 600 MeV. The particles were then injected into a small

[1] the other three are DELPHI, L3 and OPAL

storage ring (the Electron Positron Accumulator, EPA) where they were separated into bunches and accumulated until the beam intensities achieved nominal values. Afterwards, the leptons were first injected into the Proton Synchrotron (PS) and then into the Super Proton Synchrotron (SPS) storage ring, where they were accelerated up to an energy of 20 GeV. Finally, the particles were injected into the LEP main ring and accelerated until they reached the collision energy.

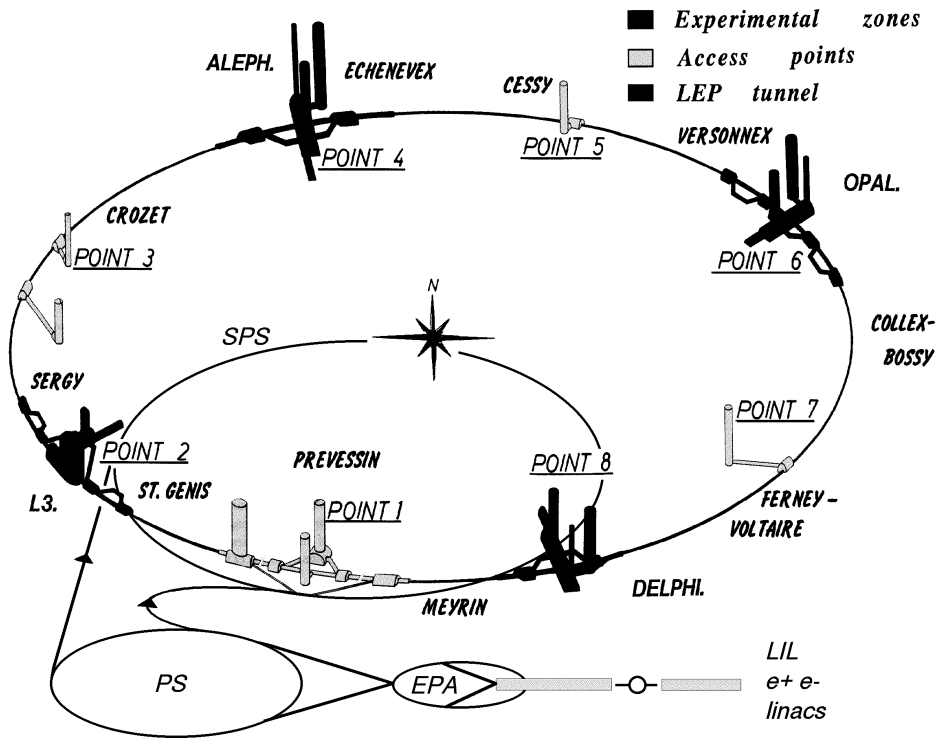

Figure 4.1: Schematic view of the LEP collider, the injector chain and the four interaction points.

During the first phase, LEP1 (1989-1995), LEP was operated at the peak position of the Z resonance and each experiment collected around four million visible Z decays. During the second phase, LEP2 (1995-2000), the energy was increased first to the threshold for W-pair production and later to the limit of the machine, which was found to be almost 210 GeV. Studies of the bosonic sector of the SM and searches for new physics have been the main goal of this last phase.

4.2 The ALEPH detector

The ALEPH (A detector for LEp PHysics) detector was a multi-purpose detector designed to cover as much of the 4π solid angle as possible. It consisted of a series of subdetectors arranged in an onion-like structure, see Fig. 4.2. A large tracking system immersed in a 1.5 T magnetic field allowed to reconstruct the direction and momentum of charged particles with very good resolution. The electromagnetic and hadronic calorimeters measured the energy of charged and neutral particles. The high segmentation of the first, together with the ionization measurement in the tracking system, was used for electron identification. Muons were identified using the muon chambers and the final planes of the hadron calorimeter, which provided continuous tracking inside sufficient iron absorber to eliminate the hadrons. The trigger system had the purpose of identifying interesting events while keeping the background rate low. Finally, the data acquisition system (DAQ) put together all the information coming from the subdetectors and built events which were then stored for further analysis.

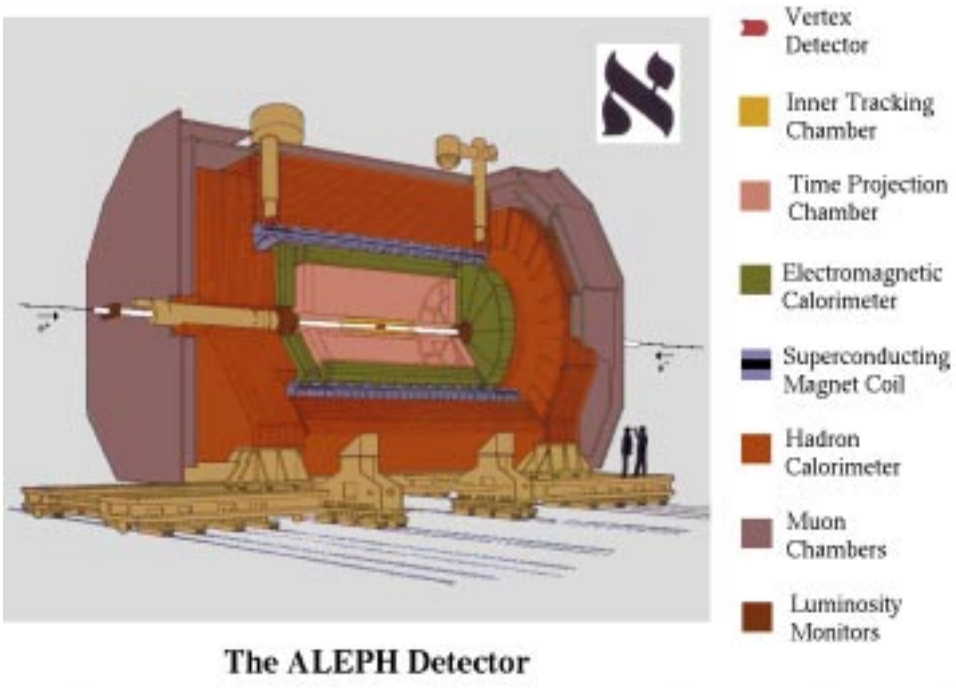

Figure 4.2: The ALEPH detector.

4.2.1 Subdetectors

In this section only the components relevant for this analysis are briefly described. We refer to [35] for further details.

- **Silicon Vertex detector (VDET):** The VDET was a double-sided silicon strip detector with two layers of strips parallel and perpendicular to the beam direction giving information on the azimuthal angle ϕ and the z coordinate, respectively. These were arranged in two coaxial cylinders around the beam pipe with inner and outer average radii of 6.5 and 11.3 cm. The angular acceptance was $|\cos\theta| \leq 0.95$ for tracks required to pass through at least one VDET layer.

  The trajectory of a track was determined starting with the outer tracking. VDET hits were used to improve the precision of the track parameters. They were reconstructed by averaging the charged-weighted positions of adjacent strips that have at least three times the mean noise charge. This way resolutions of $\sigma_\phi = 12$ μm in the ϕ and $\sigma_z = 10$ μm in the z direction were achieved. VDET also played a very important role in the identification of long-lived particles by tagging the displaced vertices of their decay products.

- **Inner Tracking Chamber (ITC):** It was a cylindrical multi-wire drift chamber. It provided up to eight accurate $r\phi$ points for tracking in the radial region between 16 and 26 cm. Charged particles traversing the chamber ionized the gas, which was a mixture of 80% Ar and 20% CO_2. The produced electrons drifted to the sense wires (mean drift velocity of 50 μm/ns), where they induced a signal via ionization avalanches. The ϕ coordinate was calculated from the relation between drift time and drift distance to the wire, whereas the z coordinate of a wire hit was found by using the difference of arrival times of the pulses at the two ends of the wire. The average accuracies were 150 μm and 3 cm, respectively.

- **Time Projection Chamber (TPC):** The central tracking device was a very large three-dimensional imaging drift chamber. It consisted of a cylindrical volume filled with a gas mixture of 91% Ar and 9% CH_4, and it operated with a gas pressure slightly above the atmospheric pressure. The electric drift field extended from each end plate towards the central membrane that divided the chamber into two halves. When a charged particle traversed the chamber, the electrons produced by ionization drifted towards one end plate, where their arrival position and time were measured by multi-wire proportional chambers. From the drift time and drift velocity the z coordinate could be deduced with a precision of 1 mm. The ϕ coordinate was calculated by interpolating the signals induced on cathode pads located behind

the sense wires, the r coordinate instead is given by the radial position of the pads involved in the measurement. There were 21 rows of cathode pads arranged in concentric circles around the axis. Thus, the TPC measured up to 21 three-dimensional space points per track.

Because of the magnetic field, the trajectory of a charged particle inside the TPC was a helix, and its projection onto the end plate was an arc of a circle. By measuring the curvature of such an arc, the transverse momentum (p_T) of tracks was determined. The TPC alone had a resolution of $\sigma(1/p_T) = 1.2 \times 10^{-3}(\mathrm{GeV/c})^{-1}$, measured with 45 GeV muons from Z decays. However, $\sigma(1/p_T) = 0.6 \times 10^{-3}(\mathrm{GeV/c})^{-1}$ could be achieved when the tracking information from VDET, ITC and TPC was combined.

In addition to its role as a tracking device, the TPC also contributed to the charged particle identification by measuring their energy loss by ionization per unit distance (dE/dx), as the size of the signal in the sense-wires (up to 340 for tracks traversing the full radial range) was proportional to this magnitude. Since dE/dx depends only on the particle velocity for a given material, a combination of dE/dx and momentum measurements allowed the mass, and thus the identity of the charged particle, to be deduced.

Figure 4.3 was extracted from the TPC online event display. It shows the view along the beam direction and the side view of a hadronic event in ALEPH.

- **Electromagnetic Calorimeter (ECAL):** It was a lead proportional wire chamber sampling calorimeter of a nominal thickness of 22 radiation lengths. It consisted of a barrel surrounding the TPC and was closed at each end by an end-cap. It lied inside the superconducting magnet coil to minimize the amount of material preceding it, and covered 98% of the solid angle. Photons, electrons and positrons interacted with the field of the lead atoms, thereby initiating electromagnetic showers through e^+e^- pair production and photon bremsstrahlung. The energy and position of each shower were read out using small cathode pads, which were connected internally to form towers which point to the interaction point and provided an average granularity of $0.9^\circ \times 0.9^\circ$. This fine segmentation provided excellent identification of photons, electrons and neutral pions within jets. The energy resolution for electromagnetic clusters was parameterized as $\sigma(E)/E = 0.18/\sqrt{E/\mathrm{GeV}} + 0.009$, and the angular resolution for photons $\sigma_{\theta,\phi} = (2.5/\sqrt{E/\mathrm{GeV}} + 0.25)\mathrm{mrad}$.

- **Hadronic Calorimeter (HCAL):** It was a sampling calorimeter consisting of layers of plastic streamer tubes separated by iron slabs. The iron structure was the main mechanical support of the ALEPH detector, and it served both as the return yoke of the magnet as well as a muon filter. HCAL was used to measure hadronic

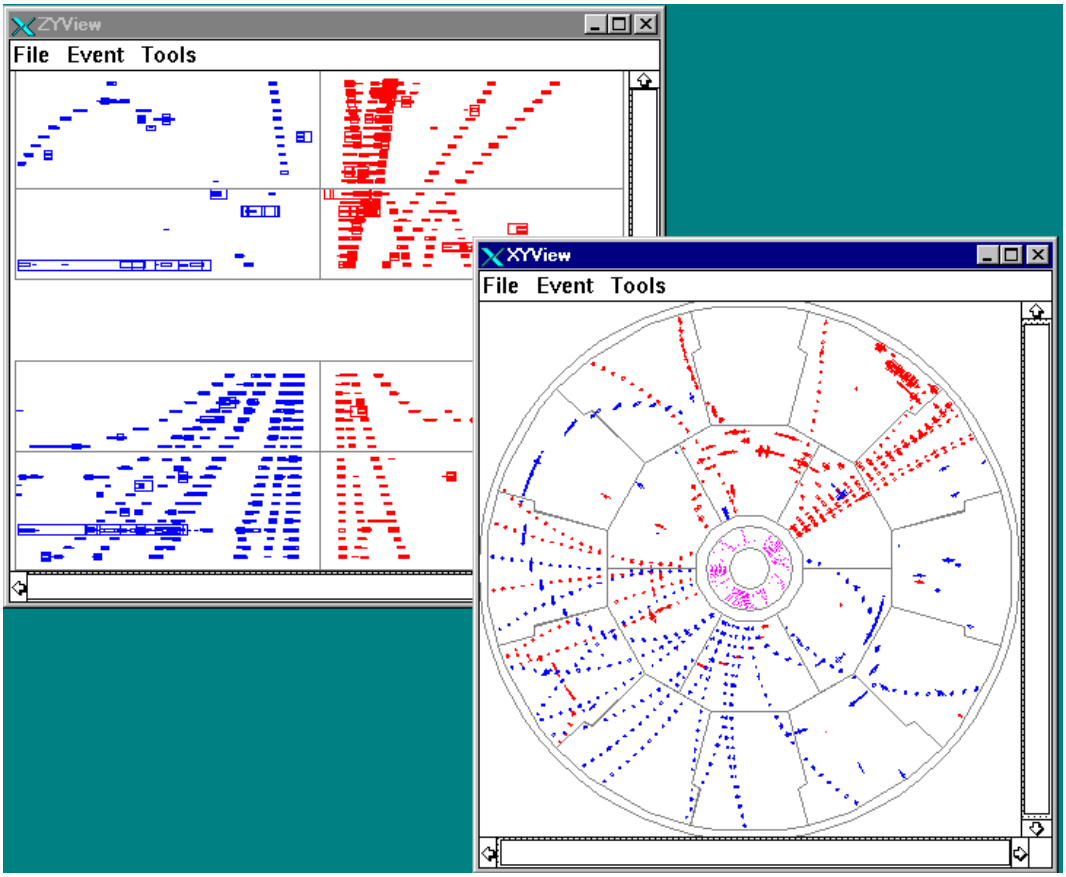

Figure 4.3: A hadronic event from the TPC online event display.

energy deposits (together with ECAL), and it was part of the muon identification system. It had a tower readout similar to ECAL with a granularity of $3.7° \times 3.7°$. In addition, a digital signal was recorded for each of the streamer tubes, providing a two-dimensional ($r\phi$) projection of the energy deposition. The energy resolution was $\sigma(E)/E = 0.85/\sqrt{E/\mathrm{GeV}}$.

- **Muon Chambers:** Muon identification was completed by the muon chambers, located beyond the HCAL. They were formed by two double layers of streamer tubes and gave a measurement of the x and y coordinates for tracks traversing the chambers.

4.2.2 The Trigger System

At LEP1 with four bunches per beam, a beam crossing occurred after every 22 μsec. If we take into account the LEP luminosity and the hadronic cross section, one hadronic

Z decay was expected every 0.3 sec on average. The purpose of the trigger system was to identify events coming from electron-positron annihilation while reducing the rate of background events. The main background came from collisions of beam particles with residual gas in the beam pipe, bremsstrahlung photons, off-momentum beam electrons which hit the beam pipe walls, and cosmic rays traversing the detector top to bottom. As every time an event was recorded by ALEPH, the information from all the subdetectors had to be read out, collected and combined to make a complete picture of the event, the trigger system also had to filter the events in order not to exceed the storage capacity, to minimize the dead time due to the detector read out, and to reduce the time that the TPC gate was open.

The requirements of the system lead to a three-level system. Level-1 decided within 5 μsec after the beam crossing whether or not to read out all detector elements. It had to identify whether there was a good charged track (from the ITC) and/or particle energy (from the calorimeters) to justify waiting for the TPC trigger signals. An important task of the Level-1 trigger was to keep the TPC operational, by deciding when the gate should be kept open for the full drift time. The Level-2 trigger simply seeked to verify a Level-1 charged track trigger by replacing the ITC tracking information with that from the TPC. It occurred about 50 μsec after beam crossing. A Level-3 software trigger was used to reduce the amount of recorded data by eliminating unwanted events.

Hadronic Z decays were collected using a Level-1 trigger in which energy deposits in ECAL were greater than 6 GeV in the barrel or 3 GeV in the end-cap or greater than 1.5 GeV in both end-caps in coincidence. A second Level-1 trigger possibility was that track segments in the drift chamber coincided with hits in a module of the hadron calorimeter, so requiring a certain penetration depth. This trigger was sensitive to muons and, with lower efficiency, to hadrons. The combination of these trigger requirements provided an efficiency of greater than 99.9% for selecting hadronic decays.

4.2.3 Data Acquisition System

Following a Level-2 YES decision, the data acquisition system (DAQ) was in charge of handling the information from all the subdetectors. The ALEPH DAQ was organized in a tree structure, with a strong hierarchy, implying that components on the same level do not communicate with each other. The different subdetectors readout was performed in parallel and asynchronously. The information was collected in a microprocessor called the Main Event Builder, where it was synchronized. The date was then sent to a computer

in the surface where it was checked by the Level-3 software and finally written to disk.

4.2.4 Energy Flow Determination

The Energy Flow algorithm [36] was meant to improve the visible energy resolution in ALEPH by combining the measurements of track momenta, calorimeter energy deposits and particle identification. It built a set of *energy flow objects* (electrons, muons, photons, charged and neutral hadrons) which should be a close representation of the stable particles actually produced in the collision.

In a first stage, charged tracks and calorimeter clusters were subjected to a cleaning procedure to reject badly reconstructed tracks and noise from the calorimeters. Then the charged particle tracks were extrapolated to the calorimeters, and groups of topologically connected tracks and clusters (called *calorimeter objects*) were formed. From these calorimeter objects the following pieces were then removed:

- Charged tracks identified as electrons, together with the associated energy in ECAL. If the energy in the calorimeter was larger than expected within a certain range, the excess energy was assumed to come from a bremsstrahlung photon, and it was counted as neutral electromagnetic energy.
- Charged tracks identified as muons, together with a maximum of 1 GeV from the closest associated ECAL deposit (if any) and a maximum of 400 MeV per plane fired around the extrapolation of the muon track from the corresponding HCAL cluster.
- identified photons and π^0s (they are counted as neutral electromagnetic energy).

At this point only charged and neutral hadrons should be left in the calorimeters. Charged hadrons were identified as all the remaining charged tracks, and the pion mass was assumed for them. Neutral hadrons were identified as a significant excess of calorimeter energy.

Using the energy flow algorithm, the resulting energy resolution was parameterized as

$$\frac{\sigma(E)}{E} = \frac{(0.59 \pm 0.03)}{\sqrt{E/\mathrm{GeV}}} + (0.6 \pm 0.3),$$

which represents a factor of two improvement with respect to the energy resolution obtained when adding up the raw energy of the calorimetric cells.

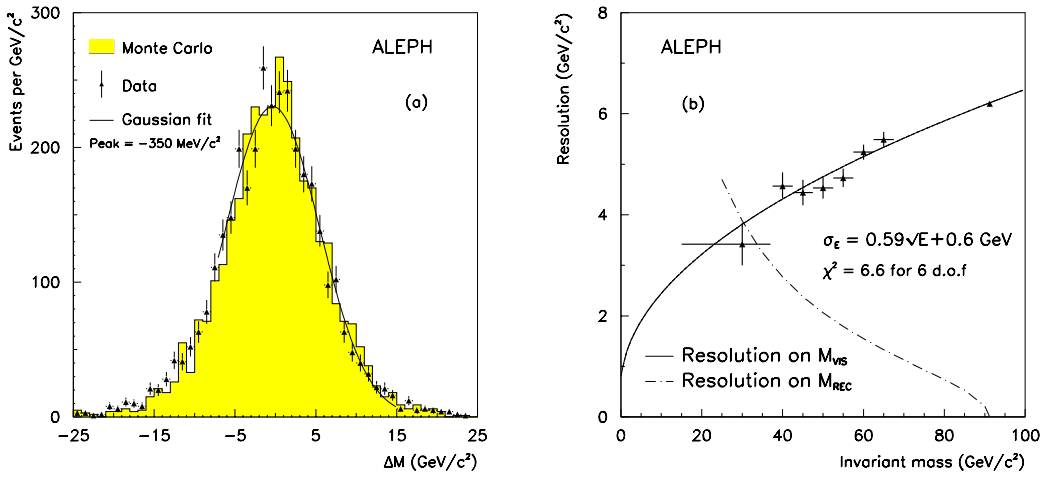

Figure 4.4: (a) Distribution of Δm for hadronic events accompanied by an isolated-energetic photon, both for Data and Monte Carlo. (b) Evolution of the resolution on $m_{\rm vis}$ and $m_{\rm rec}$ with the hadronic mass. The full line indicates the result of the fit to a calorimetric-like resolution.

The estimation of the energy resolution was done with 3225 ALEPH hadronic events accompanied by an isolated energetic photon (or π^0). For each event, the invariant mass of the system is calculated by two methods: the direct determination of the visible mass, $m_{\rm vis}$, using the energy flow algorithm, and the computation of the mass $m_{\rm rec}$ recoiling against the well-determined photon energy. Then, the distribution $\Delta m = m_{\rm vis} - m_{\rm rec}$ was measured and showed a good agreement with the one coming from fully simulated hadronic events, see Fig. 4.4 (a). However, since the resolution achieved for $m_{\rm rec}$ depends strongly on the hadronic mass, the event sample had to be divided into several subsamples to compute the corresponding resolution on $m_{\rm vis}$; this was calculated by unfolding the contribution from $m_{\rm rec}$ from the resolution on Δm. Fig. 4.4(b) shows the result of the fit.

Chapter 5

Analysis Description

Lo que sabe hacer no lo enseñan en la escuela,
que es materia superior.
Pudo ser mejor, pero nuestro baile acaba.

Two kinds of measurements have been performed in the present thesis. First, measurements of the strong coupling constant from the four-jet rate were performed. Second, a simultaneous measurement of the strong coupling constant and the colour factors was performed using the four-jet rate and the four-jet angular correlations, all of them as defined in Chapter 3. The results of these analyses will be discussed in the next chapter. Here, the analysis procedure, common to both measurements, is described.

First, some details of the event selection are given. Then, the theoretical predictions are described, followed by an explanation of the corrections applied to have a theoretical prediction at detector level to be compared to the data. Afterwards, the strategy of the fit procedure is given. Finally, the sources of systematic uncertainty studied as well as the method used to combine the different contributions into the total systematic error are detailed.

5.1 Event Selection

Y quedaba mucho por hacer.
Limpiar de malas hierbas el prado,
arrancar las rejas y cercados.

In the analyses data from 1994 and 1995 are used, taken at and around the Z peak by the ALEPH detector. First a hadronic selection is applied. Charged particle tracks

are selected that have at least four measured space coordinates from the TPC, a polar angle in the range $18^\circ < \theta < 162^\circ$, and a transverse momentum with respect to the beam direction of $p_t > 0.2$ GeV/c. In addition, the closest radial distance of approach of the extrapolated track to the beam axis, d_0, is required to be less than 2 cm, and the z coordinate of the point of closest radial approach, z_0, is required to be less than 10 cm. Using these selected charged tracks, the total charged energy $E_{\rm ch} = \sum_i \sqrt{p_i^2 + m_\pi^2}$ is computed. A minimum of four tracks are requested for the TPC as studies on the track finding efficiency showed that in hadronic Z events 98.6% of tracks that cross at least four pad rows in the TPC are successfully reconstructed [37].

Neutral energy-flow objects are kept if their polar angle with respect to the beam axis is in the range $18^\circ < \theta < 162^\circ$. This cut is applied in order to avoid the low angle regions since for neutral particles these regions are not well described by the detector simulation. Events are selected that have at least five selected charged particle tracks and $E_{\rm ch} > 15$ GeV. Only events with $|\cos\Theta_{\rm Sph}| < 0.9$ are kept, where $\Theta_{\rm Sph}$ is the polar angle of the sphericity axis, computed from all charged and neutral particles as obtained from the energy-flow algorithm.

The sphericity axis is defined as follows. The momentum tensor $M_{\alpha\beta} = \sum_j p_{\alpha j} p_{\beta j}$, can be diagonalized so that its normalized eigenvalues Q_i fulfill $Q_1 + Q_2 + Q_3 = 1$. If they are ordered such that $0 < Q_1 < Q_2 < Q_3$, then the Sphericity is defined as $S = \frac{3}{2}(Q_1 + Q_2)$. The eigenvector $\vec{n}_3$ determines the sphericity axis, and $\vec{n}_2$ and $\vec{n}_3$ define the event plane. The cut on the sphericity axis ensures that the event is well contained within the detector.

According to the MC simulation, this basic hadronic event selection is about 90.2% efficient. Non-hadronic background, which is dominated by $\tau^+\tau^-$ events, represents about 0.3% of this sample. After the selection, a sample of 2.5 million hadronic events remains for further analysis.

The hadronic events are clustered into four jets by means of the Durham clustering algorithm [38], with the E recombination scheme. The metric

$$y_{ij} = \frac{2\min(E_i^2, E_j^2)}{E_{\rm vis}^2}(1 - \cos\theta_{ij}) \tag{5.1}$$

is used, i.e. those particles (i and j) with the smallest y_{ij} are clustered together to form a new pseudo-particle with four-momentum

$$E_{\rm new} = E_i + E_j \quad , \quad \vec{p}_{\rm new} = \vec{p}_i + \vec{p}_j \, . \tag{5.2}$$

The clustering procedure is repeated until four jets are left. Finally, the event is further used provided that the fraction of electromagnetic energy in each jet is smaller than 90%, to avoid high energy photons coming from final state radiation from quarks. At this point, all the selected events are used for the calculation of the four-jet rate, when the number of four-jet events at each resolution parameter value is obtained.

Next, the energies of the jets are subsequently rescaled, to improve the resolution, by imposing total energy-momentum conservation. The assumption that the four jet directions are perfectly measured is made, since ALEPH has better angular than energy resolution. Thus, the following system of linear equations is solved in order to find the rescaled energies E_i, which are required to be positive:

$$\begin{aligned} \vec{\beta}_1 E_1 + \vec{\beta}_2 E_2 + \vec{\beta}_3 E_3 + \vec{\beta}_4 E_4 &= \vec{0} \\ E_1 + E_2 + E_3 + E_4 &= \sqrt{s} \end{aligned} \tag{5.3}$$

The velocities $\vec{\beta}_i = \vec{p}_i^{\,\mathrm{meas}}/E_i^{\mathrm{meas}}$ are fixed, $\vec{p}_i^{\,\mathrm{meas}}$ and E_i^{meas} are the measured momentum and energy. The Durham metric is recalculated and the event is taken as a four-jet event if $\min_{ij=1,4} y_{ij} > y_{\mathrm{cut}}$, with $\mathrm{y_{cut}}$=0.008. For this resolution parameter, $\mathrm{y_{cut}}$, the number of events selected for the calculation of the four-jet angular correlations is about 163,000. The chosen $\mathrm{y_{cut}}$ value represents a compromise between high statistics and good separation of the four jets.

The binned distributions of the angular correlations and the four-jet rate for different values of the resolution parameter are computed taking all selected charged and neutral energy-flow objects. Twenty equally-sized bins are used for each angular observable, and the four-jet rate is measured at 60 equidistant points in the range $-12 \leq \ln(\mathrm{y_{cut}}) \leq -0.2$.

The analyses also use 5.3 million simulated hadronic events produced with a generator based on the JETSET 7.4 parton shower model. The production rates, decay modes and lifetimes of heavy hadrons are adjusted to agree with recent measurements, while heavy quarks are fragmented using the Peterson *et al.* model [39]. Detector effects are simulated using the GEANT package [40].

5.2 The Theoretical Prediction

The NLO perturbative predictions for the angular correlations and the four-jet rate were obtained with the MC program DEBRECEN 2.0 [41].

DEBRECEN is a collection of C++ libraries that implement the dipole formalism for calculating next-to-leading order corrections to multi-jet final states. The version used in the analyses of this thesis contains programs that can be used to calculate the gauge group independent kinematical functions, see Eqs. 3.7 and 3.8, at leading and next-to-leading order for any three- and four-jet-like quantity as well as the leading order functions for the production of five jets in electron-positron annihilation. These functions can be calculated either in the pure QCD case, or taking into account the contributions from a light gluino. This second option will be referred to as the QCD+gluino case. Only infrared- and collinear-safe observables can be calculated with DEBRECEN. These quantities have to be experimentally (theoretically) defined in such a way that their actual value is independent of the number of soft and collinear hadrons (partons) produced in the final state.

More than 100 million events were generated using DEBRECEN. The coefficients of the B and C functions can be found in Tables 5.1, 5.2, 5.3, 5.4, 5.5, 5.6, 5.7, 5.8 for the four-jet angular correlations, and in Tables 5.9, 5.10 and 5.11 for the four-jet rate, where the third table gives the added functions when taking $SU(3)$ values for the colour factor ratios. These combined functions are the ones to be used for the measurement of the strong coupling constant from the four-jet rate.

5.3 Corrections

5.3.1 Hadronization Corrections

The theoretical predictions have to be corrected to take into account hadronization as well as detector effects before being compared to data. The hadronization corrections have been implemented separately for the four-jet rate and the angular correlations as detailed below.

Corrections for R_4

For the four-jet rate, for which the resummation of large logarithms exists, the hadronization corrections have been computed using R_4 distributions at parton and at hadron level. Here, the parton level refers to the set of partons present after the showering process. Then the correction factors for each y_{cut} are computed according to

$$C^{had}(y_{cut}) = \frac{R_4^{had}(y_{cut})}{R_4^{part}(y_{cut})} \quad . \tag{5.4}$$

$\lvert\cos\chi_{\rm BZ}\rvert$	$B_0(y_{\rm cut})$	$B_x(y_{\rm cut})$	$B_y(y_{\rm cut})$
0.025	37.68 ± 0.06	1.96 ± 0.01	11.99 ± 0.01
0.075	37.70 ± 0.06	1.91 ± 0.01	11.85 ± 0.01
0.125	37.30 ± 0.06	2.05 ± 0.01	11.68 ± 0.01
0.175	37.42 ± 0.06	2.14 ± 0.01	11.50 ± 0.01
0.225	37.17 ± 0.06	2.22 ± 0.01	11.28 ± 0.01
0.275	37.54 ± 0.05	2.38 ± 0.01	10.98 ± 0.01
0.325	38.18 ± 0.06	2.44 ± 0.01	10.75 ± 0.01
0.375	38.54 ± 0.05	2.712 ± 0.009	10.48 ± 0.01
0.425	39.58 ± 0.06	2.795 ± 0.009	10.17 ± 0.01
0.475	40.27 ± 0.05	3.049 ± 0.009	9.86 ± 0.01
0.525	41.51 ± 0.06	3.227 ± 0.009	9.49 ± 0.01
0.575	43.08 ± 0.06	3.48 ± 0.01	9.175 ± 0.009
0.625	44.59 ± 0.05	3.79 ± 0.01	8.844 ± 0.008
0.675	47.36 ± 0.06	4.13 ± 0.01	8.556 ± 0.007
0.725	50.21 ± 0.06	4.51 ± 0.01	8.230 ± 0.007
0.775	54.08 ± 0.06	4.98 ± 0.01	7.934 ± 0.006
0.825	58.47 ± 0.06	5.46 ± 0.01	7.648 ± 0.006
0.875	64.43 ± 0.06	6.18 ± 0.01	7.383 ± 0.005
0.925	73.74 ± 0.07	7.57 ± 0.02	7.655 ± 0.005
0.975	155.1 ± 0.1	17.20 ± 0.02	13.933 ± 0.006

Table 5.1: B functions at different values of $\lvert\cos\chi_{\rm BZ}\rvert$ from DEBRECEN. The first column shows the center of bin value.

The superscript "had" ("part") refers to the hadron (parton) level. The prediction corrected to hadron level (HL), $R_4^{\rm corrHL}(y_{\rm cut})$, is obtained from the theoretical prediction, $R_4^{\rm TH}(y_{\rm cut})$, according to

$$R_4^{\rm corrHL}(y_{\rm cut}) = C^{\rm had}(y_{\rm cut}) R_4^{\rm TH}(y_{\rm cut}) \quad . \tag{5.5}$$

The JETSET parton shower model together with the Lund string fragmentation scheme (PYTHIA 6.1) is employed for the calculation of the hadronization corrections. The model parameters have been taken from [37], with the exception that final state radiation is not included in the simulation.

A similar approach for the description of the parton level is taken by the HERWIG

$\lvert\cos\chi_{\rm BZ}\rvert$	$C_0(\mathrm{y_{cut}})$	$C_x(\mathrm{y_{cut}})$	$C_y(\mathrm{y_{cut}})$	$C_{xx}(\mathrm{y_{cut}})$	$C_{xy}(\mathrm{y_{cut}})$	$C_{yy}(\mathrm{y_{cut}})$
0.025	-174 ± 7	762 ± 13	-1653 ± 7	26 ± 4	161 ± 3	-400.9 ± 0.6
0.075	-166 ± 10	715 ± 18	-1647 ± 9	36 ± 5	144 ± 15	-396.0 ± 0.6
0.125	-177 ± 10	745 ± 18	-1653 ± 9	30 ± 5	162 ± 15	-389.8 ± 0.6
0.175	-171 ± 13	726 ± 17	-1633 ± 8	38 ± 5	140 ± 4	-382.0 ± 0.5
0.225	-157 ± 12	751 ± 32	-1646 ± 7	27 ± 8	135 ± 5	-373.6 ± 0.5
0.275	-171 ± 11	748 ± 33	-1659 ± 8	45 ± 8	126 ± 4	-364.5 ± 0.5
0.325	-149 ± 13	727 ± 18	-1678 ± 8	43 ± 5	111 ± 3	-354.9 ± 0.5
0.375	-177 ± 11	753 ± 17	-1691 ± 8	44 ± 5	94 ± 4	-343.9 ± 0.5
0.425	-172 ± 8	787 ± 17	-1720 ± 8	51 ± 5	81 ± 3	-333.9 ± 0.4
0.475	-179 ± 22	830 ± 26	-1771 ± 7	41 ± 7	66 ± 3	-324.6 ± 0.4
0.525	-180 ± 25	789 ± 29	-1817 ± 7	63 ± 8	49 ± 3	-313.1 ± 0.4
0.575	-161 ± 18	831 ± 21	-1874 ± 7	70 ± 6	25 ± 3	-301.9 ± 0.4
0.625	-186 ± 9	906 ± 18	-1973 ± 7	68 ± 4	3 ± 2	-291.3 ± 0.3
0.675	-191 ± 10	913 ± 15	-2066 ± 6	80 ± 4	-19 ± 2	-281.3 ± 0.3
0.725	-222 ± 11	1011 ± 13	-2196 ± 6	80 ± 4	-44 ± 2	-271.1 ± 0.3
0.775	-242 ± 9	1088 ± 13	-2354 ± 6	83 ± 3	-74 ± 2	-261.0 ± 0.3
0.825	-276 ± 10	1179 ± 16	-2567 ± 6	105 ± 4	-111 ± 2	-252.0 ± 0.2
0.875	-287 ± 12	1277 ± 20	-2827 ± 6	123 ± 5	-151 ± 2	-243.6 ± 0.2
0.925	-346 ± 12	1511 ± 20	-3256 ± 7	144 ± 4	-214 ± 2	-248.8 ± 0.2
0.975	-752 ± 12	3129 ± 16	-6849 ± 9	320 ± 5	-562 ± 3	-444.3 ± 0.2

Table 5.2: C functions at different values of $\lvert\cos\chi_{\rm BZ}\rvert$ from DEBRECEN. $C_z(\mathrm{y_{cut}})$ was found to be very small and therefore is not tabulated. The first column shows the center-of-bin value.

6.1 program. However, there the fragmentation is modelled according to the cluster fragmentation scheme.

Two similar and extreme approaches can be tested by using the matrix element (ME) option in the PYTHIA program, or a special PYTHIA production which has on average four partons after the parton shower. In order to achieve this the parton shower cut-off parameter, Q_0, has been increased to 4 GeV, and afterwards the fragmentation parameters have been retuned so that the hadron level describes the data (this approach will be called PYTHIA,Q_0 from now on). In the ME option (namely PYTHIA,ME) at the parton level two-, three- and four-parton final states are generated according to the exact NLO matrix elements, and then the hadronization step is performed via the string fragmentation scheme. This model should give a better description of four-jet related quantities.

$\cos\Phi_{\mathrm{KSW}}$	$B_0(y_{\mathrm{cut}})$	$B_x(y_{\mathrm{cut}})$	$B_y(y_{\mathrm{cut}})$
-0.95	34.66 ± 0.03	6.39 ± 0.01	3.917 ± 0.002
-0.85	20.22 ± 0.02	3.725 ± 0.007	3.602 ± 0.003
-0.75	19.25 ± 0.02	3.627 ± 0.007	4.569 ± 0.004
-0.65	18.97 ± 0.02	3.543 ± 0.007	5.214 ± 0.005
-0.55	19.49 ± 0.02	3.435 ± 0.006	5.682 ± 0.006
-0.45	20.03 ± 0.02	3.208 ± 0.005	5.934 ± 0.006
-0.35	20.90 ± 0.02	2.985 ± 0.005	6.062 ± 0.007
-0.25	21.87 ± 0.03	2.746 ± 0.004	6.132 ± 0.007
-0.15	22.62 ± 0.03	2.460 ± 0.003	6.011 ± 0.007
-0.05	23.62 ± 0.03	2.222 ± 0.003	5.767 ± 0.007
0.05	21.41 ± 0.03	1.689 ± 0.003	5.242 ± 0.006
0.15	20.76 ± 0.03	1.417 ± 0.003	4.838 ± 0.005
0.25	20.69 ± 0.03	1.186 ± 0.003	4.539 ± 0.005
0.35	20.98 ± 0.03	0.941 ± 0.003	4.261 ± 0.005
0.45	21.33 ± 0.03	0.764 ± 0.004	4.046 ± 0.004
0.55	22.32 ± 0.03	0.630 ± 0.005	3.873 ± 0.004
0.65	23.81 ± 0.03	0.487 ± 0.005	3.798 ± 0.004
0.75	26.63 ± 0.03	0.381 ± 0.006	3.828 ± 0.004
0.85	32.90 ± 0.04	0.211 ± 0.007	4.197 ± 0.004
0.95	74.52 ± 0.06	0.05 ± 0.01	8.185 ± 0.005

Table 5.3: B functions at different values of $\cos\Phi_{\mathrm{KSW}}$ from DEBRECEN. The first column shows the center-of-bin value.

However, it is known not to describe well the energy evolution of basic quantities such as the charged multiplicity [42].

Corrections for the angular observables

For the angular correlations a different MC simulation is used. Still using PYTHIA 6.1, the option to start a parton shower from a four-parton configuration is chosen [43]. This MC simulation should better describe our data provided that two- and three-jet backgrounds are negligible, and that the showering and hadronization processes are well modelled. The parameters for the showering and hadronization are identical to the simulation used for the four-jet rate.

$\cos\Phi_{\mathrm{KSW}}$	$C_0(\mathrm{y_{cut}})$	$C_x(\mathrm{y_{cut}})$	$C_y(\mathrm{y_{cut}})$	$C_{xx}(\mathrm{y_{cut}})$	$C_{xy}(\mathrm{y_{cut}})$	$C_{yy}(\mathrm{y_{cut}})$
-0.95	-158 ± 3	653 ± 4	-1501 ± 2	129 ± 2	-236 ± 1	-128.06 ± 0.09
-0.85	-81 ± 3	378 ± 5	-884 ± 3	77 ± 1	-112 ± 1	-125.0 ± 0.1
-0.75	-73 ± 3	355 ± 4	-832 ± 3	74 ± 2	-88 ± 1	-158.8 ± 0.2
-0.65	-72 ± 3	350 ± 4	-829 ± 3	74 ± 2	-66 ± 2	-180.6 ± 0.2
-0.55	-75 ± 3	367 ± 6	-848 ± 3	71 ± 2	-47 ± 1	-194.9 ± 0.2
-0.45	-83 ± 5	377 ± 7	-878 ± 3	63 ± 2	-31 ± 2	-203.4 ± 0.3
-0.35	-76 ± 5	394 ± 7	-908 ± 5	60 ± 2	-17 ± 2	-206.3 ± 0.3
-0.25	-93 ± 3	427 ± 6	-957 ± 4	51 ± 1	2 ± 2	-205.3 ± 0.3
-0.15	-92 ± 3	429 ± 6	-995 ± 4	49 ± 1	8 ± 1	-201.0 ± 0.3
-0.05	-106 ± 7	464 ± 5	-1035 ± 4	42 ± 1	16 ± 1	-192.0 ± 0.3
0.05	-81 ± 7	430 ± 7	-953 ± 4	30 ± 1	32 ± 1	-174.1 ± 0.2
0.15	-95 ± 4	420 ± 6	-915 ± 4	23 ± 1	37 ± 1	-158.7 ± 0.2
0.25	-88 ± 4	415 ± 5	-910 ± 4	20 ± 1	42 ± 1	-147.3 ± 0.2
0.35	-86 ± 4	424 ± 5	-915 ± 3	16 ± 1	44 ± 1	-137.2 ± 0.2
0.45	-102 ± 4	445 ± 5	-937 ± 3	8 ± 1	49.8 ± 0.9	-129.1 ± 0.2
0.55	-103 ± 4	450 ± 5	-971 ± 3	8 ± 1	50.6 ± 0.9	-123.1 ± 0.2
0.65	-113 ± 4	496 ± 6	-1049 ± 3	2 ± 1	56.2 ± 0.9	-119.5 ± 0.1
0.75	-128 ± 5	549 ± 7	-1178 ± 3	0 ± 2	65 ± 2	-120.2 ± 0.1
0.85	-163 ± 7	684 ± 7	-1448 ± 3	-7 ± 2	78 ± 1	-130.6 ± 0.1
0.95	-398 ± 6	1581 ± 8	-3320 ± 5	-33 ± 3	176 ± 2	-251.3 ± 0.2

Table 5.4: C functions at different values of $\cos\Phi_{\mathrm{KSW}}$ from DEBRECEN. $C_z(\mathrm{y_{cut}})$ was found to be very small and therefore is not tabulated. The first column shows the center-of-bin value.

An important parameter in this four-parton MC simulation is the so called intrinsic jet resolution parameter $\mathrm{y_{int}}$. The rejection of four-parton configurations with a $\mathrm{y_{34}}$ (jet resolution parameter when going from four to three jets) smaller than $\mathrm{y_{int}}$ is used to avoid soft and collinear divergences. The parameter $\mathrm{y_{int}}$ has to be smaller than $\mathrm{y_{cut}}$, but going to very small values is not possible for technical reasons. Therefore, it is not a suitable MC for the four-jet rate, which is calculated at different $\mathrm{y_{cut}}$ values over a large range. The value used for the MC simulation in order to correct the angular distributions was $\mathrm{y_{int}}$=0.004.

Using this four-parton option 15 million events were generated with about 8 million four-jet events selected at $\mathrm{y_{cut}} = 0.008$. The angular distributions are calculated at three levels: parton level before showering (i.e. using massless LO matrix elements for 4 par-

$\lvert\cos\theta_{\rm NR}\rvert$	$B_0(\mathrm{y_{cut}})$	$B_x(\mathrm{y_{cut}})$	$B_y(\mathrm{y_{cut}})$
0.025	39.96 ± 0.05	2.76 ± 0.01	13.72 ± 0.01
0.075	40.49 ± 0.05	2.80 ± 0.01	13.65 ± 0.01
0.125	40.29 ± 0.05	2.92 ± 0.01	13.53 ± 0.01
0.175	41.03 ± 0.05	2.91 ± 0.01	13.33 ± 0.01
0.225	41.38 ± 0.05	3.04 ± 0.01	13.13 ± 0.01
0.275	42.42 ± 0.05	3.23 ± 0.01	12.74 ± 0.01
0.325	42.97 ± 0.05	3.32 ± 0.01	12.30 ± 0.01
0.375	44.56 ± 0.05	3.43 ± 0.01	11.94 ± 0.01
0.425	45.77 ± 0.06	3.64 ± 0.01	11.42 ± 0.01
0.475	47.40 ± 0.06	3.91 ± 0.01	10.89 ± 0.01
0.525	49.02 ± 0.06	4.12 ± 0.01	10.32 ± 0.01
0.575	50.96 ± 0.06	4.37 ± 0.01	9.682 ± 0.009
0.625	52.93 ± 0.06	4.63 ± 0.01	9.052 ± 0.009
0.675	55.38 ± 0.06	4.83 ± 0.01	8.396 ± 0.008
0.725	57.52 ± 0.07	5.08 ± 0.01	7.654 ± 0.007
0.775	59.59 ± 0.07	5.32 ± 0.01	6.930 ± 0.006
0.825	60.97 ± 0.07	5.52 ± 0.01	6.155 ± 0.005
0.875	61.31 ± 0.07	5.73 ± 0.01	5.411 ± 0.004
0.925	63.00 ± 0.07	6.00 ± 0.01	4.773 ± 0.004
0.975	77.03 ± 0.08	6.64 ± 0.02	4.371 ± 0.003

Table 5.5: B functions at different values of $\lvert\cos\theta_{\rm NR}\rvert$ from DEBRECEN. The first column shows the center-of-bin value.

tons), parton level after showering and hadron level. In order to correct not only for the hadronization effects, but also for the missing higher orders, the bin-by-bin ratios of the distribution at hadron level over the one at parton level are calculated,

$$C^{\rm bck+had}(i_{bin}) = \frac{\cos X^{\rm had}(i_{bin})}{\cos X^{\rm part}(i_{bin})} \quad , \tag{5.6}$$

where now "part" refers to parton level before showering. The predictions corrected to hadron level are then obtained as

$$\cos X^{\rm corrHL}(i_{bin}) = C^{\rm bck+had}(i_{bin}) \cos X^{\rm TH}(i_{bin}) \quad . \tag{5.7}$$

$\lvert\cos\theta_{\rm NR}\rvert$	$C_0(y_{\rm cut})$	$C_x(y_{\rm cut})$	$C_y(y_{\rm cut})$	$C_{xx}(y_{\rm cut})$	$C_{xy}(y_{\rm cut})$	$C_{yy}(y_{\rm cut})$
0.025	-175 ± 5	746 ± 8	-1760 ± 7	46 ± 3	156 ± 3	-453.1 ± 0.6
0.075	-174 ± 14	749 ± 14	-1770 ± 9	52 ± 6	134 ± 16	-452.2 ± 0.6
0.125	-162 ± 14	786 ± 14	-1771 ± 10	41 ± 6	161 ± 16	-450.1 ± 0.6
0.175	-174 ± 6	768 ± 10	-1773 ± 12	53 ± 4	140 ± 5	-438.6 ± 0.6
0.225	-159 ± 6	785 ± 10	-1815 ± 11	52 ± 4	135 ± 5	-434.2 ± 0.6
0.275	-171 ± 7	791 ± 11	-1851 ± 8	54 ± 4	108 ± 5	-418.7 ± 0.5
0.325	-183 ± 6	832 ± 22	-1892 ± 9	58 ± 7	102 ± 4	-409.6 ± 0.5
0.375	-191 ± 6	839 ± 22	-1938 ± 9	59 ± 6	84 ± 4	-394.1 ± 0.5
0.425	-183 ± 7	888 ± 11	-1991 ± 8	65 ± 4	71 ± 3	-379.6 ± 0.4
0.475	-209 ± 7	932 ± 12	-2078 ± 8	68 ± 4	47 ± 3	-360.9 ± 0.4
0.525	-218 ± 7	963 ± 12	-2141 ± 7	72 ± 3	21 ± 3	-342.1 ± 0.4
0.575	-224 ± 7	1021 ± 13	-2237 ± 8	76 ± 3	-6 ± 3	-322.2 ± 0.4
0.625	-237 ± 7	1058 ± 13	-2330 ± 9	89 ± 6	-27 ± 3	-298.5 ± 0.3
0.675	-262 ± 8	1113 ± 13	-2438 ± 8	82 ± 5	-55 ± 3	-275.8 ± 0.3
0.725	-258 ± 8	1188 ± 11	-2530 ± 7	92 ± 4	-84 ± 4	-251.8 ± 0.3
0.775	-274 ± 11	1228 ± 15	-2616 ± 8	101 ± 4	-112 ± 2	-226.2 ± 0.2
0.825	-277 ± 14	$1265. \pm 14.$	-2677 ± 7	101 ± 4	-141 ± 2	-200.8 ± 0.2
0.875	-274 ± 10	$1259. \pm 14.$	-2705 ± 7	114 ± 3	-169 ± 2	-175.5 ± 0.2
0.925	-323 ± 9	$1311. \pm 11.$	-2783 ± 6	113 ± 3	-198 ± 2	-152.3 ± 0.1
0.975	-405 ± 10	$1656. \pm 12.$	-3433 ± 7	127 ± 4	-244 ± 3	-136.4 ± 0.1

Table 5.6: C functions at different values of $\lvert\cos\theta_{\rm NR}\rvert$ from DEBRECEN. $C_z(y_{\rm cut})$ was found to be very small and therefore is not tabulated. The first column shows the center-of-bin value.

The simulation of massless four-parton configurations is also possible using the HERWIG 6.1 MC program. About 6 million events were produced, with about 2.5 million selected as four-jet events.

The ME option in PYTHIA, as was described for the four-jet rate in Section 5.3.1, is also tested for the corrections of the angular distributions.

Finally, a forth MC set was produced in order to check for mass effects. For this, the FOURJPHACT MC program is used [58], where the massive LO four-parton MEs are implied for generating the initial state. The showering and hadronization processes are modelled using PYTHIA 6.1 (standard parameters). The program allows to generate

$\cos\alpha_{34}$	$B_0(\mathrm{y_{cut}})$	$B_x(\mathrm{y_{cut}})$	$B_y(\mathrm{y_{cut}})$
-0.95	42.87 ± 0.04	-0.096 ± 0.006	3.559 ± 0.003
-0.85	38.83 ± 0.04	0.092 ± 0.006	3.680 ± 0.003
-0.75	36.79 ± 0.04	0.323 ± 0.006	3.872 ± 0.003
-0.65	34.62 ± 0.04	0.596 ± 0.006	4.072 ± 0.003
-0.55	33.00 ± 0.04	0.833 ± 0.006	4.292 ± 0.004
-0.45	31.21 ± 0.04	1.095 ± 0.005	4.526 ± 0.004
-0.35	29.93 ± 0.03	1.343 ± 0.005	4.797 ± 0.004
-0.25	28.51 ± 0.03	1.659 ± 0.005	5.074 ± 0.004
-0.15	27.62 ± 0.03	2.010 ± 0.005	5.395 ± 0.005
-0.05	26.76 ± 0.03	2.336 ± 0.005	5.781 ± 0.005
0.05	25.95 ± 0.03	2.754 ± 0.005	6.167 ± 0.006
0.15	25.18 ± 0.03	3.183 ± 0.006	6.575 ± 0.006
0.25	24.04 ± 0.03	3.640 ± 0.006	6.899 ± 0.006
0.35	22.88 ± 0.03	4.111 ± 0.007	7.171 ± 0.007
0.45	21.25 ± 0.02	4.425 ± 0.007	7.345 ± 0.007
0.55	19.43 ± 0.02	4.581 ± 0.008	7.235 ± 0.007
0.65	17.09 ± 0.02	4.393 ± 0.008	6.595 ± 0.007
0.75	13.81 ± 0.02	3.527 ± 0.007	4.978 ± 0.006
0.85	6.874 ± 0.01	1.275 ± 0.004	1.660 ± 0.003
0.95	0.338 ± 0.003	0.0186 ± 0.0003	0.0021 ± 0.0002

Table 5.7: B functions at different values of $\cos\alpha_{34}$ from DEBRECEN. The first column shows the center-of-bin value.

single final states only (such as $q\bar{q}gg$) or a correctly weighted mixture of final states.

5.3.2 Detector Corrections

The theoretical predictions, which are corrected to hadron level, have to be corrected further for detector effects such as acceptance, efficiency and resolution before being fitted to data. This is done by computing these observables from a MC before and after the detector simulation and imposing the same track and event selection cuts as for the data. Then the correction factors are computed,

$$C^{\mathrm{det}}(i_{bin}/\mathrm{y_{cut}}) = \frac{O_4^{\mathrm{det}}(i_{bin}/\mathrm{y_{cut}})}{O_4^{\mathrm{had}}(i_{bin}/\mathrm{y_{cut}})} \quad , \tag{5.8}$$

$\cos\alpha_{34}$	$C_0(\mathrm{y_{cut}})$	$C_x(\mathrm{y_{cut}})$	$C_y(\mathrm{y_{cut}})$	$C_{xx}(\mathrm{y_{cut}})$	$C_{xy}(\mathrm{y_{cut}})$	$C_{yy}(\mathrm{y_{cut}})$
-0.95	-208 ± 5	917 ± 7	-1899 ± 4	-26 ± 2	81.8 ± 0.8	-105.6 ± 0.1
-0.85	-182 ± 6	817 ± 8	-1718 ± 4	-11 ± 3	71 ± 1	-110.4 ± 0.1
-0.75	-185 ± 5	788 ± 6	-1615 ± 4	-12 ± 2	63 ± 1	-117.4 ± 0.1
-0.65	-160 ± 6	723 ± 7	-1521 ± 4	-1 ± 1	56 ± 1	-124.8 ± 0.1
-0.55	-146 ± 4	672 ± 6	-1435 ± 4	9 ± 2	49 ± 1	-132.2 ± 0.1
-0.45	-141 ± 4	641 ± 7	-1366 ± 4	11 ± 2	44 ± 2	-140.6 ± 0.1
-0.35	-141 ± 4	606 ± 6	-1300 ± 4	20 ± 2	36 ± 1	-149.5 ± 0.2
-0.25	-131 ± 4	572 ± 7	-1244 ± 4	28 ± 2	29 ± 1	-159.6 ± 0.2
-0.15	-123 ± 3	542 ± 7	-1200 ± 4	33 ± 3	19 ± 1	-171.9 ± 0.2
-0.05	-123 ± 3	529 ± 5	-1179 ± 4	43 ± 2	12 ± 1	-187.0 ± 0.2
0.05	-117 ± 4	512 ± 6	-1149 ± 4	51 ± 3	-2 ± 1	-201.5 ± 0.2
0.15	-111 ± 4	489 ± 7	-1107 ± 4	66 ± 3	-18 ± 1	-217.1 ± 0.2
0.25	-102 ± 3	455 ± 5	-1055 ± 4	76 ± 2	-30 ± 2	-231.4 ± 0.3
0.35	-98 ± 3	418 ± 5	-999 ± 4	82 ± 2	-43 ± 2	-243.5 ± 0.3
0.45	-83 ± 2	381 ± 4	-936 ± 3	95 ± 1	-60 ± 2	-253.8 ± 0.3
0.55	-72 ± 2	343 ± 4	-851 ± 3	100 ± 1	-72 ± 2	-253.6 ± 0.3
0.65	-70 ± 2	306 ± 4	-761 ± 3	95 ± 3	-78 ± 1	-238.3 ± 0.3
0.75	-48 ± 2	243 ± 4	-610 ± 3	76 ± 2	-69 ± 2	-183.7 ± 0.3
0.85	-24 ± 2	129 ± 2	-304 ± 1	23.4 ± 0.8	-29.9 ± 0.7	-63.6 ± 0.1
0.95	-1.3 ± 0.6	7.7 ± 0.8	-15.5 ± 0.3	0.4 ± 0.1	-0.54 ± 0.07	-0.86 ± 0.01

Table 5.8: C functions at different values of $\cos\alpha_{34}$ from DEBRECEN. $C_z(\mathrm{y_{cut}})$ was found to be very small and therefore is not tabulated. The first column shows the center-of-bin value.

where $O_4^{\mathrm{det}}(i_{bin}/\mathrm{y_{cut}})$ denotes the value of the observable at the detector level. The hadron level distributions are obtained by switching off any photon radiation in the initial and final state (ISR, FSR), both present at the detector level, with all particles having mean lifetimes less than 10^{-9} s required to decay, and all other particles being treated as stable. The detector level distributions come from the full MC simulation described in Section 5.1. Starting from the distributions at HL, $O_4^{\mathrm{corrHL}}(i_{bin}/\mathrm{y_{cut}})$, the detector-corrected distribution, $O_4^{\mathrm{corrDL}}(i_{bin}/\mathrm{y_{cut}})$, is obtained according to

$$O_4^{\mathrm{corrDL}}(i_{bin}/\mathrm{y_{cut}}) = C^{\mathrm{det}}(i_{bin}/\mathrm{y_{cut}}) O_4^{\mathrm{corrHL}}(i_{bin}/\mathrm{y_{cut}}) \quad . \tag{5.9}$$

The detector correction factors are typically found within the 5% range, except at the edges of the phase space where corrections up to 10-20% are observed.

$\ln(y_{cut})$	$B_0(y_{cut})$	$B_x(y_{cut})$	$B_y(y_{cut})$
-2.2	0.00939 ± 0.00003	0.000888 ± 0.000005	0.002900 ± 0.000009
-2.4	0.06333 ± 0.00009	0.005412 ± 0.00002	0.01732 ± 0.00002
-2.6	0.2318 ± 0.0002	0.01959 ± 0.00004	0.05910 ± 0.00004
-2.8	0.6059 ± 0.0004	0.05025 ± 0.00008	0.14687 ± 0.00007
-3.0	1.2991 ± 0.0006	0.1068 ± 0.0001	0.3036 ± 0.0001
-3.2	2.4394 ± 0.0009	0.1981 ± 0.0002	0.5529 ± 0.0002
-3.4	4.166 ± 0.001	0.3380 ± 0.0003	0.9220 ± 0.0002
-3.6	6.650 ± 0.002	0.5418 ± 0.0004	1.4418 ± 0.0003
-3.8	10.067 ± 0.003	0.8205 ± 0.0006	2.1424 ± 0.0005
-4.0	14.612 ± 0.004	1.1964 ± 0.0008	3.0570 ± 0.0006
-4.2	20.538 ± 0.005	1.684 ± 0.001	4.2248 ± 0.0009
-4.4	28.059 ± 0.007	2.305 ± 0.001	5.687 ± 0.001
-4.6	37.406 ± 0.009	3.087 ± 0.002	7.471 ± 0.002
-4.8	48.89 ± 0.01	4.054 ± 0.003	9.630 ± 0.002
-5.0	62.80 ± 0.02	5.232 ± 0.003	12.215 ± 0.003
-5.2	79.46 ± 0.02	6.636 ± 0.004	15.277 ± 0.004
-5.4	99.26 ± 0.03	8.319 ± 0.005	18.831 ± 0.005
-5.6	122.39 ± 0.04	10.319 ± 0.007	22.923 ± 0.006
-5.8	149.56 ± 0.05	12.642 ± 0.009	27.634 ± 0.008
-6.0	180.99 ± 0.07	15.34 ± 0.01	33.05 ± 0.01
-6.2	217.14 ± 0.09	18.48 ± 0.02	39.12 ± 0.01
-6.4	258.4 ± 0.1	22.16 ± 0.02	46.02 ± 0.02
-6.6	304.8 ± 0.1	26.32 ± 0.02	53.71 ± 0.02
-6.8	357.7 ± 0.2	31.09 ± 0.03	62.33 ± 0.03
-7.0	416.2 ± 0.2	36.47 ± 0.04	71.71 ± 0.04
-7.2	481.5 ± 0.3	42.35 ± 0.05	82.08 ± 0.05
-7.4	555.0 ± 0.4	48.92 ± 0.06	93.69 ± 0.06
-7.6	636.4 ± 0.5	56.43 ± 0.08	106.03 ± 0.07
-7.8	727.9 ± 0.6	65.2 ± 0.1	119.71 ± 0.09
-8.0	828.3 ± 0.8	74.3 ± 0.1	134.4 ± 0.1

Table 5.9: B functions for the four-jet rate from DEBRECEN at different values of y_{cut}. Bins from -0.2 to -1.8 are not tabulated because no event was found to be a four-jet event for those values of y_{cut}. The values for bins with $\ln(y_{cut})$ smaller than -8 are not in the table as we are not interested in the four-jet rate at too small y_{cut} values.

$\ln(y_{cut})$	$C_0(y_{cut})$	$C_x(y_{cut})$	$C_y(y_{cut})$	$C_{xx}(y_{cut})$	$C_{xy}(y_{cut})$	$C_{yy}(y_{cut})$
-2.2	0.032 ± 0.004	0.148 ± 0.005	-0.318 ± 0.005	0.014 ± 0.001	0.019 ± 0.002	-0.0678 ± 0.0002
-2.4	0.201 ± 0.009	1.01 ± 0.01	-2.20 ± 0.01	0.093 ± 0.003	0.106 ± 0.003	-0.4153 ± 0.0006
-2.6	0.64 ± 0.02	3.80 ± 0.02	-8.20 ± 0.02	0.334 ± 0.007	0.338 ± 0.006	-1.441 ± 0.001
-2.8	1.64 ± 0.03	10.13 ± 0.04	-21.74 ± 0.03	0.84 ± 0.01	0.76 ± 0.01	-3.677 ± 0.002
-3.0	3.18 ± 0.06	22.1 ± 0.1	-47.25 ± 0.05	1.83 ± 0.03	1.43 ± 0.02	-7.780 ± 0.003
-3.2	4.77 ± 0.07	42.09 ± 0.09	-90.01 ± 0.08	3.40 ± 0.03	2.37 ± 0.03	-14.547 ± 0.005
-3.4	6.1 ± 0.1	73.6 ± 0.2	-156.3 ± 0.1	5.82 ± 0.04	3.56 ± 0.04	-24.944 ± 0.008
-3.6	6.4 ± 0.2	119.4 ± 0.3	-254.1 ± 0.2	9.41 ± 0.07	4.86 ± 0.06	-40.07 ± 0.01
-3.8	3.3 ± 0.3	184.6 ± 0.3	-392.5 ± 0.3	14.40 ± 0.08	6.42 ± 0.08	-61.23 ± 0.02
-4.0	-6.1 ± 0.4	272.8 ± 0.4	-582.4 ± 0.4	21.1 ± 0.1	7.8 ± 0.1	-89.87 ± 0.02
-4.2	-25.3 ± 0.5	390.2 ± 0.8	-835.9 ± 0.5	29.9 ± 0.2	9.0 ± 0.2	-127.77 ± 0.03
-4.4	-61.3 ± 0.6	541.7 ± 0.9	-1167.4 ± 0.7	41.3 ± 0.3	9.1 ± 0.2	-176.72 ± 0.04
-4.6	-118.7 ± 0.9	732 ± 1	-1596.0 ± 0.8	54.9 ± 0.3	8.8 ± 0.3	-238.85 ± 0.06
-4.8	-209 ± 1	971 ± 1	-2139 ± 1	72.6 ± 0.4	6.5 ± 0.4	-316.24 ± 0.08
-5.0	-346 ± 1	1267 ± 2	-2818 ± 2	94.1 ± 0.6	1.3 ± 0.6	-412.0 ± 0.1
-5.2	-536 ± 2	1616 ± 3	-3657 ± 2	122.2 ± 0.9	-5.9 ± 0.7	-528.6 ± 0.2
-5.4	-807 ± 3	2042 ± 9	-4683 ± 3	$154 \pm 2.$	-18.0 ± 0.9	-668.5 ± 0.2
-5.6	-1173 ± 4	2555 ± 4	-5932 ± 4	188 ± 1	-33 ± 1	-835.5 ± 0.3
-5.8	$-1664 \pm 5.$	3145 ± 6	-7431 ± 4	230 ± 2	-56 ± 1	-1033.1 ± 0.4
-6.0	-2302 ± 6	3837 ± 7	-9221 ± 6	282 ± 2	-89 ± 2	-1264.1 ± 0.5
-6.2	-3135 ± 9	4634 ± 11	-11324 ± 8	339 ± 3	-135 ± 3	-1533.2 ± 0.7
-6.4	-4205 ± 11	5569 ± 13	-13810 ± 10	401 ± 4	-188 ± 3	-1841.7 ± 0.9
-6.6	-5551 ± 17	6615 ± 18	-16732 ± 13	469 ± 4	-250 ± 4	-2199 ± 1
-6.8	-7178 ± 18	7780 ± 26	-20132 ± 17	520 ± 4	-342 ± 5	-2608 ± 2
-7.0	-9259 ± 22	9102 ± 32	-24009 ± 24	666 ± 9	-449 ± 7	-3068 ± 2
-7.2	-11510 ± 145	10501 ± 103	-28562 ± 31	798 ± 21	-578 ± 10	-3590 ± 3
-7.4	-14797 ± 40	12188 ± 79	-33681 ± 37	907 ± 30	-732 ± 11	-4184 ± 3
-7.6	-18454 ± 56	14087 ± 59	-39542 ± 49	1016 ± 15	-923 ± 14	-4847 ± 4
-7.8	-22856 ± 64	16098 ± 81	-46281 ± 63	1158 ± 19	-1139 ± 18	-5584 ± 5
-8.0	-28024 ± 102	18350 ± 116	-53836 ± 78	1275 ± 25	-1416 ± 22	-6384 ± 7

Table 5.10: C functions for the four-jet rate from DEBRECEN at different values of y_{cut}. Bins from -0.2 to -1.8 are not tabulated because no event was found to be a four-jet event for those values of y_{cut}. The values for bins with $\ln(y_{cut})$ smaller than -8 are not in the table as we are not interested in the four-jet rate at too small y_{cut} values.

Another approach is tested for the correction of the angular correlations. A detector level distribution is obtained by passing through the detector simulation events simulated with the PYTHIA four-parton option, including ISR and FSR. This MC simulation was expected to describe the data better. This was indeed found for $\cos\alpha_{34}$, but surprisingly not for $\cos\theta_{NR}$ as shown in Fig. 5.1. This may be a hint of some problems in the tuning or in the showering and hadronization processes implemented in PYTHIA. In this analysis,

this new MC simulation has been used to calculate again C^{det} factors, but only for $\cos\alpha_{34}$, were an improvement has been observed.

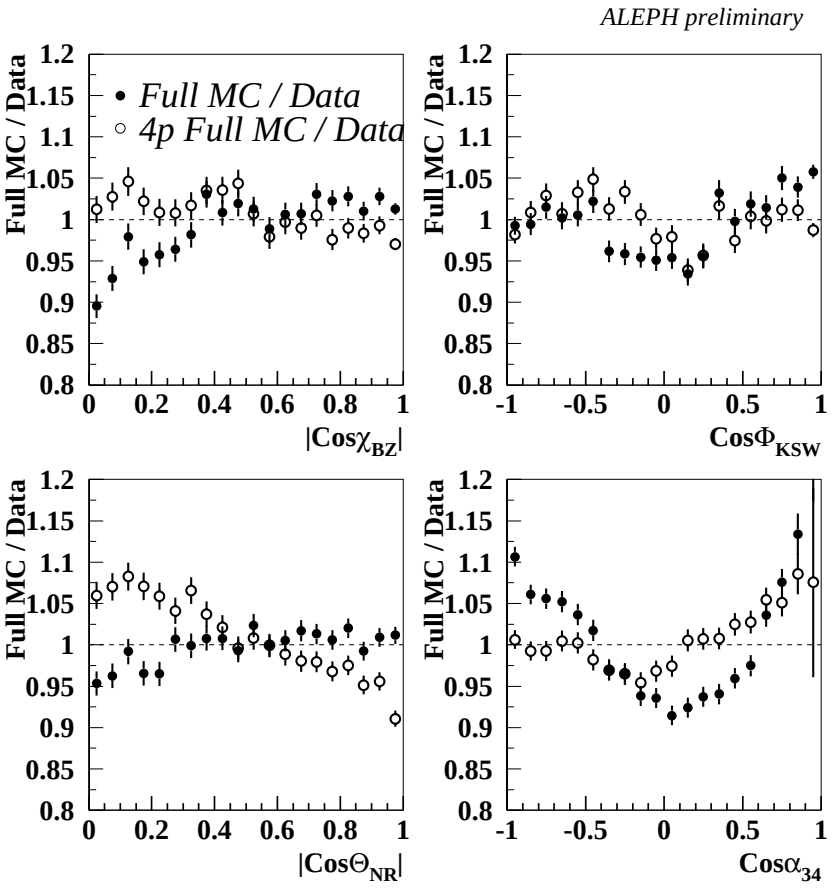

Figure 5.1: Comparison of the two sets of full MC simulations with respect to ALEPH data.

5.4 The fit procedure

The measured distributions for the four-jet angular correlations and the four-jet rate are put together to form a vector

$$D_{1\ldots140} = (\cos\chi_{\mathrm{BZ}\,1\ldots20}, \cos\phi_{\mathrm{KSW}\,1\ldots20}, \cos\theta_{\mathrm{NR}\,1\ldots20}, \cos\alpha_{34\,1\ldots20}, R_{4\,1\ldots60}). \tag{5.10}$$

A covariance matrix σ_{ij}^{D} is calculated from data distributions to take into account the statistical error, correlations between bins of a single distribution, and correlations between

bins of different distributions. The diagonal block elements are the covariance matrices of the single distributions. For the four-jet angular correlations they are multinomial, i.e.

$$\begin{aligned}(\sigma_{ij}^D)_{i,j\in\text{same angle}} &= -p_i p_j \frac{1}{N_{\text{had}}} \\ (\sigma_{ii}^D) &= p_i \left(\frac{1}{\Delta} - p_i\right) \frac{1}{N_{\text{had}}}\end{aligned} \tag{5.11}$$

where $p_i = N_i/N_{\text{had}}\Delta$ with N_i the number of entries in a single bin, N_{had} the total number of hadronic events and Δ the bin width. For the four-jet rate, being a different observable at each y_{cut} value, the formulas to be used are the ones of the off-diagonal block elements,

$$(\sigma_{ij}^D)_{i,j\in\text{diff. dist.}} = ((pp)_{ij} - p_i p_j)\,\frac{1}{N_{\text{had}}} \tag{5.12}$$

where $(pp)_{ij} = N_{ij}/\left(N_{\text{had}}\Delta^2\right)$ with N_{ij} the number of events common to bin i of one distribution and bin j of another.

Then a further vector is formed, $T_{1\ldots140}$, with the theoretical distributions corrected to detector level, having the same dimension as the data vector. With all these inputs, the following function is computed and minimized with respect to the fitted parameters:

$$\chi^2 = \sum_{i,j\in\text{fit range}} \delta_i \sigma_{ij}^{-1} \delta_j \quad , \quad \delta_i = D_i - T_i \quad , \quad \sigma_{ij} = \sigma_{ij}^D + \sigma_{ij}^T. \tag{5.13}$$

5.5 Systematic Uncertainty Studies

Systematic uncertainties can arise from imperfections of the implementation of the physics processes in the MC as well as from deficiencies in the description of the detector performance, from theoretical uncertainties or missing higher orders in the perturbative series, from the model used to calculate the hadronization corrections, and from the specific analysis procedure. The sources of systematic uncertainty that have been taken into account are: the fit range, the selection cuts, the hadronization and background corrections, the detector corrections, the scale uncertainty and the mass effects in the four-jet angular correlations.

In general a Bayesian method is used [21, 44] in order to obtain the systematic error for each source, except for the variation of the fit range, where the number of fitted bins is different. This scheme tries to reduce the arbitrariness of the estimation of the total systematic error: how many and which variations have to be applied in the analyses and the weight that each source should have in the calculation of the final systematic error.

The main decision criterion for the weight in this thesis is the quality of the fit when using a particular analysis chain, i.e. the overall χ^2. The Bayesian idea is that *a priori* all models can be considered equally well suited for usage in the analysis, but from a bad χ^2 it is deduced that the *a posteriori* probability of such model is low, and therefore this model should get a small weight when estimating the actual systematic error. From classical statistics it is known that in the large sample limit a deviation from the estimator of a parameter by N times its variance corresponds to an increase in χ^2 of N^2. This will be the basis for the definition of the size of the systematic error.

For example, a measurement of two quantities (x, y) results in a set of numbers (x_0, y_0, χ_0^2), (x_1, y_1, χ_1^2), ..., (x_n, y_n, χ_n^2) after $(n+1)$ variations of the analysis procedure, with $\chi_0^2 = \min_{i=0,n}\chi_i^2$. First a correlation coefficient for the systematic errors is calculated according to

$$\rho_{x,y}^{\text{syst}} = \frac{\sum_{i=1}^{n}(x_0 - x_i)(y_0 - y_i)}{\sqrt{\left(\sum_{i=1}^{n}(x_0 - x_i)^2\right)\left(\sum_{i=1}^{n}(y_0 - y_i)^2\right)}} \quad . \tag{5.14}$$

Then the elements of the systematic covariance matrix are defined as

$$\sqrt{\sigma_{x,x}^{\text{syst}}} = C \max_{i=1,n}\left(\frac{\Delta x_i}{\sqrt{\Delta\chi^2}}\right) \quad , \quad \sigma_{x,y}^{\text{syst}} = \rho_{x,y}^{\text{syst}}\sqrt{\sigma_{x,x}^{\text{syst}}}\sqrt{\sigma_{y,y}^{\text{syst}}} \, , \tag{5.15}$$

with

$$\Delta x_i = |x_0 - x_i| \quad , \quad \Delta\chi^2 = \max(1, |\chi_0^2 - \chi_i^2|) \quad , \quad C = \max\left(1, \sqrt{\chi_0^2/N_{\text{dof}}}\right) . \tag{5.16}$$

The factor C takes into account cases where the best fit gives a bad χ^2. This scheme is generalizable to any number of fit variables, and it is ensured that models giving a bad fit are properly deweighted. Of course still some unavoidable arbitrariness remains in the choice and number of variations.

$\ln(y_{cut})$	$B_4(y_{cut})$	$C_4(y_{cut})$
-2.0	0.000502 ± 0.000007	0.0136 ± 0.004
-2.2	0.01247 ± 0.00004	0.33 ± 0.01
-2.4	0.0820 ± 0.0001	2.15 ± 0.02
-2.6	0.2981 ± 0.0002	7.89 ± 0.05
-2.8	0.7741 ± 0.0004	20.64 ± 0.08
-3.0	1.6532 ± 0.0006	44.6 ± 0.3
-3.2	3.0924 ± 0.0009	83.0 ± 0.2
-3.4	5.272 ± 0.001	142.1 ± 0.4
-3.6	8.409 ± 0.002	226.1 ± 0.5
-3.8	12.717 ± 0.003	341.3 ± 0.6
-4.0	18.450 ± 0.004	490 ± 1
-4.2	25.911 ± 0.006	680 ± 2
-4.4	35.377 ± 0.007	910 ± 2
-4.6	47.15 ± 0.01	1181 ± 3
-4.8	61.62 ± 0.01	1503 ± 3
-5.0	79.15 ± 0.02	1870 ± 5
-5.2	100.13 ± 0.02	2270 ± 5
-5.4	125.04 ± 0.03	2700 ± 10
-5.6	154.20 ± 0.04	3161 ± 9
-5.8	188.37 ± 0.05	3596 ± 15
-6.0	227.90 ± 0.07	4049 ± 16
-6.2	273.39 ± 0.09	4435 ± 22
-6.4	325.5 ± 0.1	4763 ± 24
-6.6	384.1 ± 0.2	4915 ± 36
-6.8	451.1 ± 0.2	4757 ± 243
-7.0	525.1 ± 0.2	4784 ± 58
-7.2	607.5 ± 0.3	4456 ± 86
-7.4	700.2 ± 0.4	3384 ± 100
-7.6	803.1 ± 0.5	2097 ± 107
-7.8	919.4 ± 0.6	128 ± 152
-8.0	1045.9 ± 0.8	-2562 ± 246

Table 5.11: B and C functions for the four-jet rate from DEBRECEN at different values of y_{cut}. Here the contributions from different columns in tables 5.9 and 5.10 have been added taking the $SU(3)$ values for the colour factor ratios. Bins from -0.2 to -1.8 are not in the table because no event was found to be a four-jet event for those values of y_{cut}. The values for bins with $\ln(y_{cut})$ smaller than -8 are not in the table as we are not interested in the four-jet rate at too small y_{cut} values.

Chapter 6

Measurements of the Strong Coupling Constant and the Colour Factors

Háblame toda la noche si me quieres convencer.
Un rato, una hora, un día. Un tiempo sin determinar.
Tarda una vida en contarme lo que me quieras contar.

In this chapter the measurements of the strong coupling constant, $\alpha_s(M_Z)$, from the four-jet rate, as well as the simultaneous measurement of the strong coupling constant and the colour factors are described. The structure of the chapter is as follows. First the α_s measurements from the four-jet rate are detailed. Three different methods have been employed giving results in perfect agreement among them, and with an important reduction in the total systematic error with respect to previous analyses based on two- and three-jet observables. Finally, the simultaneous measurement of the strong coupling and the colour factors is presented, with results in perfect agreement with previous ALEPH analyses and with a similar analysis from another LEP Collaboration, namely OPAL.

6.1 Measurements of the Strong Coupling Constant from the Four-Jet Rate

Many QCD studies have been carried out at LEP, in particular precise measurements of the strong coupling constant $\alpha_s(M_Z)$ [9]. For these measurements jet rates and so called event-shape variables have been used as they are very sensitive to the effects of gluon radiation, and usually defined such that the differential cross sections are directly

proportional to the strong coupling constant. The differential matrix elements in leading (LO) and next-to-leading order (NLO) for these two- and three-jet type quantities have been known for a long time [15], and for some of the variables even the resummation of large logarithms to all orders in perturbation theory has been carried out [45].

Some years ago, NLO corrections to infrared- and collinear-safe four-jet observables were computed [46, 47, 48, 50, 51, 52, 53, 24], which allow refined studies such as measurements of the strong coupling constant with variables for which the perturbative predictions start at $\mathcal{O}(\alpha_s^2)$.

In this section three α_s measurements are presented which use these new calculations. The resummed next-to-leading order predictions for the four-jet rate, corrected to detector level, are fitted to ALEPH data. The theoretical input as well as the analysis procedure have been described in Chapters 3 and 5, respectively. Here plots and details about the corrections, the fit range, systematic uncertainty studies and a discussion of the results are given.

6.1.1 Corrections for the Four-Jet Rate

Hadronization Corrections

The resummed theoretical NLO prediction as obtained from DEBRECEN should be corrected for hadronization effects. This, as explained in the previous chapter, is done by computing the ratio of the hadron and parton level distributions.

In Fig. 6.1 the bin-by-bin hadronization corrections calculated with the various models described in Section 5.3.1 are shown. The two parton shower models PYTHIA and HERWIG give very similar corrections, which differ appreciably from unity, by about 20%. The corrections obtained with the PYTHIA,ME and PYTHIA,Q_0 options typically differ more from unity and are quite different from the previous ones. The large discrepancies at the order of 10% can be traced back to large discrepancies in the four-jet rates at parton and at hadron level. The parton shower option, for y_{cut}=0.008, gives a four-jet rate of 8.2% (6.9%) at parton (hadron) level, whereas the matrix element option predicts 10.2% (7.7%).

New MC models where the matrix element approach is combined with a parton shower have been studied, but they have been shown not to be suitable for the description of the

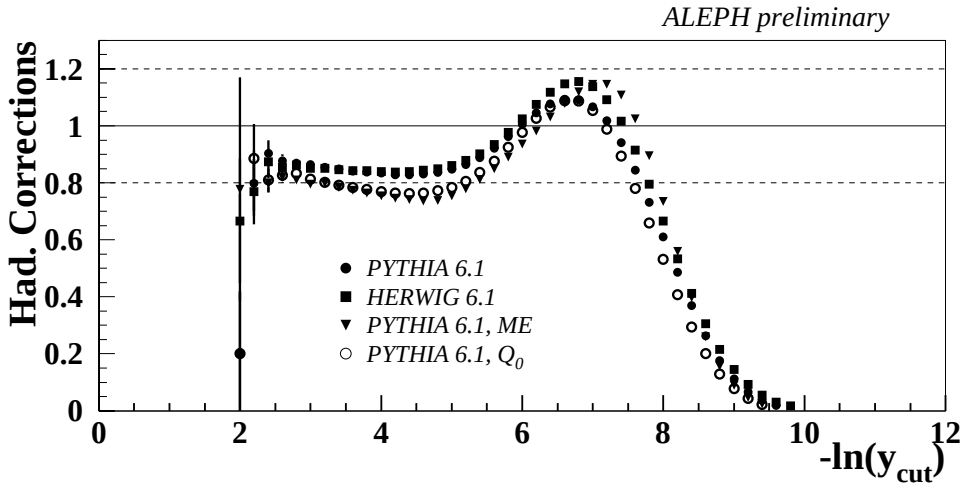

Figure 6.1: Comparison of the different hadronization corrections used in this thesis.

four-jet rate, as their predictions depend on an intrinsic resolution parameter needed to avoid soft and collinear divergences [43] (see also Chapter 7).

Detector Corrections

The theoretical prediction for the four-jet rate already corrected for hadronization effects, has to be corrected further to include detector effects before being compared to ALEPH data. As explained in the previous chapter, this is done by computing this observable from the MC before and after detector simulation.

The detector correction factors for the four-jet rate are typically found within the 5-10% range, increasing at the edges of the phase space. These corrections are displayed in Fig. 6.2.

Total Corrections

Taking into account the hadronization and detector corrections as explained above, the total corrections for the four-jet rate can be constructed as:

$$C^{\mathrm{tot}}(\mathrm{y_{cut}}) = C^{\mathrm{had}}(\mathrm{y_{cut}}) \cdot C^{\mathrm{det}}(\mathrm{y_{cut}})\,. \tag{6.1}$$

Figure 6.3 shows the total bin-by-bin corrections. Typically they are about 10% in the central region of the four-jet rate, but quickly increasing to around 20% or higher when

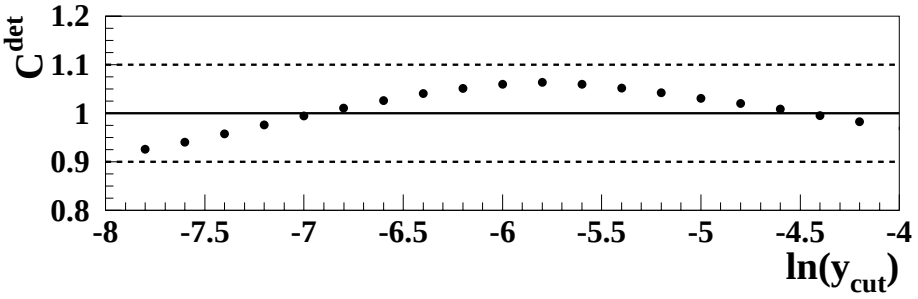

Figure 6.2: Detector corrections for the four-jet rate.

going to small or large y_{cut} values. Taking into account these total corrections, the fit range is selected by requiring them to be smaller than 10% and the resolution parameter to be in the range $10^{-3} < y_{cut} < 10^{-2}$.

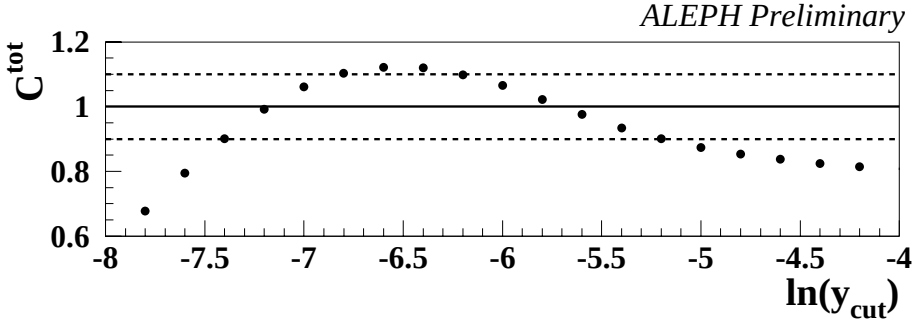

Figure 6.3: Total corrections for the four-jet rate. The dashed lines show the maximum allowed corrections used for the fit

6.1.2 Results

The experimental covariance matrix is calculated to take into account the statistical error of the data, the statistical errors of the detector and hadronization corrections, the statistical error of the theoretical prediction and the bin-by-bin statistical correlations among measurements of R_4 at different values of the resolution parameter. This covariance matrix is calculated following Eq. 5.12. Table 6.1 contains the four-jet rate from ALEPH data as well as the detector corrections. In Fig. 6.4 the correlations for the four-jet rate are plotted, showing values up to 90% for neighbouring y_{cut} values.

$\ln(y_{cut})$	R_4 from ALEPH data	Detector Corrections
-2.2	0.000019 ± 0.000003	0.7932 ± 0.1424
-2.4	0.000089 ± 0.000006	0.7307 ± 0.0481
-2.6	0.000315 ± 0.000012	0.8768 ± 0.0267
-2.8	0.000801 ± 0.000019	0.9054 ± 0.0164
-3.0	0.001699 ± 0.000027	0.9215 ± 0.0112
-3.2	0.003317 ± 0.000038	0.9276 ± 0.0082
-3.4	0.005744 ± 0.000050	0.9382 ± 0.0062
-3.6	0.009197 ± 0.000063	0.9494 ± 0.0050
-3.8	0.013923 ± 0.000078	0.9582 ± 0.0040
-4.0	0.020152 ± 0.000093	0.9683 ± 0.0034
-4.2	0.028218 ± 0.000110	0.9824 ± 0.0029
-4.4	0.038261 ± 0.000127	0.9945 ± 0.0025
-4.6	0.050409 ± 0.000145	1.0087 ± 0.0022
-4.8	0.064992 ± 0.000163	1.0197 ± 0.0019
-5.0	0.082198 ± 0.000182	1.0304 ± 0.0017
-5.2	0.102317 ± 0.000201	1.0422 ± 0.0015
-5.4	0.125528 ± 0.000220	1.0518 ± 0.0014
-5.6	0.151787 ± 0.000238	1.0597 ± 0.0012
-5.8	0.180738 ± 0.000255	1.0632 ± 0.0011
-6.0	0.210446 ± 0.000270	1.0596 ± 0.0010
-6.2	0.239597 ± 0.000283	1.0505 ± 0.0009
-6.4	0.265663 ± 0.000293	1.0401 ± 0.0008
-6.6	0.285690 ± 0.000299	1.0260 ± 0.0008
-6.8	0.297560 ± 0.000303	1.0100 ± 0.0007
-7.0	0.298678 ± 0.000303	0.9937 ± 0.0007
-7.2	0.287528 ± 0.000300	0.9753 ± 0.0007
-7.4	0.265248 ± 0.000293	0.9572 ± 0.0008
-7.6	0.234053 ± 0.000281	0.9405 ± 0.0008
-7.8	0.196958 ± 0.000264	0.9255 ± 0.0009
-8.0	0.157385 ± 0.000241	0.9134 ± 0.0010

Table 6.1: Four-jet rate measurements at different values of y_{cut} from ALEPH data. The detector corrections are also given. Bins from -0.2 to -2.0 are not in the table because no event was found to be a four-jet event for those values of y_{cut}.

Then a χ^2 is constructed according to Eq. 5.13, where i and j run over the bins allowed by the fit range requirements. Three different minimizations of this χ^2 are carried out,

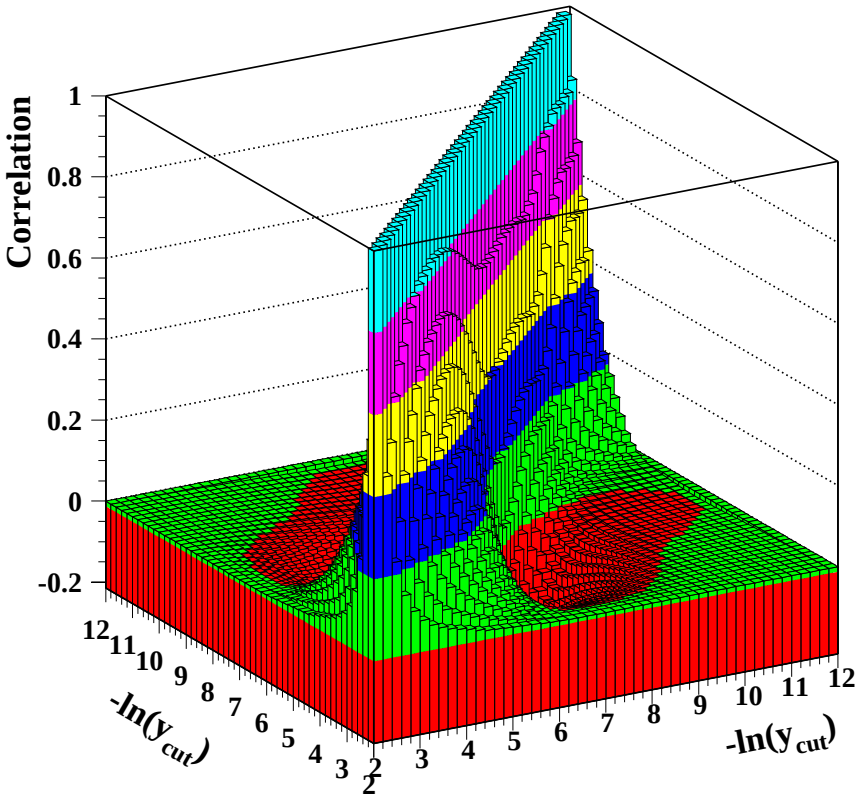

Figure 6.4: Bin-by-bin statistical correlations between measurements of the four-jet rate at different y_{cut} values.

leading to three different measurements of the strong coupling constant.

- **Method I**. The minimization is performed with respect to $\eta = \frac{\alpha_s C_F}{2\pi}$, with x_μ fixed to 1. Later, all the systematic uncertainty estimations will be for $x_\mu = 1$. The scale uncertainty will be estimated as the variation in the fitted η when x_μ is varied in the range $0.5 < x_\mu < 2$..

- **Method II**. The minimization is performed with respect to η and x_μ. In all the systematic uncertainty estimations both parameters will be fitted again. There is no theoretical uncertainty associated to the scale, as it is a fitted parameter.

- **Method III**. The minimization is first performed with respect to both η and x_μ. The fitted x_μ value is taken as the optimized scale, ${x_\mu}^{\rm opt}$ [1]. Then, all the systematic

[1] Some details and discussion about the optimized scale method can be found in Appendix A

uncertainty estimations are calculated by fitting only η, but with the scale fixed to this optimized value. The scale uncertainty will be estimated by the variation in the fitted η when x_μ is moved in the range $0.5{x_\mu}^{\rm opt} < x_\mu < 2{x_\mu}^{\rm opt}$.

The fit results for the three methods can be found in Tables 6.2 - 6.4, and the plots of the fit results in Figs. 6.5 and 6.6. The new calculations used for this study, which are at NLO for a four-jet observable, are an important ingredient for a future full NNLO prediction for three-jet observables, where a value for x_μ closer to unity might be obtained [24].

$\eta(\mathrm{M_Z})$	x_μ	$\chi^2/N_{\rm dof}$	$\Longrightarrow$	$\alpha_s(\mathrm{M_Z})$
0.02483 ± 0.00003	1.	27.6/5		0.1170 ± 0.0001

Table 6.2: Fit results with statistical errors only for Method I using ALEPH data.

$\eta(\mathrm{M_Z})$	x_μ	$\chi^2/N_{\rm dof}$	$\Longrightarrow$	$\alpha_s(\mathrm{M_Z})$
0.02494 ± 0.00004	0.73 ± 0.05	4.8/4		0.1175 ± 0.0002

Table 6.3: Fit results with statistical errors only for Method II using ALEPH data.

$\eta(\mathrm{M_Z})$	x_μ	$\chi^2/N_{\rm dof}$	$\Longrightarrow$	$\alpha_s(\mathrm{M_Z})$
0.02494 ± 0.00003	0.73	4.8/5		0.1175 ± 0.0001

Table 6.4: Fit results with statistical errors only for Method III using ALEPH data.

A χ^2 per degree of freedom close to unity is found for methods II and III, where a "preferred" value x_μ=0.73 is found. The fitted x_μ in Method II, quite different from unity, might be an indication that missing higher orders in perturbative QCD are still important. This is also reflected in the large χ^2 for Method I, where the scale is not allowed to vary and thus to mimic the contributions from missing higher orders.

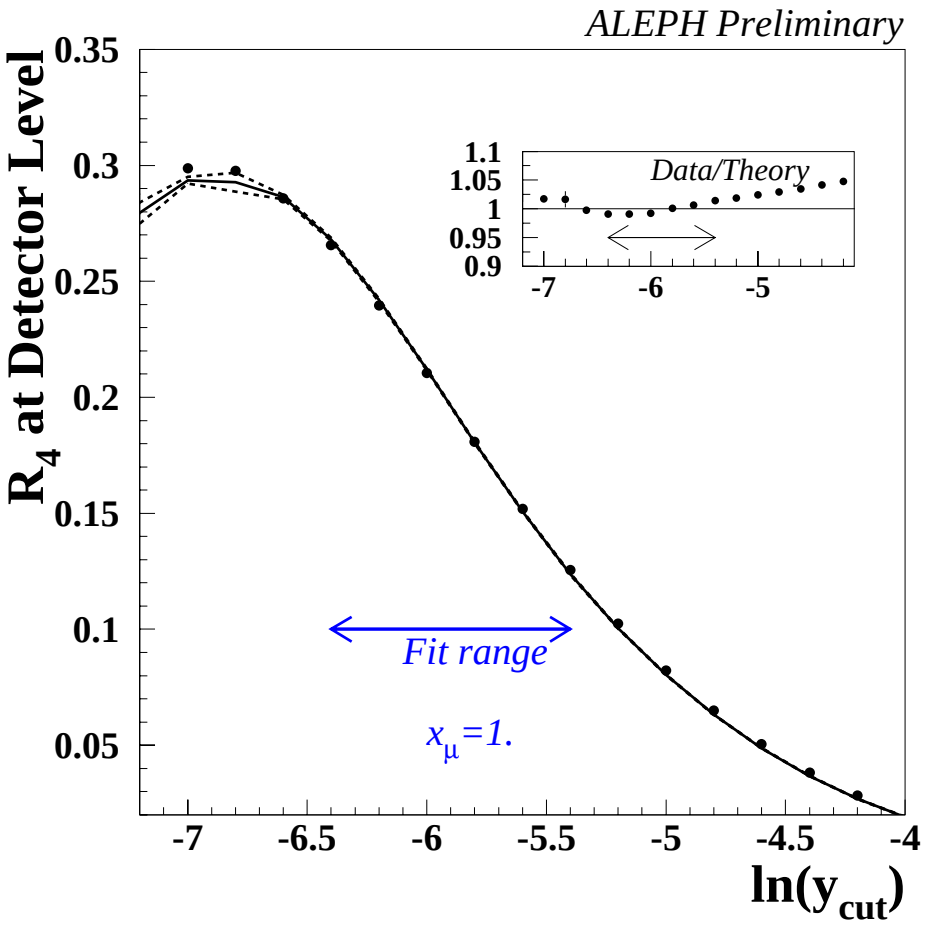

Figure 6.5: Plot for the distribution of the four-jet rate, corrected to detector level and fitted to ALEPH data using Method I. Full dots correspond to ALEPH data and the solid line to the fitted distribution. Dashed lines are also plotted, which correspond to the statistical uncertainty, but they are indistinguishable from the solid line for most of the y_{cut} range. The ratio of data with respect to fitted distributions is shown in the small insert.

Figures 6.5 and 6.5 shows how the fitted four-jet rate significantly deviates from data for low values of $\ln y_{cut}$ out of the fit range. Such deviation is larger when the scale is also fitted, which could be an indication of missing higher orders being more and more important at small y_{cut} values.

Finally, Fig. 6.7 shows the sensitivity of the fit to the renormalization scale, leading to a theoretical uncertainty on η from the scale variation.

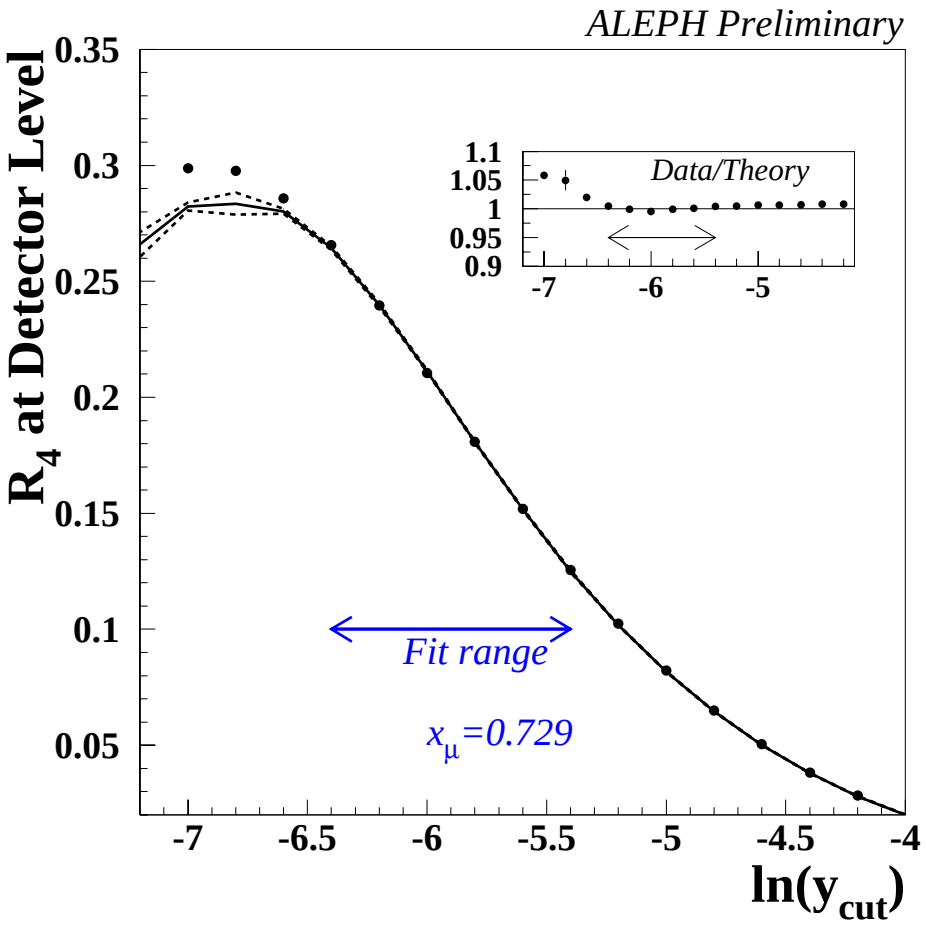

Figure 6.6: Plot for the distribution of the four-jet rate, corrected to detector level and fitted to ALEPH data using Method II. Full dots correspond to ALEPH data and the solid line to the fitted distribution. Again dashed lines are plotted to show the statistical uncertainty, but they are indistinguishable from the solid line for most of the y_{cut} range. The ratio of data with respect to fitted distributions is shown in the small insert.

6.1.3 Systematic Studies

Quedaba mucho por hacer.
Quedaba mucho.
Aprendí a sumar lo lógico y lo incierto.

Tables 6.5-6.7 show the sources of systematic uncertainty that have been studied for the three methods. A brief description of each uncertainty source can be found in the following sections.

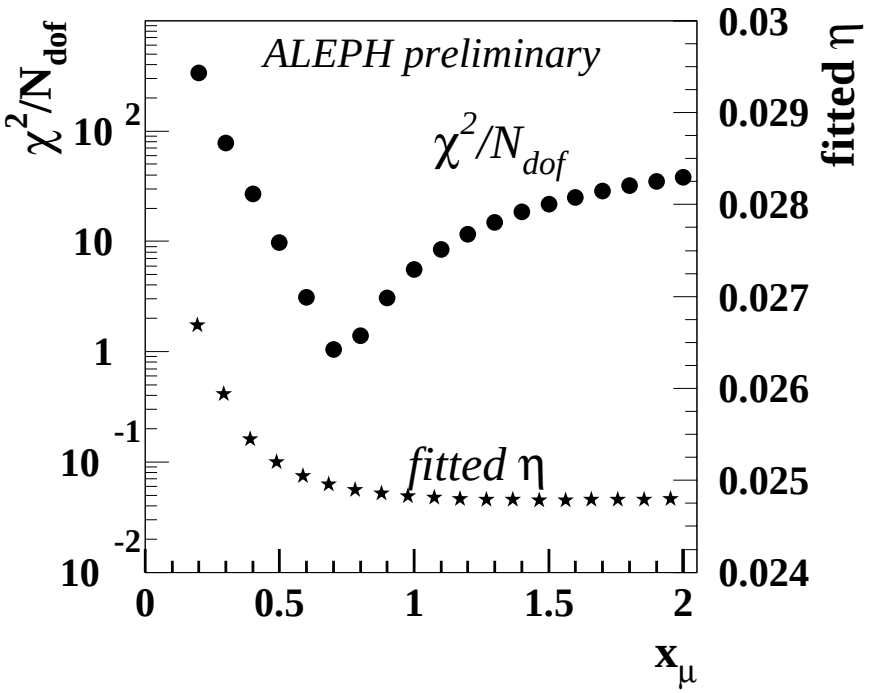

Figure 6.7: Dependence of the fitted η value and the $\chi^2/N_{\rm dof}$ on the renormalization scale x_μ.

Fit Range

The sensitivity of the measurements to the fit range is checked by repeating the analyses with the requirement of a total correction per bin smaller than 20% (it was 10% in the standard analyses). The systematic variation due to this new fit range is quite different for the three methods. For the first method, where x_μ is fixed to 1, the range uncertainty is large with respect to the statistical error. However, for the two other methods this uncertainty is of the same order than the statistical one. This might be an indication of some correlation between the scale and range uncertainties in Method I, which is avoided when x_μ is either fit at the same time as η or fixed to its optimized value.

Selection Criteria

All cuts imposed in the hadronic selection have been varied in order to evaluate the effect on the measurement. The new values for the selection cuts on track parameters are found by changing them until the number of selected events per unit luminosity is the same in data and MC [54]. The analysis has been repeated by introducing the following changes

	$\eta(M_Z)$	χ^2/N_{dof}
tot.corr. $< 20\%$	0.02491 ± 0.00002	57.5/8
Range sys.	$\Delta\eta = 0.00008$	

	$\eta(M_Z)$	χ^2/N_{dof}
HERWIG	0.02461 ± 0.00003	107.3/5
Hadr. Syst.	$\Delta\eta = 0.00006$	

	$\eta(M_Z)$	χ^2/N_{dof}
Charged Only	0.02500 ± 0.00003	33.6/5
Detector sys.	$\Delta\eta = 0.00016$	

	$\eta(M_Z)$	χ^2/N_{dof}
x_μ=0.5	0.02519 ± 0.00003	50.0/5
x_μ=2.	0.02480 ± 0.00002	195.3/5
Scale sys.	$\Delta\eta = 0.00018$	

	$\eta(M_Z)$	χ^2/N_{dof}
Sphericity cut	0.02485 ± 0.00003	29.3/5
TPC cut	0.02480 ± 0.00003	22.2/5
N_{ch} cut	0.02486 ± 0.00003	27.6/5
E_{ch} cut	0.02484 ± 0.00003	28.5/5
θ_{ch} cut	0.02485 ± 0.00003	34.6/5
θ_{nt} cut	0.02479 ± 0.00003	28/2/5
Fraction of e.m. energy cut	0.02483 ± 0.00003	27.1/5
z_0 cut	0.02482 ± 0.00003	28.3/5
d_0 cut	0.02483 ± 0.00003	27.9/5
p_t cut	0.02482 ± 0.00003	26.4/5
Experimental sys.	$\Delta\eta = 0.00013$	

Table 6.5: Systematic uncertainties for Method I.

(only one at a time): at least six measured space coordinates from the TPC; a polar angle at the origin in the range $20° < \theta < 160°$ both for charged and neutral tracks; transverse momentum $p_t > 0.205$ GeV/c; $d_0 = 1.867$cm; $z_0 = 6.64$cm; at least 8 selected charged tracks; minimum charged energy 22 GeV; $|\cos\Theta_{Sph}| < 0.85$; and fraction of electromagnetic energy $< 20\%$.

The observed changes when modifying the selection cuts are in general small and in many cases even negligible, always below 1% for η. These uncertainties are smaller than the equivalent ones obtained with three-jet observables, as might be expected from the quadratic LO dependence on η for four-jet variables instead of the linear one in the case of three-jet variables.

	$\eta(\mathrm{M_Z})$	x_μ	χ^2/N_{dof}	
tot.corr. $< 20\%$	0.02496 ± 0.00003	0.756 ± 0.034	20.3/7	$\rho_\eta x_\mu$
Range sys.	$\Delta\eta = 0.00002$	$\Delta x_\mu = 0.027$		1.

	$\eta(\mathrm{M_Z})$	x_μ	χ^2/N_{dof}	
HERWIG	0.02491 ± 0.00005	0.547 ± 0.029	0.7/4	$\rho_\eta x_\mu$
Hadr. Syst.	$\Delta\eta = 0.00002$	Δx_μ=0.099		1.

	$\eta(\mathrm{M_Z})$	x_μ	χ^2/N_{dof}	
Charged Only	0.02511 ± 0.00004	0.731 ± 0.046	9.1/4	$\rho_\eta x_\mu$
Detector sys.	$\Delta\eta = 0.00009$	$\Delta x_\mu = 0.001$		1.

	$\eta(\mathrm{M_Z})$	x_μ	χ^2/N_{dof}	
Sphericity cut	0.02497 ± 0.00004	0.719 ± 0.047	4.4/4	
TPC cut	0.02489 ± 0.00004	0.750 ± 0.050	4.0/4	
N_{ch} cut	0.02497 ± 0.00004	0.731 ± 0.047	5.1/4	
E_{ch} cut	0.02495 ± 0.00004	0.725 ± 0.047	4.7/4	
θ_{ch} cut	0.02498 ± 0.00004	0.703 ± 0.044	4.9/4	
θ_{nt} cut	0.02490 ± 0.00004	0.728 ± 0.048	5.5/4	
Fraction of e.m. energy cut	0.02494 ± 0.00004	0.732 ± 0.048	4.9/4	
z_0 cut	0.02493 ± 0.00004	0.726 ± 0.047	4.8/4	
d_0 cut	0.02494 ± 0.00004	0.727 ± 0.047	4.8/4	
p_t cut	0.02493 ± 0.00004	0.732 ± 0.048	4.5/4	$\rho_\eta x_\mu$
Experimental sys.	$\Delta\eta = 0.00010$	$\Delta x_\mu = 0.039$		-0.741

Table 6.6: Systematic uncertainties for Method II.

The total experimental systematic uncertainty has been computed as the quadratic sum of all contributions, where individual contributions are calculated in the Bayesian approach. It results in an experimental uncertainty on η going from 0.00013 for Method I to 0.00008 for Method III.

Hadronization Corrections

The hadronization correction uncertainty is taken as the Bayesian change in η when the corrections are calculated with HERWIG. This results in a systematic uncertainty much

	$\eta(M_Z)$	χ^2/N_{dof}
tot.corr. $< 20\%$	0.02497 ± 0.00003	20.1/8
Range sys.	$\Delta\eta = 0.00003$	

	$\eta(M_Z)$	χ^2/N_{dof}
HERWIG	0.02473 ± 0.00003	27.9/5
Hadr. Syst.	$\Delta\eta = 0.00004$	

	$\eta(M_Z)$	χ^2/N_{dof}
Charged Only	0.02511 ± 0.00003	9.1/5
Detector sys.	$\Delta\eta = 0.00008$	

	$\eta(M_Z)$	χ^2/N_{dof}
x_μ=0.365	0.02559 ± 0.00004	193.3/5
x_μ=1.458	0.02479 ± 0.00003	101.8/5
Scale sys.	$\Delta\eta = 0.00005$	

	$\eta(M_Z)$	χ^2/N_{dof}
Sphericity cut	0.02496 ± 0.00003	4.4/5
TPC cut	0.02490 ± 0.00003	4.2/5
N_{ch} cut	0.02497 ± 0.00003	5.1/5
E_{ch} cut	0.02494 ± 0.00003	4.7/5
θ_{ch} cut	0.02496 ± 0.00003	5.2/5
θ_{nt} cut	0.02490 ± 0.00003	5.5/5
Fraction of e.m. energy cut	0.02494 ± 0.00003	4.9/5
z_0 cut	0.02490 ± 0.00003	5.5/5
d_0 cut	0.02494 ± 0.00003	4.8/5
p_t cut	0.02493 ± 0.00003	4.6/6
Experimental sys.	$\Delta\eta = 0.00008$	

Table 6.7: Systematic uncertainties for Method III.

smaller than 1% for the three methods. In methods I and III, the χ^2 of the fit when using HERWIG corrections is almost four times the one of the standard measurement. Therefore, the uncertainty calculated using the Bayesian method is heavily reduced if compared to the full difference between the fit results of measurements using PYTHIA and HERWIG corrections. However, even if the full difference is taken as an estimate of the hadronization uncertainty, it would be small (0.00022), not even reaching the 1% range.

Detector Corrections

An estimation of the systematic uncertainty due to the detector corrections has been obtained by repeating the analysis using charged tracks only, leading to a variation in η

going from 0.6% to 0.3%, depending on the method.

Theoretical Predictions

The lack of knowledge of higher orders of perturbative QCD is estimated by the impact on η of the renormalization scale variation for Methods I and III. In the second Method there is no uncertainty related to the scale as it is fitted for each variation of the analysis.

The scale uncertainty is the largest contribution to the total systematic uncertainty in the case of Method I as can be seen in Table 6.5. For Method III, this uncertainty is heavily reduced to less than 1/3 of its value in the first case. This is a well known feature of the optimized scale method as is further explained in Appendix A.

6.1.4 Further Checks

Hadronization Corrections

As a cross-check, the more extreme models presented in Sect. 5.3.1 were used to fit η. The systematic changes in the fitted parameters, see Table 6.8, are covered by the total uncertainty as will be seen in Section 6.1.5.

	$\eta(\mathrm{M_Z})$	x_μ	χ^2/N_{dof}
PYTHIA ME - Method I	0.02569 ± 0.00003	1.	80.6/5
PYTHIA ME - Method II	0.02589 ± 0.00005	0.637 ± 0.030	3.4/4
PYTHIA ME - Method III	0.02581 ± 0.00003	0.729	11.3/5
PYTHIA,Q_0 - Method I	0.02527 ± 0.00003	1.	178.5/5
PYTHIA,Q_0 - Method II	0.02563 ± 0.00005	0.526 ± 0.023	11.3/4
PYTHIA,Q_0 - Method III	0.02539 ± 0.00003	0.729	60.7/5

Table 6.8: Check for the hadronization corrections. The deviations from the standard analysis are covered by the systematic uncertainties already described.

Scale Dependence when using PYTHIA or HERWIG

In the results for Method III, the fitted scale was found to be quite different when using the hadronization corrections coming from PYTHIA (0.73) or HERWIG (0.55). The check described in this section was carried out in order to understand the source of this

effect. The fit was repeated, for some arbitrarily chosen ranges, both using corrections from PYTHIA and HERWIG. The results can be found in Table 6.9. The discrepancies in the fitted x_μ are found to be larger when going to small values of $\ln(y_{cut})$, where the PYTHIA and HERWIG corrections differ more from each other, see Fig. 6.1. In fact, the first two entries of the table show quite close x_μ values for PYTHIA and HERWIG (compatible within errors), as they correspond to the ranges with very similar corrections. Therefore, the different fitted x_μs obtained in the fits when using PYTHIA and HERWIG corrections are just a propagation of the discrepancies of the hadronization corrections themselves and are then covered by the hadronization + range uncertainties. In any case, the variations in the fitted η, within one type of corrections, are small (especially for the PYTHIA case).

	PYTHIA		HERWIG	
Range	$\eta(M_Z)$	x_μ	$\eta(M_Z)$	x_μ
$-6. \to -4.2$	0.02497	0.66	0.02483	0.61
$-6. \to -5.$	0.02499	0.64	0.02485	0.59
$-6.2 \to -5.2$	0.02498	0.67	0.02488	0.57
$-6.4 \to -5.4$	0.02494	0.73	0.02491	0.55
$-6.6 \to -5.6$	0.02489	0.83	0.02487	0.58
$-6.8 \to -5.8$	0.02496	0.75	0.02485	0.59

Table 6.9: Check for the difference in the optimized scale when using PYTHIA or HERWIG to correct for hadronization effects.

Fits over different ranges of R_4

There is an ongoing discussion with the DELPHI experiment about the meaning of fitting the four-jet rate with x_μ fixed to 1 [56]. The DELPHI Collaboration uses as standard measurement the optimized scale method (i.e. Method III in this analysis) but with the theoretical prediction only at NLO. Such a decision was taken after performing the following test. Small ranges of R_4 at different values of $\ln(y_{cut})$ were fitted to DELPHI data, using resummed predictions, and significantly different η values were found. Such variations in the fitted η brought them to the conclusion that missing higher order terms were important and that the scale should be fitted at the same time. However, they claim that it has no physical meaning to fit the scale when a resummed prediction is used. We have also studied such variations but different conclusions were extracted.

The check is the following. The resummed four-jet rate was fitted at different small ranges covering in total a large region in terms of $\ln(y_{cut})$. The method used for the fit was always Method I. Results can be found in Table 6.10, where $\Delta\eta_{range}$ is calculated as the largest difference between the measurement at a given range and any of the measurements at other ranges. Then, the fit was repeated for the same ranges, but now with x_μ first fixed to 0.5 and then to 2, i.e. the scale uncertainty for each range was obtained. Results for the scale uncertainty estimation are found in Table 6.11. A large correlation between the range uncertainty and the scale uncertainty is observed, which implies that the "bias" in the fitted η which could be introduced by selecting a given range is fully covered by the scale uncertainty in each case, i.e. the fitted η values together with their scale uncertainty for the different ranges are fully compatible.

Range	$\eta(M_Z)$	$\Delta\eta_{range}$
$-5. \to -4.$	0.02511	0.00028
$-5.2 \to -4.2$	0.02508	0.00025
$-5.4 \to -4.4$	0.02506	0.00023
$-5.6 \to -4.6$	0.02501	0.00018
$-5.8 \to -4.8$	0.02497	0.00014
$-6. \to -5.$	0.02492	0.00019
$-6.2 \to -5.2$	0.02488	0.00023
$-6.4 \to -5.4$	0.02483	0.00028

Table 6.10: Variation in the the fitted η when using different ranges for the resummed four-jet rate.

Range	η for x_μ=0.5	η for x_μ=2.	$\Delta\eta_{scale}$
$-5. \to -4.$	0.02494	0.02547	0.00036
$-5.2 \to -4.2.$	0.02497	0.02538	0.00030
$-5.4 \to -4.4$	0.02498	0.02533	0.00027
$-5.6 \to -4.6$	0.02503	0.02520	0.00019
$-5.8 \to -4.8$	0.02506	0.02511	0.00014
$-6. \to -5.$	0.02509	0.02500	0.00017
$-6.2 \to -5.2$	0.02513	0.02491	0.00025
$-6.4 \to -5.4$	0.02520	0.02480	0.00037

Table 6.11: Estimation of the scale uncertainty for different ranges of the four-jet rate.

Another estimation of the scale uncertainty for Method III

If the χ^2 obtained for the experimentally optimized scale method is taken at face value and if this method is used for the standard fit, then the scale uncertainty can be computed as the change in the fitted η when x_μ is fixed to a value ${x_\mu}^{\rm new}$ such that $\chi^2({x_\mu}^{\rm new}) = \chi^2({x_\mu}^{\rm opt}) + 1$. For the fit presented in Section 6.1.2 the optimized scale value was 0.73, and a variation of one in the χ^2 corresponds to the x_μ values of 0.69 and 0.78. The fit results are found in Table 6.12, which give a scale uncertainty of 0.00003 to be compared to 0.00005 obtained with the estimation used in Section 6.1.3.

η	x_μ	$\chi^2/N_{\rm dof}$
0.02497 ± 0.00003	0.69	5.9/4
0.02491 ± 0.00003	0.78	5.9/4

Table 6.12: Estimation of the scale uncertainty for Method III using as criteria a variation of 1 in the χ^2.

Effect of the K coefficient in the resummed prediction

It was stated in Chapter 3 that if the K coefficient was taken into account in the splitting probabilities, an improved theoretical prediction could be obtained. This had been observed for the two-jet rate [26], but it is also true for the four-jet rate as seen in Fig. 6.8. In the figure the improved resummed prediction is shown to better reproduce the ALEPH data. Thus, the resummed prediction without this K coefficient was not taken into account for the measurements of this thesis.

6.1.5 Final Results

Putting together all systematic uncertainties considered above, the final results of the measurements of the strong coupling constant are:

$$\eta(\mathrm{M_Z}) = 0.02483 \pm 0.00003(stat) \pm 0.00029(sys)$$
$$\Downarrow$$
$$\alpha_s(\mathrm{M_Z}) = 0.1170 \pm 0.0001(stat) \pm 0.0014(sys)$$

for Method I,

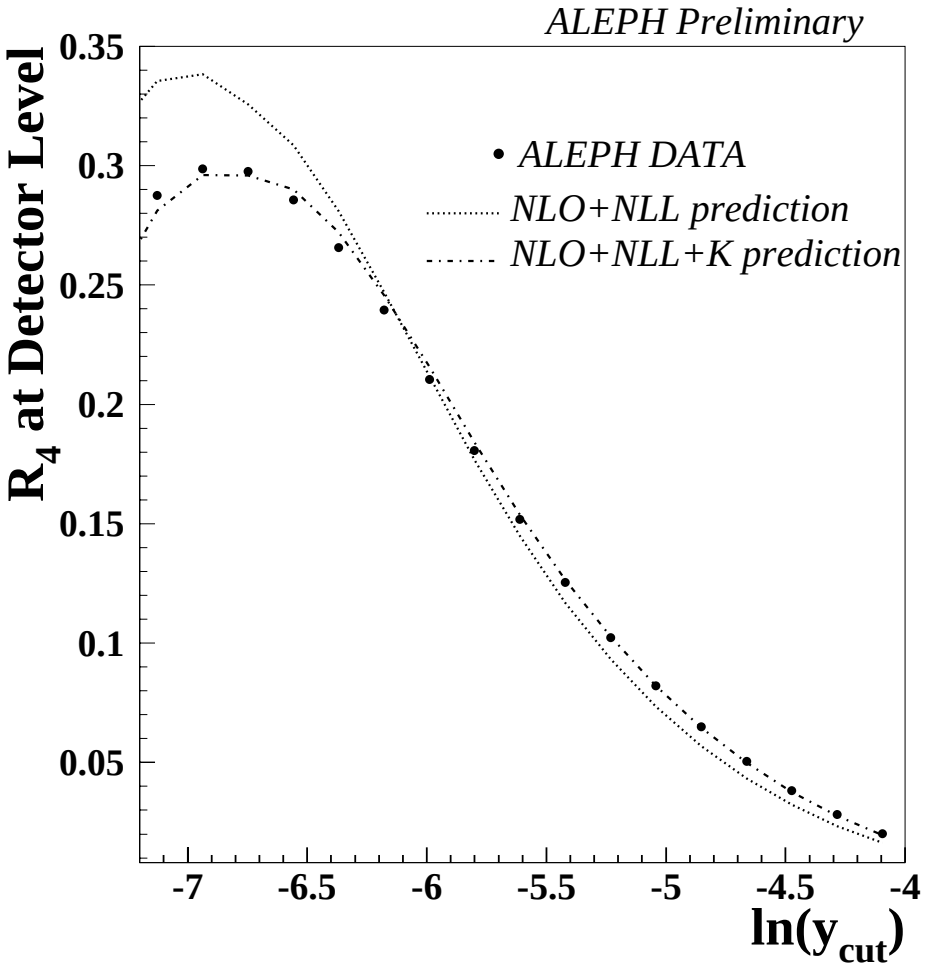

Figure 6.8: Comparison of the four-jet rate as obtained from ALEPH data to the resummed predictions, with and without the K coefficient, from DEBRECEN.

$$\eta(\mathrm{M_Z}) = 0.02494 \pm 0.00004(stat) \pm 0.00013(sys)$$
$$x_\mu = 0.73 \pm 0.05$$
$$\Downarrow$$
$$\alpha_s(\mathrm{M_Z}) = 0.1175 \pm 0.0002(stat) \pm 0.0006(sys)$$

for Method II and, finally for Method III,

$$\eta(\mathrm{M_Z}) = 0.02494 \pm 0.00003(stat) \pm 0.00014(sys)$$
$$\Downarrow$$
$$\alpha_s(\mathrm{M_Z}) = 0.1175 \pm 0.0001(stat) \pm 0.0007(sys) \quad .$$

If the Bayesian method had not been used, and all the contributions for each uncertainty source had been added quadratically instead, the total systematic error in α_s would be of 0.0022, 0.0008 and 0.0033, respectively.

The results presented above are in good agreement with previous measurements by ALEPH using two- and three-jet observables [54], but the dominant source of uncertainty, the theoretical uncertainty, is strongly reduced when using the four-jet rate. Such results are confirmed by a preliminary analysis from the DELPHI collaboration, which also uses the four-jet rate [56]. These results are one of the most precise determinations on α_s at present.

6.2 A Simultaneous Measurement of the Strong Coupling Constant and the Colour Factors

Tests of the structure of the underlying gauge group [21][55], which is $SU(3)$ in the case of QCD, have been performed at LEP. In order to get sensitivity to the gauge structure of the theory, the angular distributions of jets in four-jet events were employed. The first tests of the structure of the underlying gauge group were done using LO predictions which start at $\mathcal{O}(\alpha_s^2)$ [57].

Leading order calculations in pQCD give only the order of magnitude of a partonic cross section and the main features of the distribution of a certain observable. This poor predictivity of the theory is usually signalled by a strong dependence of the (unphysical) renormalization and factorization scales. The theoretical accuracy of pQCD predictions is in general controlled by higher (at least NLO) order corrections that reduce the scale sensitivity.

In this section a new combined measurement of the strong coupling constant and the colour factors using NLO calculations is presented, by fitting the resummed next-to-leading order predictions for the four-jet rate and the normalized next-to-leading order predictions for the angular correlations of the four-jet events to corrected ALEPH data. A new treatment of the backgrounds and hadronization corrections is used, showing good agreement with previous results. In the following subsections details about corrections, fit results and systematic uncertainties are given. Recently, first results on a combined measurement of the strong coupling constant and the colour factors, which are based on NLO calculations, have been published by OPAL [55].

6.2.1 Corrections for the Four-Jet Observables

Background plus Hadronization Corrections

The theoretical NLO prediction as obtained from DEBRECEN should be corrected for background and hadronization effects. The correction procedure was detailed in Section 5.3.1. In Fig. 6.9 the background plus hadronization corrections as obtained from PYTHIA and HERWIG are shown.

The background plus hadronization corrections from the HERWIG simulation show large discrepancies with respect to the ones coming from PYTHIA. The showering and hadronization parameters used, both in HERWIG and PYTHIA, are the standard ones, which were obtained by the tuning of MC simulations starting from $q\bar{q}$ configurations. Therefore this may be an indication of the non-universality of these parameters. If a better tuning cannot be found, then the reason for the discrepancies could be due to the implementation of the showering and hadronization processes in the MC programs. More detailed studies about the four-parton Monte Carlo programs are presented in Chapter 7.

Detector Corrections

The theoretical prediction for the four-jet angular correlations, already corrected for hadronization effects, has to be corrected further to include detector effects before being compared to ALEPH data. This is done by computing these observables from the MC before and after simulation, and the corrections are found in Fig. 6.10. In the case of $\cos\alpha_{34}$ the detector corrections calculated from the simulation with the PYTHIA four-parton option passed through the detector simulation is also shown. This, as explained in Section 5.3.2, is the one used for the systematic uncertainty estimation.

Total Corrections

Taking into account the hadronization and detector corrections as explained in the previous chapter, the total corrections for each four-jet observable can be constructed as

$$C^{\mathrm{tot}}(i_{bin}) = C^{\mathrm{bck+had}}(i_{bin}) \cdot C^{\mathrm{det}}(i_{bin}) \,. \tag{6.2}$$

Figure 6.11 shows the total bin-by-bin corrections for the angular correlations when using PYTHIA for the hadronization corrections. Typically such corrections are found within the 5-10% range. The corrections for the four-jet rate can be found in Fig. 6.3.

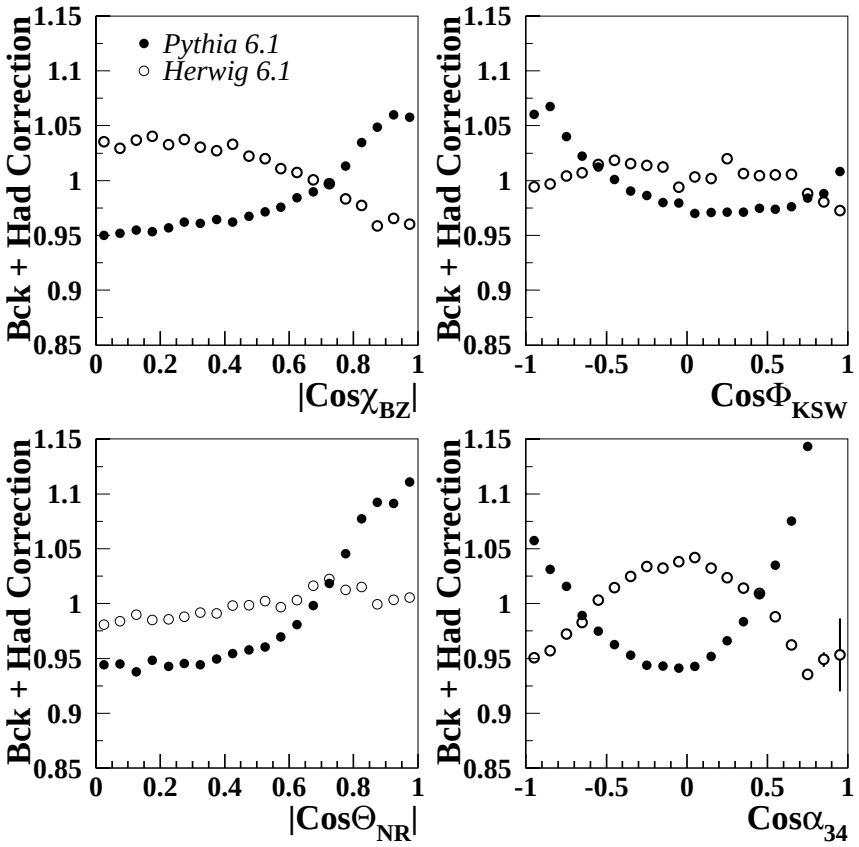

Figure 6.9: Background and hadronization corrections for the four-jet angular correlations.

6.2.2 Results

An experimental covariance matrix is calculated to take into account the statistical error of the data, the statistical errors of the detector and hadronization corrections, and the bin-by-bin statistical correlations among the different observables as well as the correlations between the bins of a single observable. Tables 6.13-6.16 show the data distributions for the four-jet angular correlations from ALEPH. Results for the four-jet rate can be found in Table 6.1. The correlations among the angular abservables are displayed in Fig. 6.12, where the correlations reach values higher than 50% for some bins.

Then a χ^2 minimization is performed with respect to η, x and y, using statistical errors only. The fit range is selected by requiring the total corrections for each observable

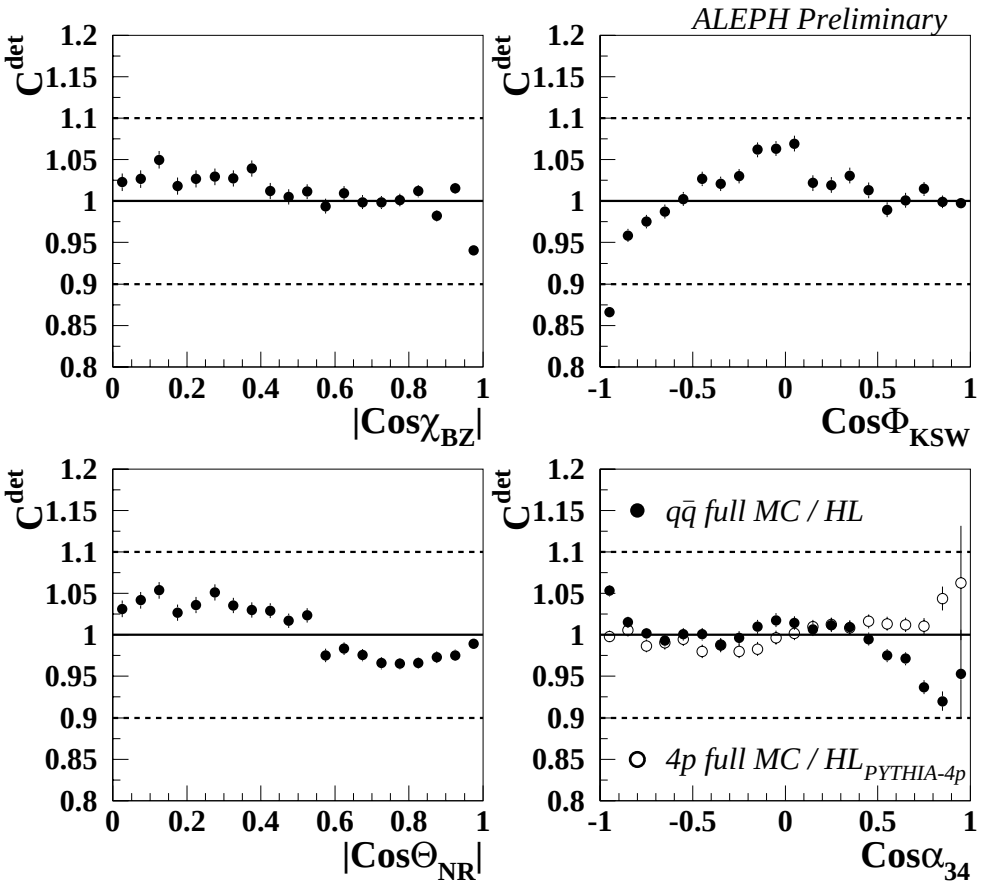

Figure 6.10: Detector corrections for the four-jet angular correlations.

to be smaller than 10%.

The results are seen in Table 6.17, and show good agreement with both QCD expectations and previous results [21] [55]. However, an important reduction of the statistical error is achieved. In the previous ALEPH analysis, the normalization of the four-jet angular correlations was also fitted, which prevented from achieving a better statistical precision. The fact that different observables were used should also be taken into account when comparing to the results in this thesis. The comparison with the OPAL results should be done after considering the smaller amount of MC used in that case for the hadronization and detector corrections, as well as the differences in the fit ranges for the angular correlations.

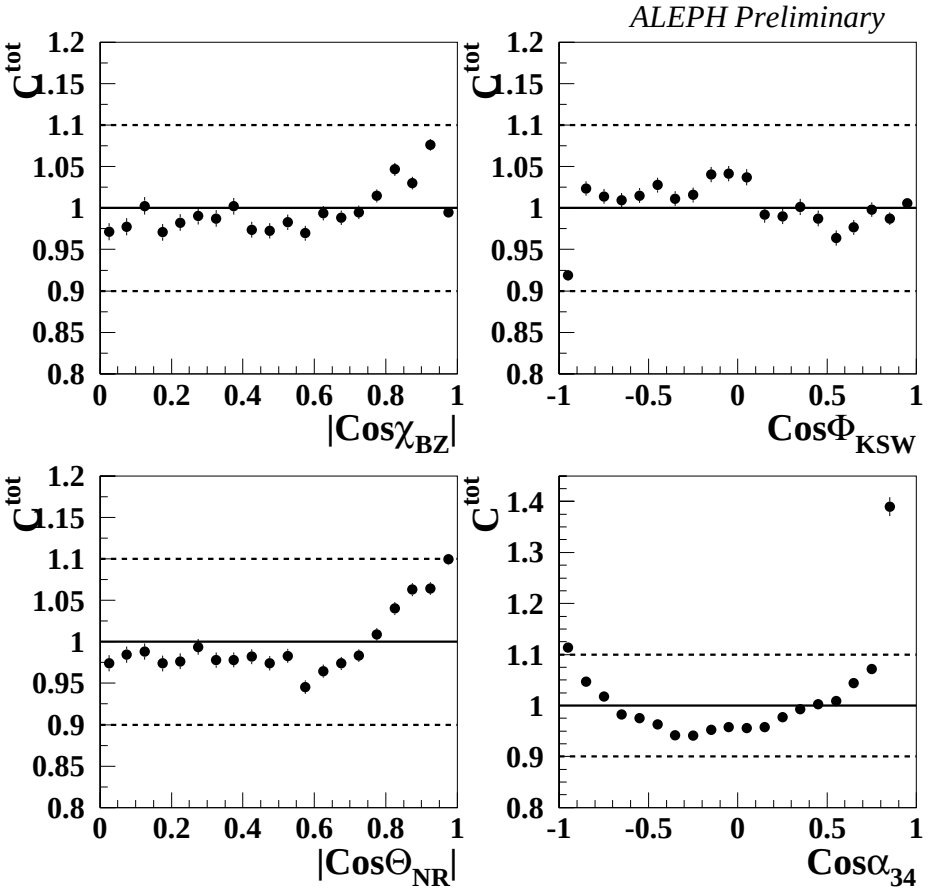

Figure 6.11: Total corrections for the four-jet angular correlations. The dashed lines show the maximum allowed corrections used for the fit.

The fitted distributions can be seen in Figs. 6.13 and 6.14. In the case of $\cos\alpha_{34}$ a significant discrepancy in the central region of the distributions is observed. This disagreement was already seen in [55]. Its origin is not understood. For the four-jet rate, the disagreement between the fitted predictions at small values of y_{cut} are again observed.

6.2.3 Systematic Studies

Tables 6.18-6.22 show the systematic uncertainties that have been studied. A brief description of each of them can be found in the following paragraphs.

Center of bin	N_{events} (ALEPH data)	N_{events} (full MC)	N_{events} (at HL)
0.025	5812 ± 74.86	10427 ± 100.45	79225 ± 277.04
0.075	5639 ± 73.78	10492 ± 100.77	79417 ± 277.37
0.125	5554 ± 73.24	10898 ± 102.64	80675 ± 279.48
0.175	5665 ± 73.95	10771 ± 102.06	82210 ± 282.04
0.225	5795 ± 74.76	11118 ± 103.63	84147 ± 285.23
0.275	5872 ± 75.24	11341 ± 104.63	85610 ± 287.61
0.325	5938 ± 75.64	11679 ± 106.12	88343 ± 292.01
0.375	5926 ± 75.57	12235 ± 108.52	91475 ± 296.95
0.425	6079 ± 76.50	12280 ± 108.71	94282 ± 301.30
0.475	6197 ± 77.21	12655 ± 110.29	97842 ± 306.71
0.525	6607 ± 79.62	13406 ± 113.38	103005 ± 314.36
0.575	6991 ± 81.80	13846 ± 115.15	108251 ± 321.92
0.625	7297 ± 83.49	14715 ± 118.54	113282 ± 328.98
0.675	7742 ± 85.87	15617 ± 121.94	121505 ± 340.13
0.725	8122 ± 87.85	16768 ± 126.12	130519 ± 351.86
0.775	8929 ± 91.87	18295 ± 131.41	141982 ± 366.11
0.825	9862 ± 96.26	20311 ± 138.01	155978 ± 382.61
0.875	10967 ± 101.14	22195 ± 143.83	175600 ± 404.29
0.925	12831 ± 108.72	26429 ± 155.85	202268 ± 431.45
0.975	25138 ± 145.81	51023 ± 207.48	421553 ± 592.89

Table 6.13: Number of events per bin for the $|\cos\chi_{\text{BZ}}|$ distribution from the ALEPH data. The events at detector level (DL) from the full MC simulation and at hadron level (HL) are also given since these are the distributions used to calculate the detector corrections.

Fit Range

The sensitivity of the measurement to the fit range is checked by repeating the analysis with the requirement of a total correction per bin smaller than 20% (it was 10% in the standard analysis). The systematic variation due to this new fit range, see Table 6.18, is smaller than the statistical errors of the measurement showing that the range chosen for the nominal fit does not introduce any important bias in the measurement.

Selection Criteria

All cuts imposed in the selection of hadronic events have been moved in order to evaluate the effect on the measurement. The new values for the selection cuts on track parameters

Center of bin	N_{events} (ALEPH data)	N_{events} (full MC)	N_{events} (at HL)
-0.95	11846 ± 104.81	23557 ± 147.84	211284 ± 440.10
-0.85	7938 ± 86.90	15814 ± 122.67	128190 ± 348.88
-0.75	7527 ± 84.73	15303 ± 120.77	121960 ± 340.73
-0.65	7539 ± 84.80	15135 ± 120.14	119118 ± 336.94
-0.55	7540 ± 84.80	15190 ± 120.35	117738 ± 335.07
-0.45	7491 ± 84.54	15342 ± 120.92	116120 ± 332.88
-0.35	7768 ± 86.01	14966 ± 119.50	113898 ± 329.83
-0.25	7698 ± 85.64	14780 ± 118.79	111499 ± 326.50
-0.15	7868 ± 86.53	15049 ± 119.81	110124 ± 324.57
-0.05	8050 ± 87.48	15335 ± 120.89	112062 ± 327.28
0.05	7220 ± 83.07	13799 ± 114.96	100295 ± 310.37
0.15	6775 ± 80.58	12680 ± 110.40	96427 ± 304.57
0.25	6537 ± 79.21	12507 ± 109.67	95340 ± 302.92
0.35	6112 ± 76.70	12638 ± 110.22	95270 ± 302.81
0.45	6325 ± 77.97	12646 ± 110.26	96998 ± 305.43
0.55	6286 ± 77.74	12832 ± 111.03	100762 ± 311.06
0.65	6721 ± 80.27	13662 ± 114.41	106079 ± 318.82
0.75	7341 ± 83.73	15448 ± 121.31	118312 ± 335.85
0.85	8942 ± 91.93	18621 ± 132.51	144837 ± 369.55
0.95	19439 ± 130.84	41197 ± 189.73	320871 ± 529.43

Table 6.14: Number of events per bin for the $\cos\Phi_{\text{KSW}}$ distribution from the ALEPH data. The events at detector level (DL) from the full MC simulation and at hadron level (HL) are also given since these are the distributions used to calculate the detector corrections.

are found by changing them until the number of selected events per unit luminosity is the same in data and MC [54]. The analysis has been repeated by introducing the following changes (only one at a time): at least six measured space coordinates from the TPC; a polar angle at the origin in the range $20^\circ < \theta < 160^\circ$ both for charged and neutral tracks; transverse momentum $p_t > 0.205$ GeV/c; $d_0 = 1.867$cm; $z_0 = 6.64$cm; at least 8 selected charged tracks; minimum charged energy 22 GeV; $|\cos\Theta_{\text{Sph}}| < 0.85$; and fraction of electromagnetic energy $< 20\%$.

The observed changes when modifying the selection cuts are in general small and in many cases even negligible. The largest are at the 1% level for x and 2% for y (always below 1% for η).

Center of bin	N_{events} (ALEPH data)	N_{events} (full MC)	N_{events} (at HL)
0.025	6200 ± 77.23	11843 ± 106.83	89238 ± 293.43
0.075	6190 ± 77.18	11936 ± 107.24	89041 ± 293.12
0.125	6130 ± 76.81	12182 ± 108.29	89840 ± 294.38
0.175	6238 ± 77.45	12067 ± 107.80	91318 ± 296.70
0.225	6420 ± 78.53	12412 ± 109.27	93122 ± 299.51
0.275	6419 ± 78.52	12944 ± 111.49	95685 ± 303.44
0.325	6609 ± 79.63	13228 ± 112.66	99272 ± 308.85
0.375	6742 ± 80.39	13615 ± 114.22	102727 ± 313.96
0.425	7026 ± 81.99	14187 ± 116.49	107132 ± 320.33
0.475	7409 ± 84.10	14740 ± 118.64	112619 ± 328.06
0.525	7622 ± 85.24	15627 ± 121.98	118650 ± 336.31
0.575	7929 ± 86.85	15862 ± 122.85	126402 ± 346.56
0.625	8407 ± 89.29	16927 ± 126.69	133769 ± 355.97
0.675	8815 ± 91.31	17958 ± 130.27	143053 ± 367.41
0.725	9349 ± 93.88	18976 ± 133.69	152675 ± 378.80
0.775	9930 ± 96.57	20014 ± 137.07	161141 ± 388.47
0.825	10258 ± 98.04	20967 ± 140.07	168721 ± 396.87
0.875	10760 ± 100.25	21398 ± 141.41	170895 ± 399.23
0.925	10991 ± 101.24	22219 ± 143.90	177028 ± 405.81
0.975	13519 ± 111.34	27399 ± 158.43	215177 ± 443.77

Table 6.15: Number of events per bin for the $|\cos\theta_{\text{NR}}|$ distribution from the ALEPH data. The events at detector level (DL) from the full MC simulation and at hadron level (HL) are also given since these are the distributions used to calculate the detector corrections.

The total experimental systematic uncertainty is the quadratic sum of all contributions in Table 6.19, where individual contributions are calculated in the Bayesian approach. It results in 0.0002 for η, as well as 0.02 and 0.01 for the color factor ratios, x and y.

Hadronization and Background Corrections

The hadronization uncertainty is taken as the change in the fitted parameters when the corrections are calculated with HERWIG. The values can be found in Table 6.20 and show large systematic variations, up to 8.5% for y. The strong increase in the χ^2 when using

Center of bin	N_{events} (ALEPH data)	N_{events} (full MC)	N_{events} (at HL)
-0.95	11901 ± 105.03	26388 ± 155.74	194722 ± 424.00
-0.85	10876 ± 100.75	23119 ± 146.57	176953 ± 405.73
-0.75	10118 ± 97.42	21405 ± 141.43	166084 ± 393.97
-0.65	9460 ± 94.40	19943 ± 136.84	156041 ± 382.68
-0.55	9069 ± 92.54	18834 ± 133.22	146238 ± 371.23
-0.45	8778 ± 91.13	17892 ± 130.04	138956 ± 362.42
-0.35	8663 ± 90.57	16831 ± 126.35	132395 ± 354.24
-0.25	8472 ± 89.62	16366 ± 124.68	127638 ± 348.16
-0.15	8536 ± 89.94	16045 ± 123.52	123478 ± 342.74
-0.05	8553 ± 90.02	16032 ± 123.47	122407 ± 341.32
0.05	8654 ± 90.52	15858 ± 122.83	121501 ± 340.12
0.15	8573 ± 90.12	15873 ± 122.89	122513 ± 341.46
0.25	8701 ± 90.75	16337 ± 124.58	125502 ± 345.39
0.35	8706 ± 90.78	16404 ± 124.82	126296 ± 346.42
0.45	8601 ± 90.26	16535 ± 125.29	129140 ± 350.10
0.55	8376 ± 89.14	16359 ± 124.66	130377 ± 351.68
0.65	7634 ± 85.30	15844 ± 122.78	126767 ± 347.04
0.75	6194 ± 77.19	13351 ± 113.16	110759 ± 325.46
0.85	2961 ± 53.92	6727 ± 81.17	56819 ± 235.68
0.95	137 ± 11.70	358 ± 18.91	2920 ± 54.01

Table 6.16: Number of events per bin for the $\cos\alpha_{34}$ distribution from the ALEPH data. The events at detector level (DL) from the full MC simulation and at hadron level (HL) are also given since these are the distributions used to calculate the detector corrections.

$\eta(\mathrm{M_Z})$	x	y	χ^2/N_{dof}
0.0255 ± 0.0003	2.17 ± 0.06	0.37 ± 0.02	76.8/80

$\rho_{\eta y}$	ρ_{xy}
-0.450	0.845

Table 6.17: Results for the combined fit using ALEPH data.

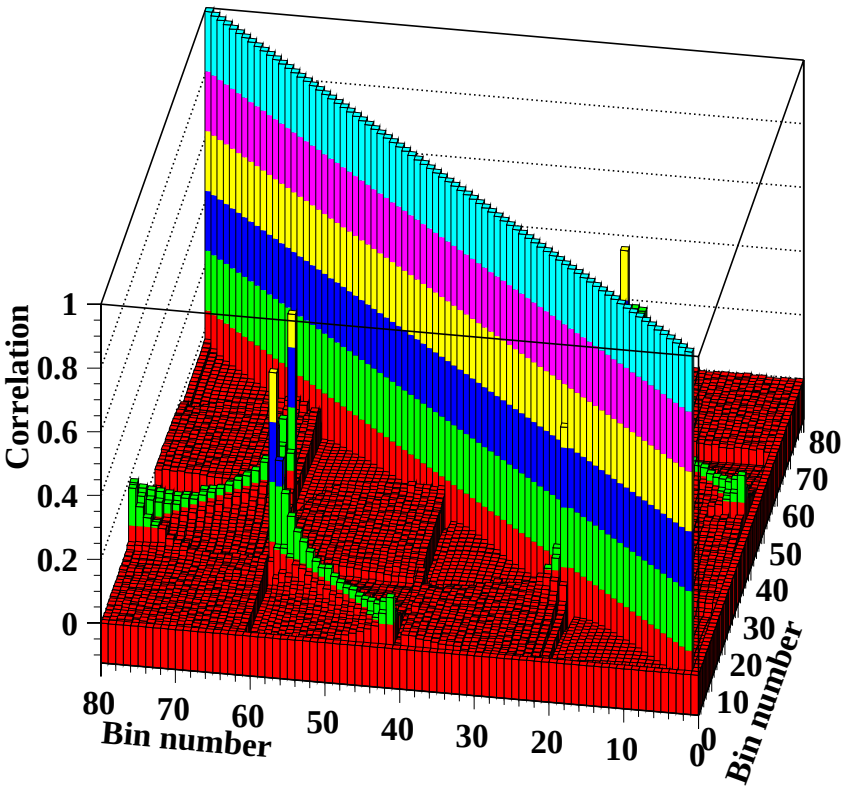

Figure 6.12: Bin-by-bin statistical correlations for the four-jet angular correlations. The numbers in the axis are the bin number: bins from 1 to 20 correspond to $|\cos\chi_{\mathrm{BZ}}|$, bins from 21 to 40 to $\cos\Phi_{\mathrm{KSW}}$, bins from 41 to 60 to $|\cos\theta_{\mathrm{NR}}|$ and bins from 61 to 80 to $\cos\alpha_{34}$.

	$\eta(\mathrm{M_Z})$	x	y	χ^2/N_{dof}
tot.corr. $< 20\%$	0.02565 ± 0.00021	2.191 ± 0.056	0.387 ± 0.019	89.0/88
Range sys.	$\Delta\eta = 0.0001$	$\Delta x = 0.02$	$\Delta y = 0.02$	

$\rho_{\eta y}$	ρ_{xy}
1.	1.

Table 6.18: Results when changing the fit range. The total corrections are chosen to be smaller than 20% instead of 10%.

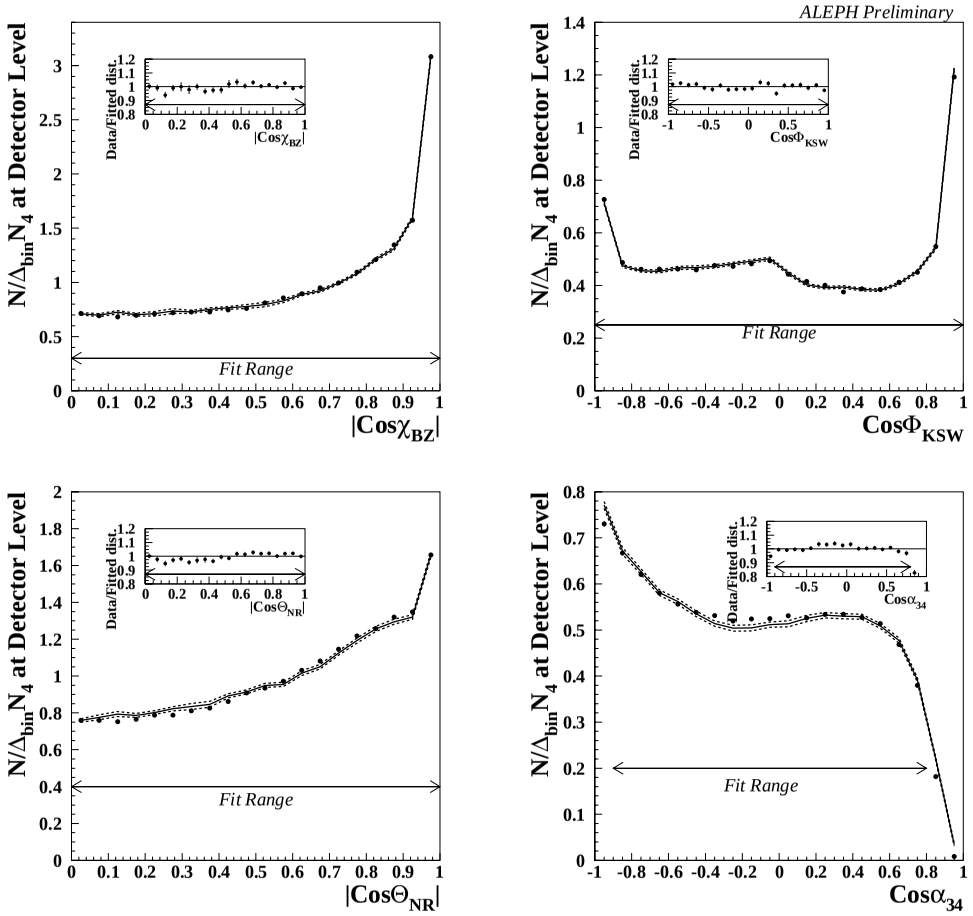

Figure 6.13: Comparison of ALEPH data and fit results for the angular correlations in four-jet events. The curves are obtained at detector level. Full dots correspond to ALEPH data. The solid lines show the fitted distributions while dashed lines correspond to their statistical uncertainty. The ratio of data with respect to fitted distributions is shown in the small inserts.

the corrections from HERWIG for the angular observables is an indication for unresolved issues in this new four-parton option.

Detector Corrections

An estimation of the systematic uncertainty due to the detector corrections has been obtained by repeating the analysis using charged tracks only. This change in the measurement procedure leads to systematic deviations on the parameters of about 1% for η and x, and about 3% for y.

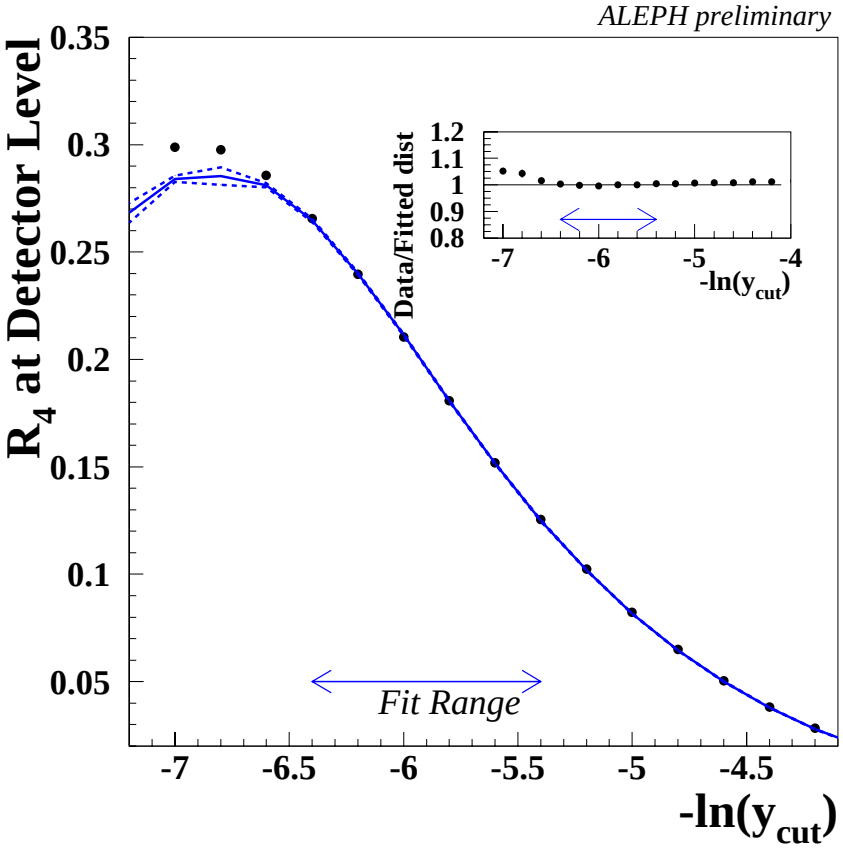

Figure 6.14: Comparison of ALEPH data and fit results for the four-jet rate. The curves are obtained at detector level. As in the previous figure, full dots correspond to ALEPH data and the solid line to the fitted distribution. The dashed lines are also plotted, however they are indistinguishable from the solid line for most of the y_{cut} range. Again, the ratio of data with respect to fitted distributions is shown in the small insert.

Another estimate is obtained by means of the four-parton full MC simulation described in Section 5.3.2. As explained, this new simulation is only used to correct $\cos\alpha_{34}$. It results in deviations similar to using charged tracks only.

The final uncertainty due to detector corrections, quoted in Table 6.21, is calculated by taking into account the two sources described above.

Theoretical Predictions

The lack of knowledge of higher order perturbative QCD is estimated by varying the renormalization scale in the theoretical predictions. The scale is varied from $x_\mu = 0.5$

	$\eta(M_Z)$	x	y	χ^2/N_{dof}
Sphericity cut	0.02559 ± 0.00031	2.172 ± 0.064	0.373 ± 0.020	71.9/80
TPC cut	0.02540 ± 0.00030	2.166 ± 0.062	0.362 ± 0.020	76.3/80
N_{ch} cut	0.02562 ± 0.00031	2.151 ± 0.062	0.363 ± 0.020	84.6/80
E_{ch} cut	0.02551 ± 0.00031	2.179 ± 0.063	0.373 ± 0.020	75.9/80
θ_{ch} cut	0.02568 ± 0.00031	2.167 ± 0.062	0.376 ± 0.020	75.8/80
θ_{nt} cut	0.02556 ± 0.00031	2.155 ± 0.062	0.366 ± 0.020	81.1/80
Fraction of e.m. energy cut	0.02553 ± 0.00031	2.163 ± 0.062	0.366 ± 0.020	77.3/80
z_0 cut	0.02553 ± 0.00031	2.168 ± 0.062	0.369 ± 0.020	78.0/80
d_0 cut	0.02553 ± 0.00031	2.168 ± 0.062	0.369 ± 0.020	76.9/80
p_t cut	0.02549 ± 0.00031	2.169 ± 0.062	0.368 ± 0.020	79.1/80
Experimental sys.	$\Delta\eta = 0.0002$	$\Delta x = 0.02$	$\Delta y = 0.01$	

$\rho_{\eta y}$	ρ_{xy}
0.766	0.532

Table 6.19: Systematic uncertainties due to the selection cuts used in the analysis.

	$\eta(M_Z)$	x	y	χ^2/N_{dof}
HERWIG - all	0.02592 ± 0.00033	2.207 ± 0.072	0.428 ± 0.023	432./80
HERWIG - angles, PYTHIA - R_4	0.02508 ± 0.00032	2.225 ± 0.071	0.370 ± 0.023	412./80
PYTHIA - angles, HERWIG - R_4	0.02639 ± 0.00033	2.135 ± 0.064	0.417 ± 0.020	79.1/80
Background & Hadronization Sys.	$\Delta\eta = 0.0006$	$\Delta x = 0.02$	$\Delta y = 0.03$	

$\rho_{\eta y}$	ρ_{xy}
0.797	0.158

Table 6.20: Systematic uncertainties due to the background and hadronization corrections.

to x_μ=2, and the largest difference to the value found for x_μ=1 is taken as systematic uncertainty. As the theoretical predictions for R_4 and for the angular correlations are known at different accuracy, the scale uncertainty is estimated by varying x_μ separately for each of the two kind of observables. The resulting uncertainty is 4% for η, 2% for x and 13% for y. It is the dominant one for the first and third parameters.

	$\eta(\mathrm{M_Z})$	x	y	χ^2/N_{dof}
Charged Only	0.02577 ± 0.00031	2.143 ± 0.062	0.359 ± 0.020	82.5/80
4-partons Full MC	0.02583 ± 0.00031	2.089 ± 0.061	0.346 ± 0.020	101.1/80
Detector sys.	$\Delta\eta = 0.0001$	$\Delta x = 0.02$	$\Delta y = 0.01$	

$\rho_{\eta y}$	ρ_{xy}
-0.896	0.991

Table 6.21: Systematic uncertainties due to detector effects.

The experimentally optimized scale method, which was used for the measurement of the strong coupling from the four-jet rate, is not used for the combined measurement for several reasons. First, the normalized angular correlations have been used due to the lack of the resummation of large logarithms. The normalized observables are expected to have a small scale dependence, as this is cancelled out in the normalization by the NLO four-jet cross section. Then, at least two different scales should be fitted, one for the four-jet rate and another for the angular observables. Second, since the colour factors and x_μ are highly correlated, the addition of this new variable introduces instabilities in the fit. Finally, even if the predictions for all four-jet angular correlations are known at NLO, the optimized scale for each observable can take on different values.

An evaluation of mass effects, which are not included in the theoretical predictions, is attempted by using the FOURJPHACT MC program [58]. As the parameters for PYTHIA were optimized for massless partons, the hadronization and background corrections with massive partons for the angular observables are calculated as follows,

$$C^{\mathrm{bck+had}}(i_{bin}) = \frac{\cos X^{\mathrm{part-4j}}(i_{bin})}{\cos X^{\mathrm{part-py}}(i_{bin})} \frac{\cos X^{\mathrm{had-py}}(i_{bin})}{\cos X^{\mathrm{part-py}}(i_{bin})} \quad , \tag{6.3}$$

where the index part-4j indicates the parton level coming from FOURJPHACT, and part-py (had-py) the parton (hadron) level from PYTHIA. The first ratio corrects for mass effects in the LO prediction, and the second ratio assumes that the showering and hadronization corrections do not depend strongly on the quark masses. It is found that mass effects might be large, up to 0.07 for x.

The total theoretical uncertainty, see Table 6.22, is obtained adding quadratically the contribution of the two sources described above and results in the dominant systematic uncertainty for all parameters.

	$\eta(M_Z)$	x	y	χ^2/N_{dof}
x_μ=0.5 for the angles	0.02545 ± 0.00032	2.193 ± 0.067	0.377 ± 0.021	64.8/80
x_μ=2. for the angles	0.02558 ± 0.00030	2.148 ± 0.059	0.361 ± 0.019	87.9/80
x_μ=0.5 for R_4	0.02352 ± 0.00030	2.265 ± 0.062	0.266 ± 0.018	72.6/80
x_μ=2. for R_4	0.02712 ± 0.00031	2.096 ± 0.063	0.439 ± 0.021	86.8/80
scale sys.	$\Delta\eta = 0.0010$	$\Delta x = 0.051$	$\Delta y = 0.05$	
quark masses	0.02629 ± 0.00035	1.982 ± 0.062	0.317 ± 0.020	84.1/80
mass sys.	$\Delta\eta = 0.0003$	$\Delta x = 0.07$	$\Delta y = 0.02$	
Theoretical sys.	$\Delta\eta = 0.0010$	$\Delta x = 0.09$	$\Delta y = 0.05$	

$\rho_{\eta y}$	ρ_{xy}
0.792	-0.212

Table 6.22: Systematic uncertainties due to variations in the theoretical predictions.

6.2.4 Further Checks

Hadronization and Background Corrections

As a cross-check, the more extreme models presented in Sect. 5.3.1 were used to fit η and the color factor ratios. The systematic changes in the fitted parameters, see Table 6.23, would be of about 2-3%, which is covered by the total uncertainty. Finally, also the standard PYTHIA simulation, $q\bar{q}$ + PS + hadronization, has been used to correct the four-jet angular correlations (again Table 6.23). As expected, the χ^2 of the fit is much larger than the one of the standard fit showing that the PYTHIA simulation which uses four-parton matrix elements and a parton shower describes better the shape of the angular correlations.

Two- and Three-Parton Backgrounds for the Angular Correlations

The background and hadronization corrections used for the angular correlations are valid provided that the number of two- and three-parton events that are clustered into four jets after hadronization is negligible. This is verified by the following study.

Using the PYTHIA ME option as described in Section 5.3.1, 1 million events were generated. The hadronization parameters were the standard ones. The fraction of the

	$\eta(M_Z)$	x	y	χ^2/N_{dof}
ME - all	0.02787 ± 0.00036	1.967 ± 0.066	0.343 ± 0.020	96.1/80
ME - angles, PYTHIA - R_4	0.02632 ± 0.00034	1.979 ± 0.065	0.317 ± 0.020	98.3/80
PYTHIA - angles, ME - R_4	0.02702 ± 0.00032	2.154 ± 0.063	0.394 ± 0.020	76.9/80
PYTHIA,Q_0 - R_4	0.02749 ± 0.00034	2.111 ± 0.063	0.423 ± 0.020	90.0/80
PYTHIA $q\bar{q}$ - all	0.02639 ± 0.00033	1.92 ± 0.064	0.293 ± 0.020	162.1/80

Table 6.23: Check for the Hadronization and Background corrections. Deviations from the standard analysis are covered by the systematic uncertainties already described.

number of four-jet events at HL which came from two- and three-parton events with respect to the total number of four-jet events was found to be much smaller than 1%, and only slightly affecting the shape of the angular correlations as observed in Fig. 6.15.

In order to quantify how the two- and three-parton backgrounds could bias our measurement the four-jet angular correlations obtained at HL, from the PYTHIA ME simulation, were fitted. The hadronization corrections were calculated using the PYTHIA four-parton simulation. Then, from those distributions the background contributions were subtracted (dashed distributions in Fig. 6.15), and the resulting ones are fitted again. The difference between the fitted parameters can be taken as an estimate of the two- and three-parton background uncertainty. As seen in the Table 6.24, the systematic uncertainties for the different parameters are much smaller than the ones considered in the previous section. Therefore, no further two- and three-parton background treatment was implemented in the analysis.

	$\eta(M_Z)$	x	y	χ^2/N_{dof}
Full HL distrib.	0.02580 ± 0.00027	2.022 ± 0.048	0.308 ± 0.016	115.1/81
Without 2- & 3-parton bckg	0.02582 ± 0.00028	2.018 ± 0.048	0.308 ± 0.016	111.2/81

Table 6.24: Check for two- and three-parton background effects.

Sensitivity Checks

The sensitivity of the analysis to each of the observables is studied. The fit results when taking out one observable at a time can be seen in Table 6.25. As expected, η is mainly fixed by the R_4 distribution, and the color factor ratios by the angular correlations. The

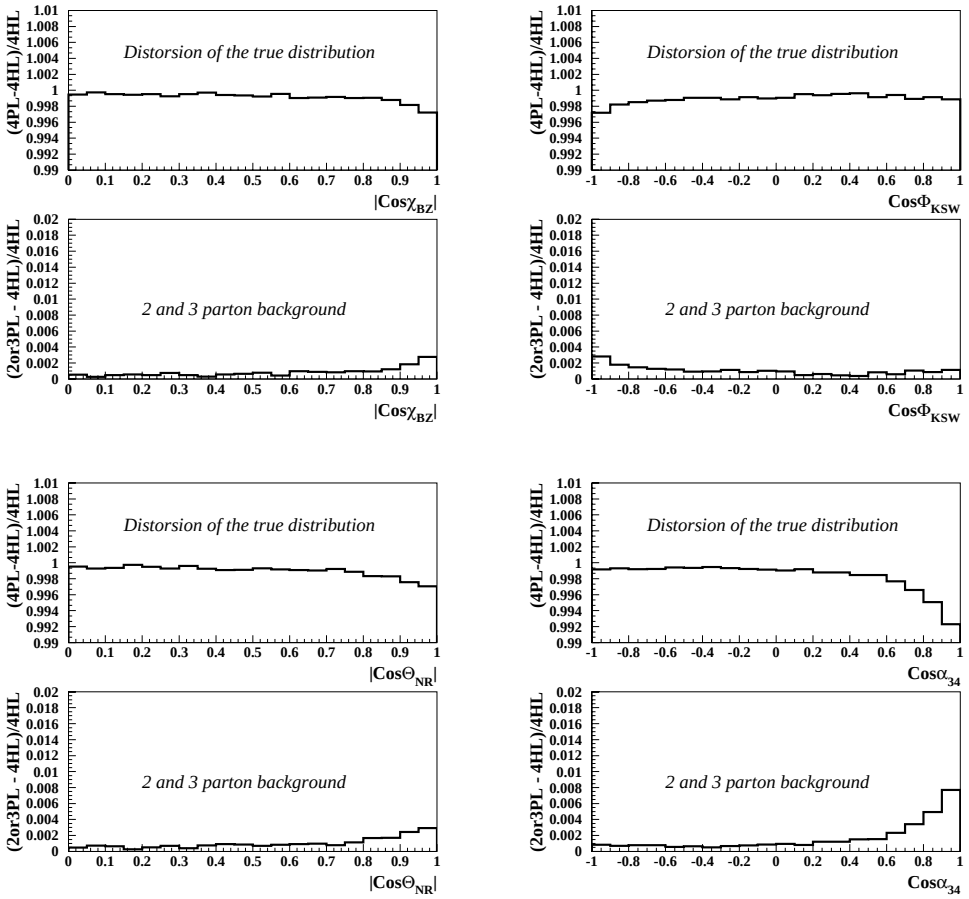

Figure 6.15: Distortion in the four-jet angular correlations due to two- and three-parton backgrounds.

sensitivity to the different angular correlations is quite similar. The fit with the angular correlations only resulted in a nonsense *eta*, for which the error could not be calculated.

	$\eta(\mathrm{M_Z})$	x	y	χ^2/N_{dof}
No $\cos\chi_{\mathrm{BZ}}$	0.0253 ± 0.0003	2.21 ± 0.08	0.38 ± 0.02	58.5/63
No $\cos\Phi_{\mathrm{KSW}}$	0.0256 ± 0.0003	2.12 ± 0.07	0.35 ± 0.02	52.6/60
No $\cos\Theta_{\mathrm{NR}}$	0.0255 ± 0.0003	2.19 ± 0.06	0.38 ± 0.02	59.1/60
No $\cos\alpha_{34}$	0.0255 ± 0.0003	2.16 ± 0.06	0.37 ± 0.02	66.1/60
No R_4	$0.0900 \pm - - -$	2.27 ± 0.09	0.37 ± 0.05	44.2/74

Table 6.25: Results from the sensitivity check. The analysis is repeated taking out one of the observables at a time.

Dependence on the y_{cut}

A check was performed in order to see if the present measurement depends on the chosen value of y_{cut}. The analysis is repeated with the four-jet events calculated for $y_{cut} = 0.01$, which represents a drop in the four-jet rate from 7.1% for the standard 0.008 y_{cut} value to 5.4%. The results are given in Table 6.26 and are in good agreement with the standard analysis.

	$\eta(M_Z)$	x	y	χ^2/N_{dof}
y_{cut}=0.01	0.0259 ± 0.0004	2.15 ± 0.08	0.34 ± 0.02	99.5/81

Table 6.26: Results for the fit when y_{cut} is fixed to 0.01 instead of 0.008 as used for the standard analysis.

6.2.5 Final Results

Putting together all systematic uncertainties considered above, the final result of the combined measurement of η and the colour factors ratios is:

$$\begin{aligned} \eta(M_Z) &= 0.0255 \pm 0.0003(stat) \pm 0.0012(sys) \\ x &= 2.17 \pm 0.06(stat) \pm 0.10(sys) \\ y &= 0.37 \pm 0.02(stat) \pm 0.06(sys) \end{aligned}$$

$$\begin{aligned} (\rho_{\eta y})_{stat} &= -0.450 \qquad (\rho_{\eta y})_{sys} = 0.769 \\ (\rho_{xy})_{stat} &= 0.845 \qquad (\rho_{xy})_{sys} = -0.028 \end{aligned}$$

which can also be expressed in terms of the strong coupling constant and the colour factors,

$$\begin{aligned} \alpha_s(M_Z) &= 0.119 \pm 0.006(stat) \pm 0.022(sys) \\ C_A &= 2.93 \pm 0.14(stat) \pm 0.50(sys) \\ C_F &= 1.35 \pm 0.07(stat) \pm 0.22(sys) \end{aligned}$$

These results are in good agreement with previous measurements. The dominant source of systematic uncertainty is obtained from variations in the theoretical predictions, where both the scale and the quark mass effects result in large deviations from the standard measurement.

Figure 6.16 shows that the measurement of the colour factor ratios is in agreement with the expectations from QCD (x=2.25 and y=0.375). The agreement with previous measurements by ALEPH [21] and lately by OPAL [55] is also observed. The total systematic errors are similar to the ones of previous analyses, but the statistical uncertainty has been strongly reduced because of the specific method adopted here.

Finally, Fig. 6.17 shows the fitted colour factor ratios for the systematic uncertainties considered in the analysis as well as for most of the further checks listed in Section 6.2.4. The compatibility of all variations with the standard fit is observed.

6.3 Massless Gluino Hypothesis

A final study was carried out in order to test the hypothesis of the existence of a massless gluino. As in the measurement described above, DEBRECEN is used to obtain the NLO perturbative prediction. This MC program provides not only the B and C functions for pure QCD, but also for QCD+massless gluino. Only the four-jet angular correlations have been used, since there is no consistent prediction for R_4, for which gluino contributions are not available in the resummation terms.

The simultaneous measurement of the strong coupling constant and the colour factors has been repeated using as perturbative predictions for the four-jet angular correlations the ones outlined in Eq. 3.22. Two cases have been considered. First, the B and C functions were taking into account only pure QCD configurations. Then the gluino contributions were also included in these functions, and the QCD beta function coefficients in Eq. 2.14 where changed to [20],

$$\begin{aligned} \beta_0 &= \frac{11}{3}x - \frac{4}{3}\left(yN_f + x\frac{N_g}{2}\right), \\ \beta_1 &= \frac{17}{3}x^2 - 2\left(y\,N_f + x^2\frac{N_g}{2}\right) - \frac{10}{3}\left(x\,y\,N_f + x^2\frac{N_g}{2}\right). \end{aligned} \tag{6.4}$$

where N_g is the number of gluinos, set to 1 in this analysis.

Hadronization and detector corrections were taken from the standard analysis under the assumption that they are not strongly dependent on the gluino contribution. At the moment of writing this work, there is no MC program which models the gluino contributions to hadronization. All the studies of systematic uncertainties described in

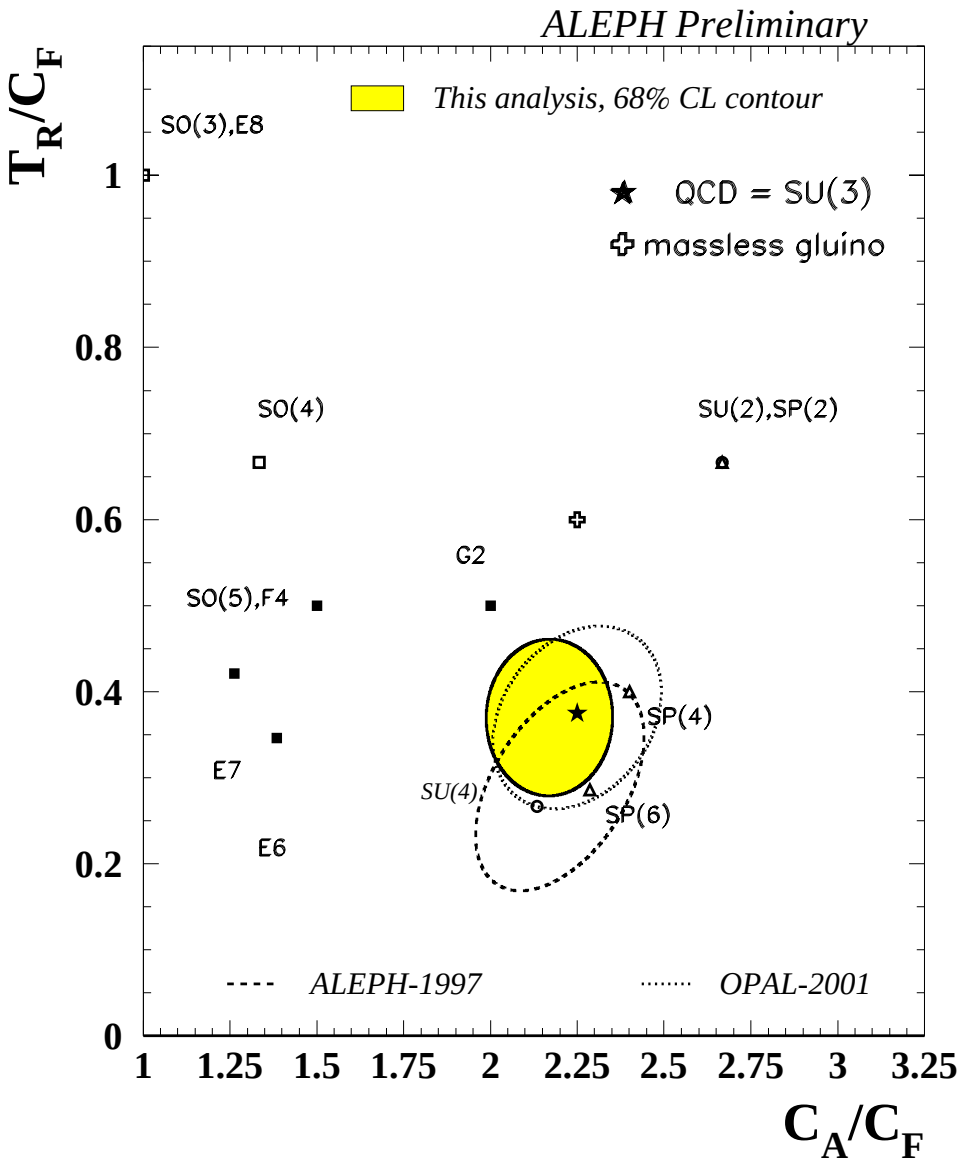

Figure 6.16: 68% confidence level contour in the (x,y) plane, calculated from statistical plus systematic errors (shaded region). For comparison also the results from previous measurements are given, as well as predictions for simple Lie groups.

Section 6.2.3 have been repeated.

The results of the fit together with an estimate of the systematic uncertainties are

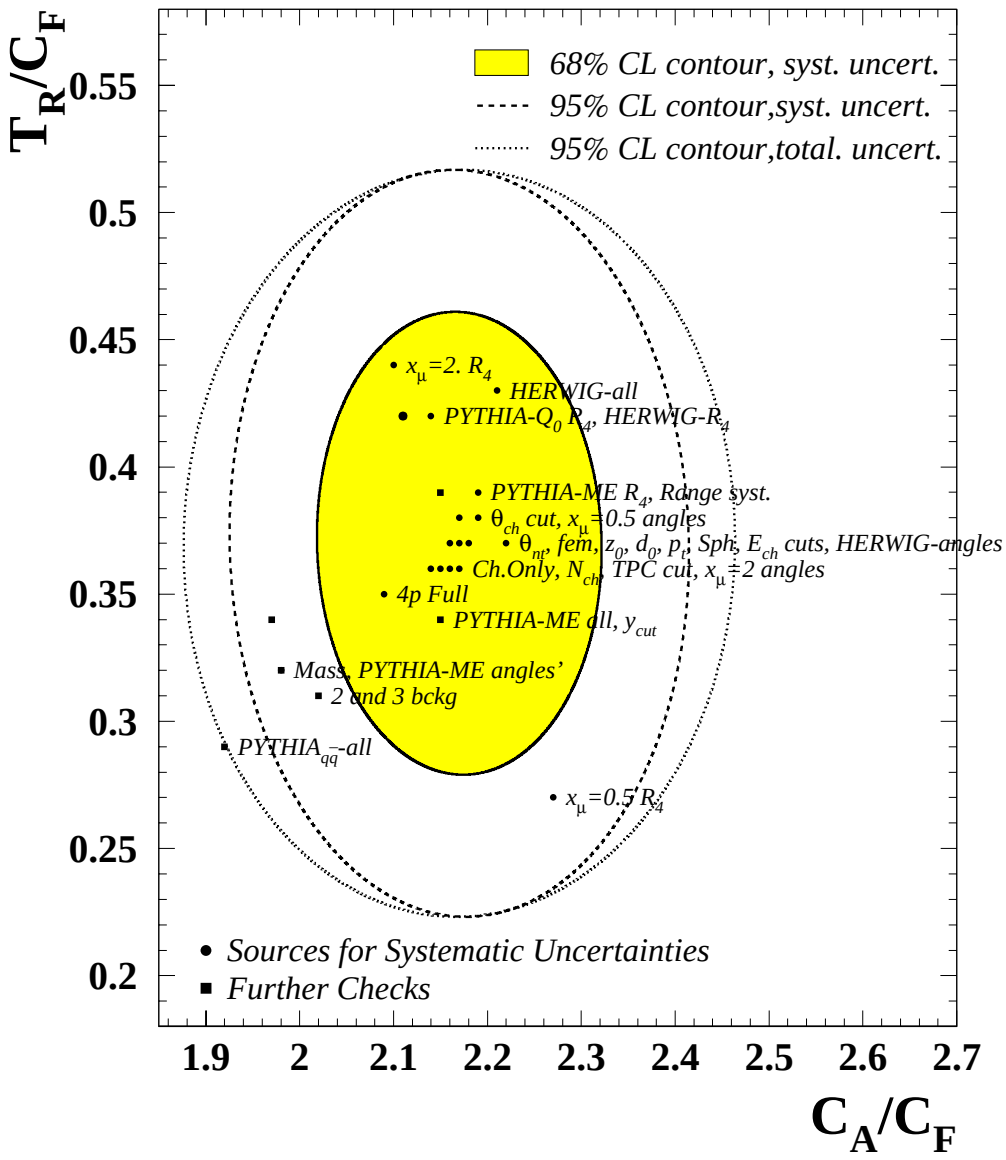

Figure 6.17: 68% and 95% confidence level contours in the (x,y) plane when taking into account systematic uncertainties only. The 95% confidence level contour with the total uncertainty is shown for comparison. Results for the sources of systematic uncertainty are also plotted.

$$x = 2.27 \pm 0.09(\text{stat}) \pm 0.08(\text{sys})$$
$$y = 0.38 \pm 0.05(\text{stat}) \pm 0.07(\text{sys})$$
$$(\rho_{xy})_{\text{total}} = -0.145$$

for the pure QCD case, and

$$x = 2.26 \pm 0.08(\text{stat}) \pm 0.07(\text{sys})$$
$$y = 0.15 \pm 0.06(\text{stat}) \pm 0.06(\text{sys})$$
$$(\rho_{xy})_{\text{total}} = -0.187$$

for the QCD+gluino hypothesis. The reduction of the total systematic uncertainty for x with respect to the standard fit comes from the lack of one of the contributions to the theoretical uncertainty estimate, namely the scale uncertainty for the four-jet rate.

Figure 6.18 shows that these results exclude the existence of a massless gluino at more than 95% confidence level, since the measured colour factor ratios do not agree with $SU(3)$ anymore. It is worth noting that effects of a massive gluino have not been studied in this thesis, since no NLO predictions including mass terms are available.

6.4 Conclusions

Results were presented for a measurement of the strong coupling constant from the four-jet rate as obtained by the Durham clustering algorithm (E-scheme). The result for $\alpha_{\text{s}}(\text{M}_{\text{Z}})$ using 1994-95 ALEPH data is:

$$\alpha_{\text{s}}(\text{M}_{\text{Z}}) = 0.1170 \pm 0.0001(stat) \pm 0.0014(sys) \quad ,$$

with the renormalization scale $x_\mu = 1$.

However, data shows a preference for x_μ values smaller than 1, as can be seen when α_{s} and x_μ are fitted simultaneously. In this case the results are

$$\alpha_{\text{s}}(\text{M}_{\text{Z}}) = 0.1175 \pm 0.0002(stat) \pm 0.0006(sys)$$
$$x_\mu = 0.73 \pm 0.05,$$

where the error on x_μ is statistical only. The preferred small x_μ indicates that missing higher order corrections are still important.

These results are in perfect agreement with previous measurements based on three-jet quantities [9][54].

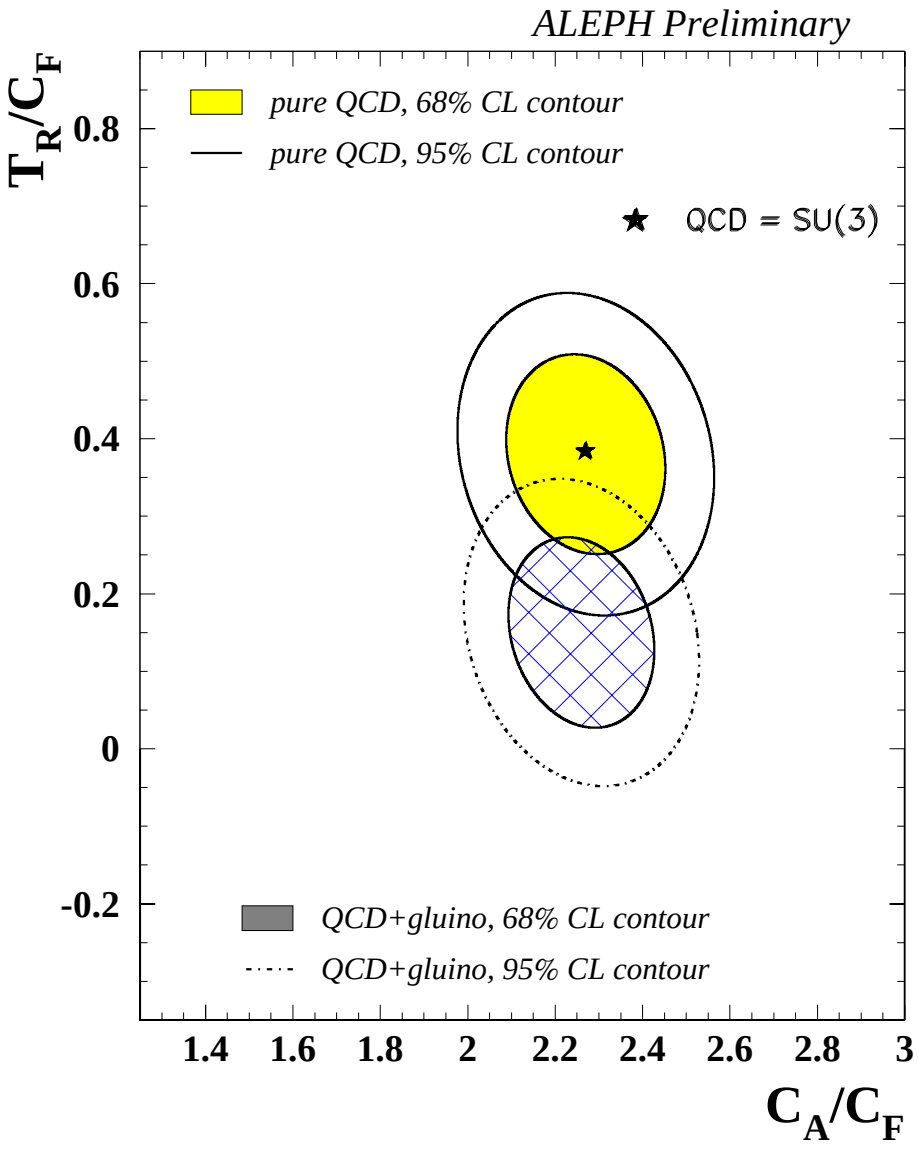

Figure 6.18: 68% and 95% confidence level contours in the (x,y) plane for the QCD and QCD+gluino hypotheses, based on four-jet angular correlations. The uncertainties include statistical as well as systematic errors.

A combined measurement of the strong coupling constant and the colour factors from angular correlations in four-jet events and the four-jet rate has been presented. For the jet finding the Durham clustering algorithm (E-scheme) was used, with y_{cut}=0.008 for the four-jet events used to compute the angular correlations. The results are

$$\alpha_s(M_Z) = 0.119 \pm 0.006(stat) \pm 0.022(sys)$$
$$C_A = 2.93 \pm 0.14(stat) \pm 0.50(sys)$$

$$C_F = 1.35 \pm 0.07(stat) \pm 0.22(sys)$$

These results are in good agreement with previous measurements, with similar systematic uncertainties, but with an important reduction in the statistical error.

Large discrepancies have been found when using either PYTHIA or HERWIG predictions for the calculations of hadronization corrections to the angular correlations. This indicates some problem either in the tuning or in the showering and hadronization implementation in these MC programs. The problems in the description of the shape for $\cos\alpha_{34}$ are further hints together with the worsening of the shape of the $|\cos\Theta_{\mathrm{NR}}|$ shape when using a full simulation starting from four-parton massless MEs.

Chapter 7

Four-Parton Monte Carlo Studies

Con las flores de un campo encendido
Como un San Francisco entre jarales vivos
De lagartos, vivo.
De quimeras me alimento,
Con simplezas me contento.

7.1 Motivation of the studies

In the context of this thesis many studies on the new four-parton Monte Carlo programs have been performed. In Section 5.3.1 it was already stated that there is a disagreement in the four-jet angular correlations between standard MCs and ALEPH data. For this reason, the new MC programs which allow to start a shower from four-parton configurations have been investigated in order to look for the best corrections for the four-jet angular correlations. As will be shown in the following sections, many aspects of the behaviour of four-parton MCs have been understood, but some problems remain opened at the moment of writing this work.

7.2 Studies on the intrinsic resolution parameter

The resolution parameter y_{cut} for clustering to four-jet events was chosen to be 0.008 for the angular correlations, based on purity and efficiency criteria. In Section 5.3.1, it was seen that both PYTHIA and HERWIG four-parton options have a key parameter to avoid soft and collinear divergences. This is the intrinsic resolution parameter, y_{int}, which was selected to be 0.004 in the MC simulations used for the calculation of the background and

hadronization corrections.

The specifications of the MC programs are $y_{int} \ll y_{cut}$, but no best value for y_{int} is given. In order to check for the dependence of the corrections on the y_{int} value, the following check was performed. Two samples of 1 million events ("test samples") with different values for y_{int} were generated using PYTHIA, and the four-jet angular correlations where calculated at three levels: parton level before showering (PL), parton level after showering (PS) and hadron level (HL). The y_{int} values were 0.003 and 0.005, and the distributions where compared to the ones used for the corrections in Section 5.3.1, where the intrinsic y_{cut} was set at 0.004 ("standard sample").

The ratios of the distributions for y_{int}=0.003(5) and y_{int}=0.004 at parton level and at hadron level are shown in Fig. 7.1. The ratios were calculated for the normalized angular correlations. In the figure no significant discrepancies are observed between the shape of the angular correlations from the "test samples" with respect to the "standard sample" used for the simultaneous measurement of the strong coupling constant and the colour factors. The discrepancies are only visible at the high edge of the $\cos\alpha_{34}$ distribution, but those bins where not used in the fit.

From this test it can be concluded that the background and hadronizations corrections used for the four-jet angular correlations do not sharply depend on y_{int}, except for some region in $\cos\alpha_{34}$. We expect that if y_{int} is moved to more extreme values the distributions will be affected. If y_{int} is increased too much, the condition of $y_{cut} \gg y_{int}$ will not be fulfilled and the MC distributions are not reliable anymore. If y_{int} is too small, the efficiency of the MC generation worsens quickly, and in the limit of very small y_{int} the soft and collinear singularities will not be cut out efficiently.

7.3 Studies on the Shower Models

The studies on the shower models are performed by comparing the distributions after the shower process from PYTHIA and HERWIG. In both cases the intrinsic resolution parameter was set to 0.004 and the showering parameters were set at the same values as for the standard $q\bar{q}$+PS+hadronization simulation. As both simulations start from the same four-parton level configurations, we can directly compare the normalized distributions after PS.

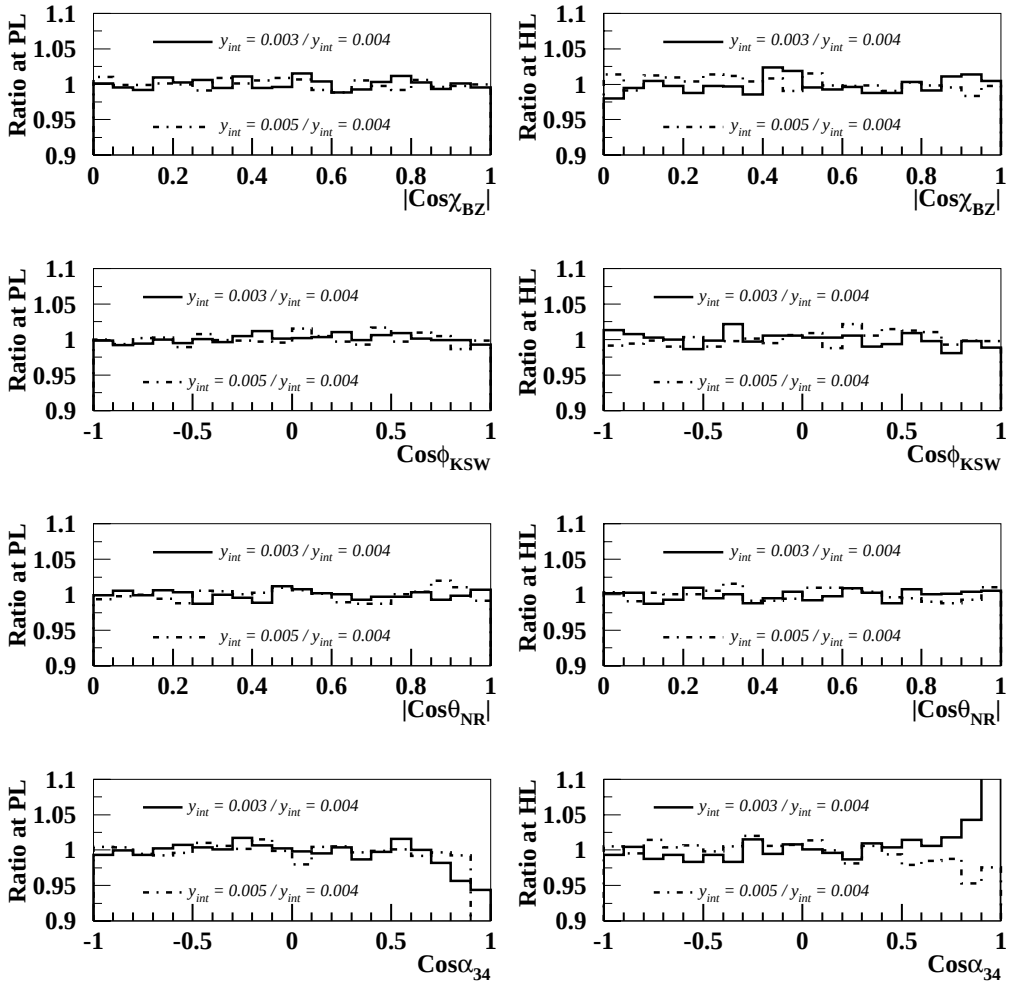

Figure 7.1: Ratios of the angular correlations for y_{int}=0.003 and 0.005 with respect to the standard value y_{int}=0.004 at parton and hadron level.

Figure 7.2 shows the comparison of the distributions coming from PYTHIA and HERWIG. The distributions show significant discrepancies, wich are more pronounced for $\cos\alpha_{34}$. This could be explained either by a better behaviour of one of the showering models, or by the need of retuning one (both) program(s). In principle, the tuned parameters should be "universal" for each Monte Carlo version. However, we have seen that the four-jet angular correlations are not well reproduced by the MC simulations starting from a $q\bar{q}$ pair, only. This might be an indication of a problem in the tuning of the MC programs, as usually the angular observables are not included in this process.

A last observation about the discrepancies observed is presented here. The four-jet angular correlations were thought to be sensitive to the intrinsic properties of the

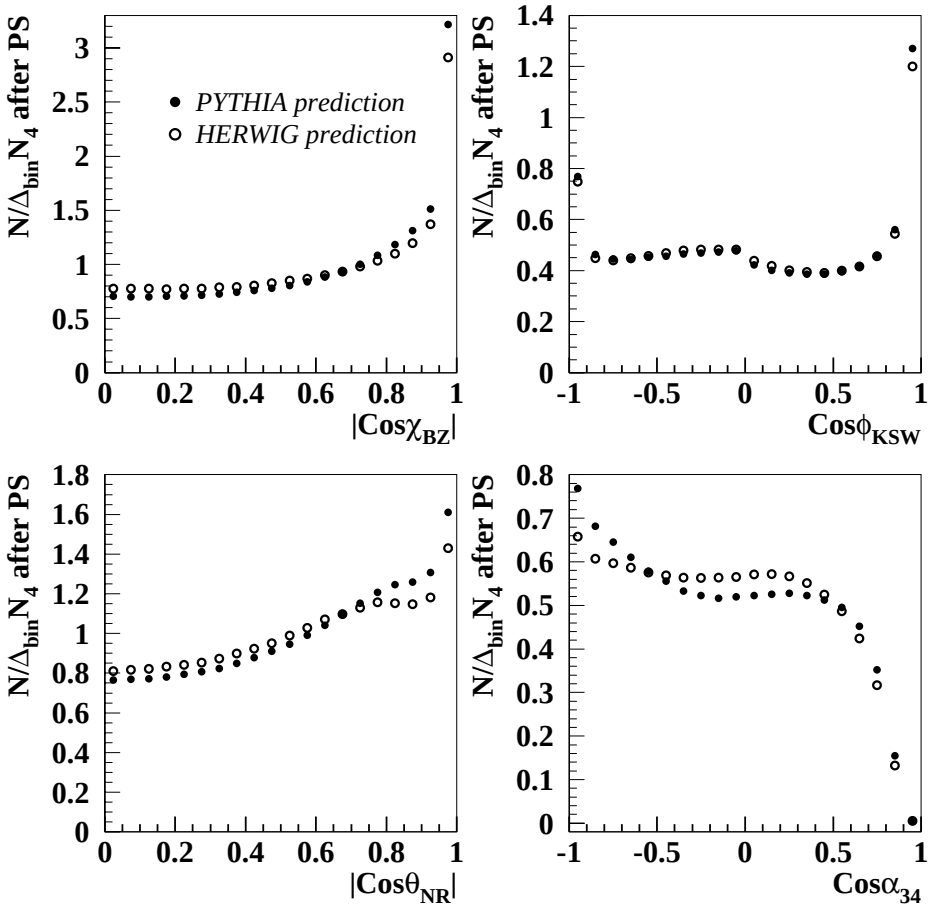

Figure 7.2: Comparison of the predictions after the parton shower from the four-parton option in PYTHIA and HERWIG.

structure of such events. It might be that the investigations so far have led to the point where the approximations and modelizations are not correct anymore (i.e. exact higher order calculations are required for an improvement of the predictions).

7.4 Studies on the Fragmentation Models

As already explained in Section 2.5, PYTHIA and HERWIG model in a different manner the fragmentation of the partons into hadrons at the end of the showering process. The first is based on a string fragmentation, and the second on a cluster fragmentation model. The comparison of the two fragmentation processes is done at hadron level after the shower level has been subtracted, since we are not interested (at this point) in the dif-

ferences at hadron level which are just a reflection of primary differences at parton level. So, the normalized hadron level distributions over the normalized parton shower distributions from PYTHIA and HERWIG, which are the so called hadronization corrections, are compared in Fig. 7.3. In this case, the discrepancies between both MC simulations are

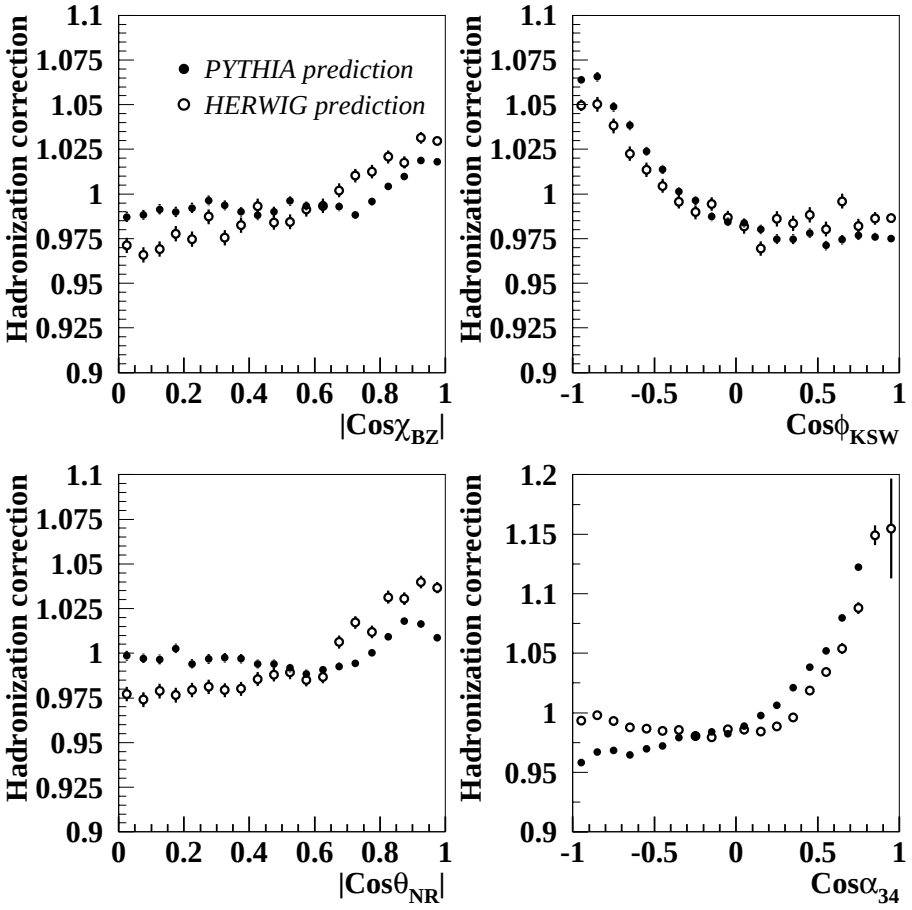

Figure 7.3: Comparison of the predictions for the hadronization corrections, i.e. hadron level over parton level distributions, from the four-parton option in PYTHIA and HERWIG.

smaller than for the comparison after the showering process. The differences are at the 2-4% level, only going to larger values at the high edge of the forth angular distribution, which is always the most sensitive to all effects encountered in the studies of this thesis. For the comparison after the showering process, the discrepancies where at the 10-20% level for wide range areas, and also going to larger values at the edges of some distributions. It is quite difficult to assess where the discrepancies at hadron level come from. At first approximation, the effects coming from the discrepancies due to the showering

process, already observed in the previous section, are taken out by the normalization. However, it could happen that the hadronization of the "non-common" configurations, i.e. the configurations present after the parton shower in PYTHIA but not in HERWIG (and vice-versa), is the source of the differences observed in Fig. 7.3.

However, the most obvious explanation would be to refer to the different models used in both Monte Carlo programs to simulate the hadronization. However, these fragmentation models have been shown to behave very similarly for the four-jet rate (see Fig. 6.1) and, once more, the parameters used are supposed to be universal. To exclude this second explanation the following test could be performed: take a set of events after the showering (either from PYTHIA or from HERWIG) and force them to hadronization first with PYTHIA and then with HERWIG. If a better agreement between the distributions at hadron level is obtained, then either the tuning or the remaining effects from the showering process should be further investigated in order to understand the disagreement. This possibility has not been studied here.

7.5 Studies on Quark Mass Effects

The only MC program with MEs including quark masses is FOURJPHACT, which showers and fragments through PYTHIA. The study described in this section arrived to the conclusion that small mass effects where expected for the observables used in the analyses. This explains why the PYTHIA simulation, without further corrections, was used to calculate the hadronization corrections.

In Section 5.3.1 the FOURJPHACT MC program was briefly described, and the possibility of simulating the different channels of a four-parton configuration was stated. This was exploited to investigate for mass effects in the four-jet angular correlations. Such distributions were calculated separately for the following channels: *(i)* $u\bar{u}u\bar{u}$, *(ii)* $u\bar{u}gg$, *(iii)* $b\bar{b}b\bar{b}$ and *(iv)* $b\bar{b}gg$. The resulting distributions were compared, $u\bar{u}u\bar{u}$ vs $b\bar{b}b\bar{b}$ and $u\bar{u}gg$ vs $b\bar{b}gg$, at parton level and at hadron level.

The comparison is done between channels *(i)* and *(iii)*, or *(ii)* and *(iv)* in order to make the mass effects visible. The other possible comparisons where already shown in Chapter 3 to stress the difference between "abelian" and "non-abelian" channels. Fig. 7.4 and 7.5 shows the comparison of the two four-quark channels for two of the angular correlations. If we first concentrate on the parton level distributions, the mass effects observed are small, but more important than the ones of the $q\bar{q}gg$ channels, for which

an example can be found in Fig. 7.6. This is an indication that the total mass effects, i.e. the effects when all channels are added with their corresponding weights, are much smaller than the ones observed when comparing the $u\bar{u}u\bar{u}$ and the $b\bar{b}b\bar{b}$ channels. First, because the production of $q\bar{q}gg$ dominates over the four-quark one. Second, because the channels containing a primary $b\bar{b}$ pair are only found in 20% of all hadronic events.

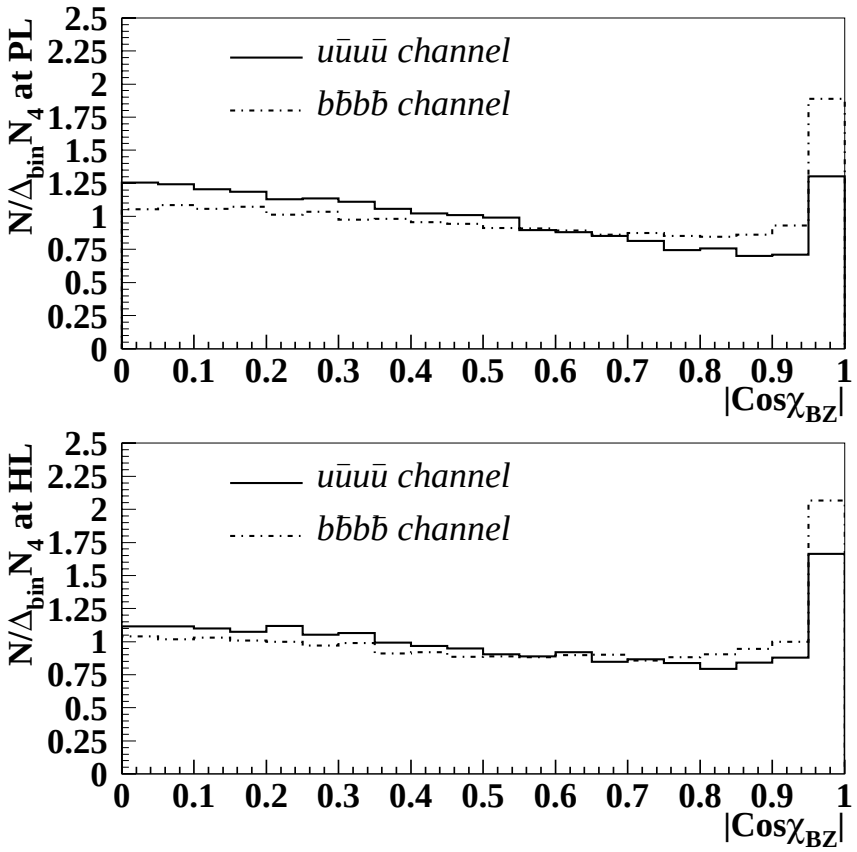

Figure 7.4: Comparison of the normalized distribution of $|\cos\chi_{BZ}|$ between a "massive" and a "massless" four-quark channel. The comparison is presented at parton level (upper plot) and at hadron level (lower plot).

When the comparison is done at hadron level (lower plots in the figures) we observe that the showering and hadronization processes reduce the discrepancies between partons of different mass, and so also between a massless and a massive simulation. Therefore, it is clear that a mass systematic uncertainty estimated at the parton level is a conservative estimate of the uncertainty at hadron level.

The discussion above indicates that the massive and massless distributions for the four-jet angular correlations do not present large discrepancies. However, it is difficult to

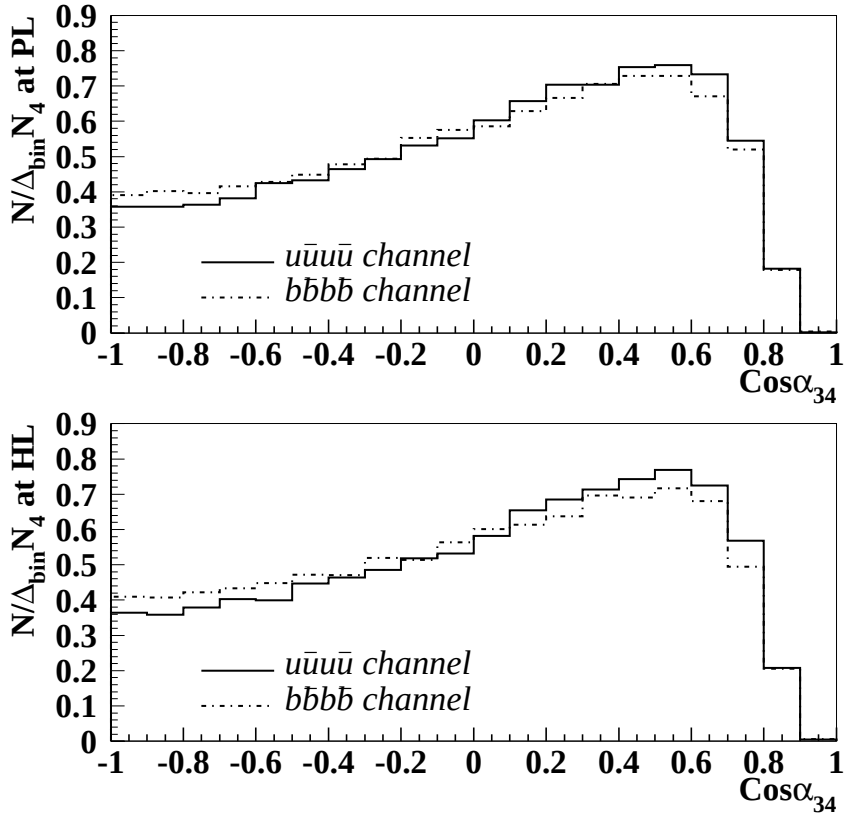

Figure 7.5: Comparison of the normalized distribution of $\cos\alpha_{34}$ between a "massive" and a "massless" four-quark channel. The comparison is presented at parton level (upper plot) and at hadron level (lower plot).

give an estimate of the mass effects in the measurement of the strong coupling constant and/or the colour factors. The effects on the strong coupling constant are expected to be very small because we are using normalized NLO angular correlations. However, the colour factors determine the shape of the distributions and they have been shown to be very sensitive to small variations in it. An estimation of such effects was presented in Section 6.2.3, but for a better estimation new MC programs with a precise treatment of masses in the whole chain of the event simulation are needed.

7.6 Other Studies to be performed

In the previous sections studies of the new Monte Carlo programs that allow to start a parton shower from four-parton matrix elements were shown. They are quite well understood, but more effort is needed in order to trust them at the same level than standard $q\bar{q}$ simulations. Detailed studies, that go beyond the purpose and time-scale of this thesis,

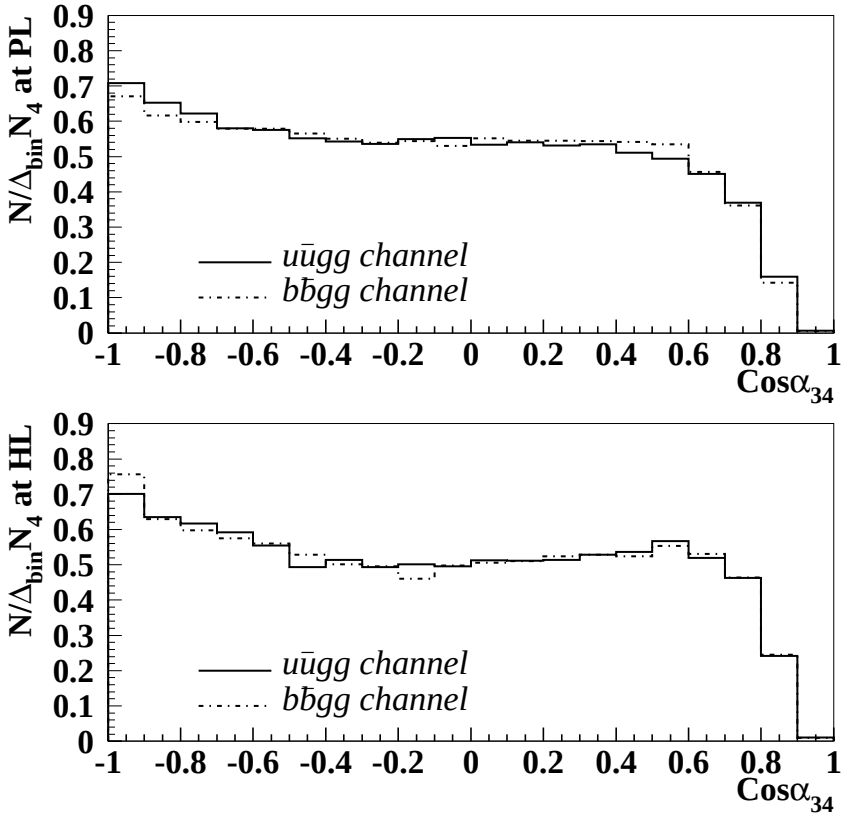

Figure 7.6: Comparison of the normalized distribution of $\cos\alpha_{34}$ between a "massive" and a "massless" two-quark two-gluon channel. The comparison is presented at parton level (upper plot) and at hadron level (lower plot).

should be performed, which will give a better comprehension of the properties of four-jet events.

More precisely, there is a new Monte Carlo program, APACIC, which is currently under development. Its basic ideas were already presented in Chapter 2, and preliminary tests showed a good performance of the new program [43]. Here no other studies will be shown as there is no tuning for the ALEPH detector, and for the time being there are different versions with their corresponding initial tunings that make any estimation of the performance of the APACIC program quite difficult and time consuming, for what concerns our analysis. As stated before, the colour factors are very sensitive to variations in the shape of the angular correlations. We would prefer to wait for a more definitive version of the APACIC program before testing its performance in the simultaneous measurement of the strong coupling constant and the colour factors.

Chapter 8

Summary and Outlook

Si lo que vas a decir
no es más bello que el silencio
no lo vayas a decir.

Two different kind of measurements have been presented in this thesis. First, three measurements of the strong coupling constant from the four-jet rate were described. Second, the simultaneous measurement of the strong coupling constant and the QCD colour factors was detailed. The analyses used ALEPH data from 1994 and 1995 and NLO predictions corrected to detector level.

The measurement of the strong coupling constant using NLO resummed predictions for the four-jet rate is the first measurement of α_s from a four-jet observable. The calculations that allow for a NLO prediction were finished some years ago. They allowed for a measurement of the strong coupling constant from new observables. In this thesis three different methods were tried. In the first case, taken as the nominal one, the result

$$\alpha_s(\mathrm{M_Z}) = 0.1170 \pm 0.0001(stat) \pm 0.0014(sys)$$

represents one of the most precise measurements on α_s at present. It is in perfect agreement with previous measurements by ALEPH and other collaborations which used two- and three-jet observables. Also, recent preliminary results by DELPHI using the four-jet rate are in excellent agreement with those presented here. The other two methods, based on the experimentally optimized scale method, lead to results compatible with the previous one.

Then, a stringent test of QCD was performed by measuring simultaneously the strong coupling constant and the colour factors. To do so, NLO predictions, corrected to detector level, for five four-jet observables are used: the four-jet rate and the four-jet angular correlations. A similar analysis had been performed in ALEPH before. The measurement presented in this thesis is the first combined measurement based on four-jet observables only. The new calculations and the new Monte Carlo programs available allow for a more precise measurement. The results,

$$\begin{aligned} \alpha_{\mathrm{s}}(\mathrm{M_Z}) &= 0.119 \pm 0.006(stat) \pm 0.022(sys) \\ C_A &= 2.93 \pm 0.14(stat) \pm 0.50(sys) \\ C_F &= 1.35 \pm 0.07(stat) \pm 0.22(sys) \end{aligned}$$

are in agreement with the expectation from QCD as well as with the previous results by ALEPH. A similar analysis, using the four-jet rate and the four-jet angular correlations, but also the differential two-jet rate, was performed by the OPAL Collaboration [55]. Our results show a good agreement with OPAL's results, however, a smaller statistical error is achieved here.

Finally, in the context of the simultaneous measurement of the strong coupling constant and the colour factors, the existence of a massless gluino has been excluded up to 95% CL. To do so, the simultaneous measurement was repeated taking into account the gluino contributions in the NLO predictions. For this test the assumption that hadronization corrections are quite independent of the existence of the light gluino is made. An improvement of this test will be possible as soon as full Monte Carlo simulations with the inclusion of the light gluino contributions become available.

At the end of this work we have presented studies performed with the new Monte Carlo programs that allow to start a parton shower from four-parton leading order matrix elements. Such programs are more suitable for our analysis as they are expected to better describe the shape of the four-jet angular correlations, shown to be badly described by the standard Monte Carlo simulations. The new four-parton Monte Carlo programs have been used in the present thesis, but some problems have appeared, such as the discrepancies between the corrections obtained from PYTHIA and HERWIG.

Detesto el tiempo, la ansiedad lamento.
Descansar sólo quiero, junto al calor del fuego.

Appendix A

The Experimentally Optimized Scale Method

The understanding of the role played by the renormalization scale parameter μ in the α_s measurements is the main goal of the coming sections. Such a parameter appears in the perturbative series of the QCD predictions, which for any observable is independent of this unphysical parameter if all the orders are known. However, usually only the first two terms are known, and for some observables also the resummation of large logarithms exists. The truncated perturbative prediction is then a function of the renormalization scale.

In many experiments, as well as in this thesis, the standard method for the measurement of the strong coupling constant is to perform the analysis with the scale μ fixed to some physical scale Q of the process, which for measurements at LEP1 is M_Z. Then, to test the dependence of the results on the renormalization scale, its value is varied from $Q/2$ to $2Q$. However, this is a somehow arbitrary estimation and some methods for a better estimation have been proposed.

The ratio of the NLO contribution with respect to the LO one can be used to estimate the importance of the unknown higher order terms. In many cases it is found to be close to unity, see Figs. A.1 and A.2, which is a clear indication of the poor convergence of the perturbative series. One can think of a value of the renormalization scale chosen in order to match the theoretical predictions to data. Such an optimal scale is found, without any theoretical assumption, by a combined fit of α_s and the scale, parametrized through x_μ defined in Section 3.2. This is the so called Experimentally Optimized Scale method (EOS), which was used for the measurement of the strong coupling constant from the

four-jet rate in Chapter 6 (called Method III).

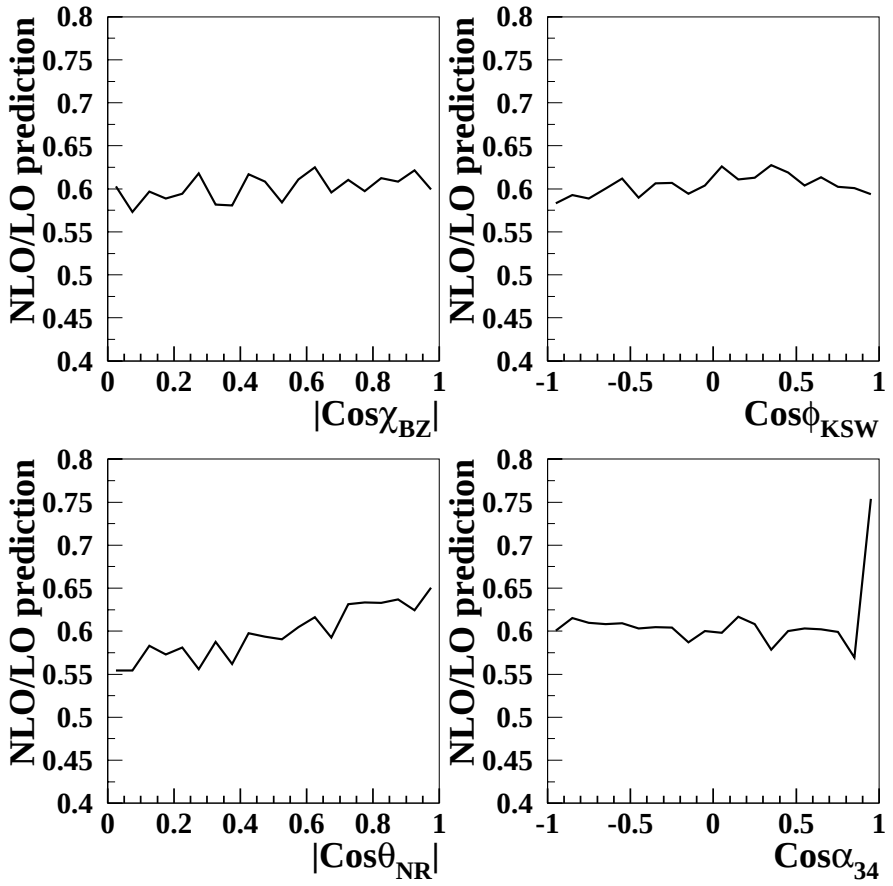

Figure A.1: K factor, NLO over LO prediction, for the four-jet angular correlations.

Other approaches, based on theoretical assumptions, have been proposed to find the best value for the renormalization scale so that fixed-order theoretical predictions better describe the data. More details can be found, for example, in Ref. [59]. Briefly, the methods try to find a general property for all observables which is an indication of a good convergence of the theoretical description. For example, in the FAC (fastest apparent convergence) method the scale is chosen to be the one that causes the NLO contributions to vanish. However, this has been proved not to work properly since the next-higher order terms are neither zero nor small for many observables.

Going back to the EOS method, it has been used for different measurements performed

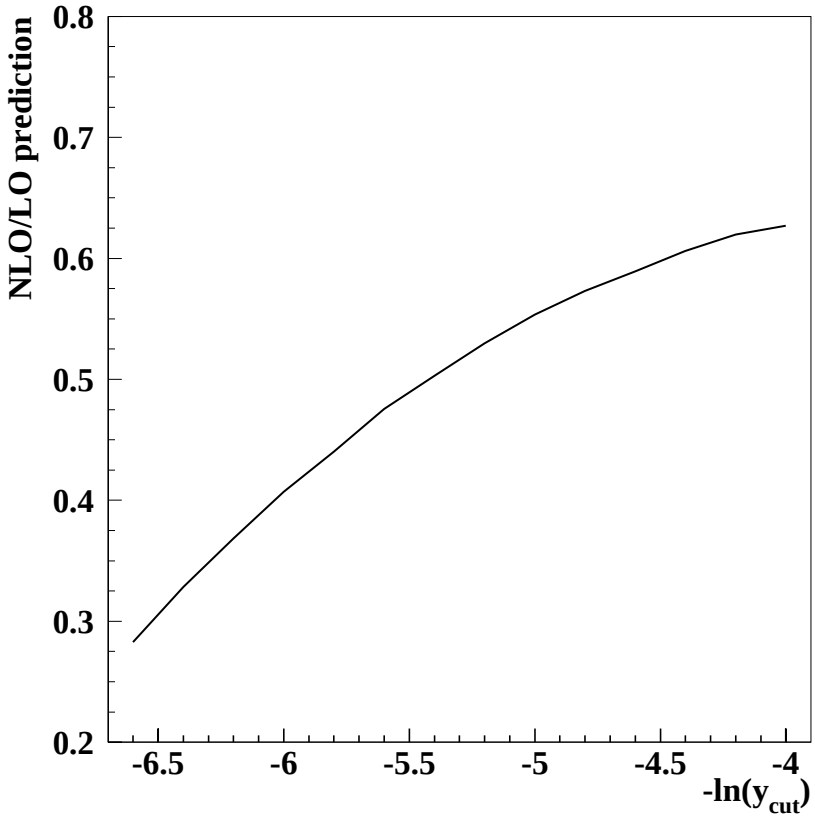

Figure A.2: K factor, NLO over LO prediction, for the four-jet rate.

by various experiments within and outside LEP. Some of these results are discussed in the following sections, as the validity of the method is still under investigation. As will be shown, different measurements have arrived to different conclusions.

In order to understand the discussions below two things have to be outlined. First, the experimentally optimized scale can differ for different observables, as the convergence of the truncated series does not have to be the same. Second, the scale is measured in a different way at different experiments. For example, we have been using the definition $x_\mu \equiv \frac{\mu}{M_Z}$, but in other collaborations the definition $x_\mu \equiv \left(\frac{\mu}{M_Z}\right)^2$ was chosen. The exact definiton of x_μ will be indicated when needed and has to be kept in mind when comparing results from different experiments.

A.1 Results with Optimized Scales from DELPHI

DELPHI has recently updated a LEP1 study on the EOS method using a set of 16 event-shape observables [60]. Results are compared from fits using $\mathcal{O}(\alpha_s^2)$ and $\mathcal{O}(\alpha_s^2)$+NLLA predictions. In Fig. A.3 the dispersion of the fitted α_s is shown to be much smaller for EOS at $\mathcal{O}(\alpha_s^2)$. Furthermore, in EOS the uncertainty due to hadronization corrections becomes the largest, since the scale uncertainty is heavily reduced. The scale uncertainty is measured in EOS as the largest deviation in α_s when x_μ is varied between 0.5 and 2 times the experimentally optimized value. EOS at $\mathcal{O}(\alpha_s^2)$, following the DELPHI conclusions, has then a small scale uncertainty with the total error heavily reduced. In Fig. A.4 the large dispersion of the experimentally optimized scales is shown, going from x_μ (here defined as $\frac{\mu^2}{M_Z{}^2}$) around 0.003 to 7.10, i.e. μ from 5 GeV to 240 GeV.

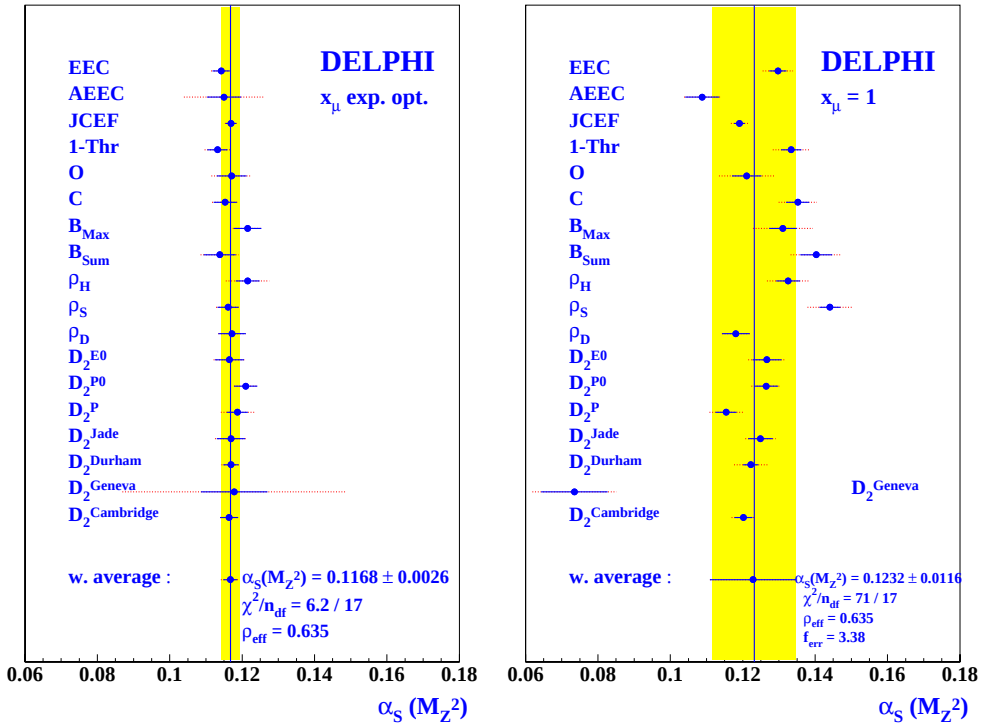

Figure A.3: DELPHI results using EOS.

Other conclusions drawn by DELPHI are that EOS at $\mathcal{O}(\alpha_s^2)$ describes the data over the whole fit range better than resummed predictions. Average results from the 16 observables show a good agreement between the EOS method and the fits to resummed predictions as seen in Table A.1.

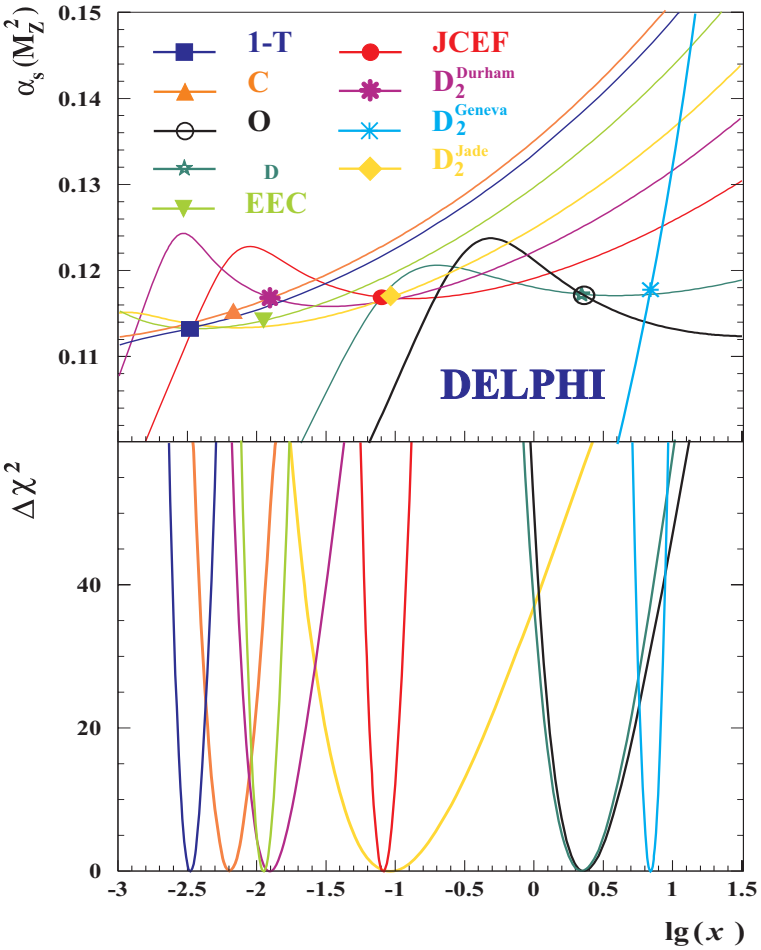

Figure A.4: Scale dependence for different observables in the EOS method.

	α_s	Total Error
EOS	0.117	0.003
$\mathcal{O}(\alpha_s^2)$ + NLLA	0.119	0.005

Table A.1: α_s results from DELPHI.

The study also includes results obtained when choosing the optimal scale according to some theoretical assumption (such as vanishing NLO terms). A larger dispersion in the fitted α_s is found, but the results are fully compatible with EOS. The study concludes that the best method for an α_s measurement from two- and three-jet observables is EOS

at $\mathcal{O}(\alpha_s^2)$.

A.2 Other Results with Optimized Scales: OPAL and SLD

A recent analysis by OPAL[61] has lead to different conclusions (and results from SLD[62] confirm such discrepancies). They show that $\mathcal{O}(\alpha_s^2)$ predictions describe better the data if the scale is also fitted. However, one can not arrive to a definitive conclusion concerning the comparison to resummed predictions, as the best prediction depends on the observable. Following this analysis resummed predictions have a smaller x_μ dependence, and therefore the smallest scale uncertainty. They show that the shape of both α_s and χ^2 depend strongly on the scale, but with a stable minimum. Following OPAL's studies the best method for an α_s measurement from two- and three-jet observables would be EOS at $\mathcal{O}(\alpha_s^2)$ +NLLA.

A.3 α_s from the 4-jet rate: ALEPH and DELPHI

In this section the results of the α_s measurements from the four-jet rate are summarised, see Section 6.1 and Ref. [56]. This observable has an attractive characteristic when compared to previously used three-jet observables. Since the LO term for four-jet observables is proportional to α_s^2, these observables have less sensitivity to possible large sources of systematics, as $\frac{\Delta\alpha_s}{\alpha_s} = \frac{1}{2}\frac{\Delta\sigma}{\sigma}$, where σ is the four-jet cross section and $\Delta\sigma$ its variation due to some systematic uncertainty source.

In the measurements performed by ALEPH a NLO+NLLA four-jet rate prediction, corrected to detector level, was fit to ALEPH data. The results when fitting only α_S (Method I) and when doing a combined fit of α_S and x_μ (i.e. EOS at NLO+NLLA) can be seen in Tables 6.2 and 6.3. The χ^2 of the two fits show an agreement with the conclusions from the OPAL collaboration, i.e. NLO predictions describe the data better if the scale is also fitted. Figure. 6.7 shows a strong dependence of the χ^2 with the renormalization scale, but with a clear minimum around 0.7. The scale dependence of α_s is small when compared to previous results using two- and three-jet observables. The smaller dependence is found with the EOS method.

The DELPHI Collaboration has performed a similar measurement, but fitting only NLO predictions to LEP1 DELPHI data [56]. Their results can be found in Table A.2 and show a good agreement with those presented in this thesis.

Observable	α_s	$\pm$	exp.	$\pm$	hadr.	$\pm$	scale
R_4	0.1178	$\pm$	0.0012	$\pm$	0.0023	$\pm$	0.0014

Table A.2: α_s results from the four-jet rate by DELPHI.

A.4 Conclusions

Two analyses by DELPHI and OPAL on Experimentally Optimized Scales have been discussed, showing some discrepancies in the final conclusions. However, they both agree on the reduction of the renormalization scale uncertainty when a combined fit of both α_s and μ is done. Finally, the α_s measurement by DELPHI from the four-jet rate has been presented briefly and compared to the one by ALEPH, already described in Chapter 6. The results from both experiments are in agreement with previous two- and three-jet measurements, and show an important reduction in the scale uncertainty. Such a reduction of the scale uncertainty is more important if the EOS method is used, but it is significant with the standard method (i.e. with x_μ fixed to 1), indicating that four-jet observables may have a smaller scale dependence than two- and three-jet variables.

Bibliography

[1] S.L. Glashow, Nucl. Phys. **B22** (1961) 579;
S. Weinberg, Phys. Rev. Lett. **19** (1967) 1264;
A. Salam, *Elementary Particle Theory*, ed. N. Svartholm, Almqvist and Wiksell, Stockholm (1968) 367;
S.L. Glashow, J. Iliopoulos and L. Maiani, Phys. Rev. **D2** (1970) 1285.

[2] H. Fritzsch and M. Gell-Mann, Proc. XVI Int. Conf. on High Energy Physics, eds. J.D. Jackson and A. Roberts (Fermilab 1972).

[3] G. 't Hooft, Nucl. Phys. **B33** (1971) 173.

[4] P.W. Higgs, Phys. Lett. **12** (1964) 132; Phys. Rev. Lett. **13** (1964) 508; Phys. Rev. **145** (1966) 1156.

[5] ALEPH Collaboration, Phys. Lett. **B495** (2000) 1;
DELPHI Collaboration, Phys. Lett. **B499** (2001) 23;
L3 Collaboration, Phys. Lett. **B508** (2001) 225;
OPAL Collaboration, Phys. Lett. **B499** (2001) 38.

[6] The LEP Collaborations, the LEP Electroweak Working Group and the SLD Heavy Flavour and Electroweak Groups, CERN-EP-2001-021, January 28, 2001.

[7] J.C. Collins and D.E. Soper, Ann. Rev. Nucl. Part. Sci. **37** (1987) 383.

[8] R.K. Ellis, W.J. Stirling and B.R. Webber, *QCD and Collider Physics*, Cambridge Monographs on Particle Physics, Nuclear Physics and Cosmology: 8 (1996), Cambridge University Press.

[9] S. Bethke, hep-ex/0004021 (2000).

[10] T. Sjöstrand, Comp. Phys. Comm. **82** (1994) 74;
T. Sjöstrand, P. Edén, C. Friberg, L. Lönnblad, G. Miu, S. Mrenna and E. Norrbin, Computer Phys. Commun. **135** (2001) 238.

[11] G. Marchesini, B.R. Webber, G. Abbiendi, I.G. Knowles, M.H. Seymour and L. Stanco, Comp. Phys. Comm. **67** (1992) 465.

[12] D. Amati, A. Bassetto, M. Ciafaloni, G. Marchesini and G. Veneziano, Nucl. Phys. **B173** (1980) 429.

[13] B. Andersson, G. Gustafson and B. Söderberg, Zeit. Phys. **C20** (1983) 317; Nucl.Phys. **B264** (1986) 29.

[14] D. Amati and G. Veneziano, Phys. Lett. **B83** (1979) 207;
A. Bassetto, M. Ciafaloni and G. Marchesini, Phys. Lett. **B83** (1985) 31;
G. Marchesini, L. Trentadue and G. Veneziano, Nucl. Phys. **B181** (1980) 335.

[15] R.K. Ellis, D.A. Ross and A.E. Terrano, Nucl. Phys. **B178** (1981) 421.

[16] S. Catani and M.H. Seymour, Nucl. Phys. **B485** (1997) 291.

[17] R. Kuhn, F. Krauss, B. Ivanyi and G. Soff, Comput. Phys. Commun. **134** (2001) 223.

[18] P.H. Nilles, Phys. Rev. **110** (1984) 1;
H. Haber and G. Kane, Phys. Rev. **115** (1985) 75.

[19] G. Farrar, Phys. Rev. **D51** (1995) 3904.

[20] L. Clavelli, P.W. Coulter and L.R. Surguladze, Phys. Lett. **D55** (1997) 4268.

[21] ALEPH Collaboration, Z. Phys. **C76** (1997) 1.

[22] F. Csikor and Z. Fodor, Phys. Rev. Lett. **78** (1997) 4335.

[23] S. Catani et al., Phys. Lett. **B269** (1991) 179.
N. Brown, J. Stirling, Z. Phys. **C53** (1992) 629.

[24] Z. Nagy, Z. Trócsányi, Phys. Rev. **D59** (1999) 14020;
Nucl. Phys. Proc. Suppl. **74** (1999) 44.

[25] J. Kodaira and L. Trentadue, Phys. Lett. **B112** (1982) 66;
C.T.H. Davies, W.J. Stirling and B.R. Webber, Nucl. Phys. **B256** (1985) 413;
S. Catani, E. d'Emilio and L. Trentadue, Phys. Lett. **B211** (1988) 335.

[26] G. Dissertori and M. Schmelling, Phys. Lett. **B361** (1995) 167.

[27] ALEPH Collaboration, Phys. Lett. **B257** (1991) 479; *ibid* **59** (1993) 21.

[28] S. Catani et al., Phys. Lett. **B269** (1991) 432.

[29] M. Bengtsson and P.M.Zerwas, Phys. Lett. **B208** (1988) 306;
M.Bengtsson, Z.Phys. **C42** (1989) 75.

[30] J.G. Körner, G. Schierholz and J. Willrodt, Nucl. Phys. **B185**, 365 (1981).

[31] O. Nachtmann and A. Reiter, Z. Phys. **C16** (1982) 45.

[32] S. Bethke, A. Richter and P.M. Zerwas, Z. Phys. **C49** (1991) 59.

[33] S. Myers and E. Picasso. *The design, construction and comissioning of the CERN Large Electron Positron collider*. Contemporary Physics **31** (1990) 387.

[34] Lep Design Report, vol. 1 CERN-LEP/83-29 (1983);
Lep Design Report, vol. 2 CERN-LEP/84-01 (1984).

[35] ALEPH Collaboration. Nucl. Inst. and Meth. **A294** (1990) 121.

[36] ALEPH Collaboration, Nucl. Instrum. Methods **A360** (1995) 481.

[37] ALEPH Collaboration, Phys. Rep. **294** (1998) 1.

[38] Y.L. Dokshitzer, Workshop on Jets at LEP and HERA, 1990.

[39] C. Peterson et al., Phys. Rev. **D27** (1983) 105.

[40] R. Brun et al., CERN DD/EE/84-1 (1987).

[41] Z. Trócsányi, private communication, 1999.

[42] ALEPH Collaboration, Z. Phys. **C73** (1997) 409.

[43] A. Ballestrero et al., hep-ph/0006259 (2000).

[44] G. Dissertori, ALEPH THESIS 97-009 (1997).

[45] S. Catani, L. Trentadue, G. Turnock, B.R. Webber, Phys. Lett. **B263** (1991) 461; Nucl. Phys. **B407** (1993) 3.
S. Catani and L. Trentadue, Phys. Lett. **B217** (1989) 539; Nucl. Phys. **B327** (1989) 323; Nucl. Phys. **B353** (1991) 183;
S. Catani, B.R. Webber and G. Marchesini, Nucl. Phys. **B349** (1991) 635;
S. Catani, G. Turnock and B.R. Webber, Phys. Lett. **B272** (1991) 368; Phys. Lett. **B295** (1992) 269..

[46] A. Signer, L. Dixon, Phys. Rev. Lett. **78** (1997) 811.

[47] L. Dixon, A. Signer, Phys. Rev. **D56** (1997) 4031.

[48] A. Signer, hep-ph/9705218 (1997).

[49] A. Signer, hep-ph/9706285 (1997).

[50] Z. Nagy, Z. Trócsányi, Phys. Rev. Lett. **79** (1997) 3604.

[51] E.W.N. Glover, hep-ph/9805481 (1998).

[52] Z. Nagy, Z. Trócsányi, Nucl. Phys. B (Proc. Suppl) **64** (1998) 63.

[53] Z. Nagy, Z. Trócsányi, Phys. Rev. **D57** (1998) 5793.

[54] ALEPH Collaboration, ALEPH 2000-044, CONF 2000-027.

[55] OPAL Collaboration, Eur. Phys. J. **C20** (2001) 601.

[56] U.Flagmeyer et al. DELPHI 2001-060. Contributed Paper for EPS HEP 2001 (Budapest) and LP01 (Rome)

[57] G. Dissertori, Nucl. Phys. B (Proc. Suppl) **65** (1998) 43.

[58] A. Ballestrero, private communication.

[59] J.Chýla and A. L. Kataev, hep-ex/9502383 (1995).

[60] DELPHI Collaboration. Eur. Phys. J. **C14** (2000) 557.

[61] The JADE and the OPAL Collaboration. Eur. Phys. J. **C17** (2000) 19.

[62] P.N. Burrows et al. Phys. Lett. **B382** (1996) 157.